NASA Contractor Report 3368

Surface Temperatures and Glassy State Investigations in Tribology - Part IV

Scott S. Bair and Ward O. Winer

NASA

NASA Contractor Report 3368

Surface Temperatures and Glassy State Investigations in Tribology - Part IV

Scott S. Bair and Ward O. Winer
Georgia Institute of Technology
Atlanta, Georgia

NASA

National Aeronautics
and Space Administration

**Scientific and Technical
Information Branch**

1980

TABLE OF CONTENTS

I. INTRODUCTION

In previous reports [1] it has been shown that at high pressure, typical lubricants undergo a viscoelastic transition from liquid to solidlike behavior. The transition pressure was determined for various temperatures and was shown to be a function of the characteristic rate of change of the environment. The constant rate transition was shown to occur at essentially constant viscosity by plotting isoviscous curves on a pressure-temperature transition diagram.

Investigations [2] of the ultimate shear strength of solidified lubricants and of the viscosity of the liquids at pressures just below their transition formed the basis of a rheological model employing three primary lubricant properties; low shear stress viscosity, limiting elastic shear modulus, and the limiting shear stress. The first of these properties is familiar and has been reported often in the literature. The limiting elastic shear modulus is less familiar but has been measured for many years by several techniques including ultrasonics. The limiting shear stress of liquid lubricants has been the subject of speculation for many years and indeed the nature of traction in EHD contacts has led several researchers to support that view for some time. Comparison of the model with traction versus slide-roll ratio data from other researchers [3] and with traction versus sideslip data from our laboratory showed that the model was essentially correct for isothermal conditions.

Since the lubricant was usually in the amorphous solid condition when the limiting shear stress was measured, it was expected that the history of the formation of the solid influenced the limiting stress values measured. In the previous report [1] it was shown that the isothermal compression history produced a limiting stress lower (and more characteristic of EHD) than the previously used isobaric cooling process. The pressure range was extended for limiting stress and shear modulus measurements and the capability of measuring these properties with solid polymers was added. The yield shear stress behavior of the solid polymers was found to be comparable to that of the liquid lubricants.

During the current year, measurements were made of the limiting shear stress for two naphthenic oils of differing molecular weight and three blends of the lower molecular weight oil and polyalkylmethacrylate polymers of differing molecular weight. The two base oils reached the same limiting shear stress for the same temperature and pressure. This was also true for all the polymer solutions although the polymer reduced the limiting shear stress by about fifteen percent. It seems that limiting stress is more a function of material type than viscosity or molecular weight.

A new falling body viscometer was constructed to operate to 230C and to 0.6 GPa. Another viscometer was constructed to extend the pressure range to 1.1 GPa.

2

A new concentrated contact simulator has been developed which allows recording of the traction force while the slide-roll ratio is continuously varied and the rolling speed is maintained essentially constant by a single drive motor. The configuration is that of a crowned roller against a disk. Preliminary results are promising and further development is expected to yield the capability of measuring the effect of kinematics and lubricant properties on the linear, low slide roll ratio portion of the traction curve.

Measurement of lubricant minimum film thickness of elliptical EHD contacts of various aspect ratios were made by optical interferometry. The data collected were used to evaluate the Hamrock and Dowson minimum film thickness model over a range of contact ellipticity ratio where the major axis of the contact ellipse was aligned both parallel and perpendicular to the direction of motion. A statistical analysis of the measured film thickness data showed that on the average the experimental data were thirty percent greater than the film thickness predicte by the model.

Preliminary development of the application of a scanning infrared radiation system to a tribo-system was completed. A commercial scanning IR detector was employed to measure the radiation from an especially constructed elastohydrodynamic device and from a commercial Timken type tester. The scanning rate was twenty-five frames per second. The effor described in this report obtained data by photographing the CRT display. Currently, efforts are underway to record the video signal for post anal which is expected to greatly enhance both the spatial and time resolutio of the information.

An analytical study was undertaken for the film thickness developed in line contacts under pure rolling conditions employing the limiting shear stress rheological model in the various lubrication regimes (rigid surfa isoviscous lubricant, rigid surface-variable viscosity lubricant, elasti deforming surface-isoviscous lubricant, and elastically deforming surfac variable viscosity lubricant). Comparisons were made in all cases with the corresponding Newtonian lubricant cases.

II. LUBRICANT SHEAR RHEOLOGICAL MEASUREMENTS

Experimental Apparatus

Lubricant shear rheological measurements were conducted on several materials and in several devices. The devices were both those for measuring primary properties (viscosity and limiting shear stress) and a traction rig for measuring traction versus contact kinematics. Some of the devices were constructed as part of this year's effort.

Several pieces of apparatus were employed. They consist of devices to measure limiting shear stress, viscosity and traction. The latter two, as explained, were constructed as part of this year's effort.

Measurements of shear properties of fluids in the amorphous solid condition were conducted in the Constant-Pressure Stress-Strain Apparatus which is described in the previous year's annual report [1].

A new falling body viscometer (Figure 1) was constructed to operate to 230C and 0.6 GPa. The higher temperature capability is due to new designs of the linear variable differential transformer and the vessel closure seal. In addition, the falling body now translates within a loose fitting sleeve inside the pressure vessel so that changes in vessel bore diameter with temperature and pressure do not affect the viscometer calibration. The sleeve is closed at one end and sealed at the other by an isolating piston forming a removable viscometer cartridge which holds about 2 cm^3 of sample.

In addition, a new viscometer was constructed to extend the pressure range to 1.1 GPa. In this design (shown in Figure 2) the pressure generating intensifier is incorporated in the viscometer and supports a portion of the outside diameter of the soft non-magnetic vessel for use above 100C the intensifier is forced air cooled. A viscometer cartridge similar to that described above is used.

A new concentrated contact simulator (Figure 3) was developed and is nearing completion which allows recording of traction force and infrared surface temperature while the slide-roll ratio is continuously varied and the rolling speed is maintained essentially constant by a single variable speed drive motor. The configuration is that of a crowned roller against the face of a disc. The disc is loaded against the roller by weights acting through a thrust bearing and keyed to prevent rotation. The sideslip angle is adjusted from approximately zero to 0.05 radians by means of a micrometer which tilts the disc rotational axis about a lower support bearing. The angular velocity of the roller and disc are coupled at a fixed ratio while the sliding velocity is varied by varying the distance from the contact to the axis of the disk. A change in slide-to-roll ratio (Σ) of 0.14 can be continuously scanned about a mean value of slide-to-roll ratio which is variable in larger increments. A preliminary traction curve is presented in

Figure 4 which shows the effect of side slip angle.

Rheological Experiments and Results

Flow curves (shear stress vs. shear rate) were generated using the
constant pressure stress-strain apparatus for two naphthenic mineral
oils of differing molecular weight and viscosity and three blends of
the low viscosity oil and four percent by weight of polyalkylmethac-
rylate polymers. The polymer-molecular weights were 3.5 x 10^5,
6 x 10^5, and 20 x 10^5. The material history for measurements in the
amorphous solid regime was that of nearly isothermal compression
from the liquid phase. Fluid descriptions can be found in Appendix A.

In Figure 5, two flow charts are presented for the low viscosity
naphthenic base oil (R620-15) for pressures of 1.09 and 0.93 GPa
respectively. In each case the temperature is varied. At the higher
temperatures linear viscous behavior is evident at the lowest shear
rates. Also, increasing the temperature apparently lowers the limit-
ing shear stress. Figure 6 shows the shear behavior of both the low
viscosity base oil (R620-15) and the high viscosity base oil (R620-16)
at 26C and various pressures. Included are results for the low vis-
cosity oil at 46C. It can be seen that lowering the pressure reduces
the limiting shear stress and brings on viscous behavior at low shear
rate. Fluid descriptions can be found in Appendix A.

Blends of polyalkylmethacrylate and the low viscosity oil were prepared
and run in the stress-strain apparatus at 26C (Figure 7). Aside from
viscosity differences their behavior is apparently the same.

In Figure 8 curves are drawn exclusive of the data points for the two
base oils and three polymer blends at 26C and .93 GPa. For this par-
ticular temperature and pressure, the base oils reached essentially
the same limiting stress. This was also true of the polymer solutions
although the polymer reduced the limiting stress of the base oil by
about fifteen percent. It seems that the limiting shear stress is
more determined by material type than by viscosity or molecular weight.

Following completion of the high temperature viscometer, a pressure
viscosity isotherm was generated for 5P4E (polyphenyl ether) at 227C
(440F) to 0.5 GPa as shown in Figure 9 along with previously presented
low temperature data. In Figure 10 are four isotherms for R620-15
developed with the instruments indicated on the figure. At 149C data
was taken to a pressure of 1.07 GPa.

Figure 11 is a collection of pressure-viscosity isotherms for the two
base oils and two of the polymer blends at 29, 99 and 227C. Pressure
viscosity coefficients for these materials are tabulated in Table 1.

Since the low shear rate portion of the flow charts in Figures 4, 5 and 6 shows viscous behavior, it is informative to plot the low stress viscosity calculated from these charts on the respective isotherms shown in Figure 10. This was done in Figure 12. Although there is a large pressure range in which no data is available, the extrapolated isotherms from the falling body experiments can be reasonably extrapolated to fit the data from the stress-strain apparatus. This provides us with a further tool for extending the limits on pressure and viscosity with respect to viscosity measurement. Note that at very high pressure the polymer thickener has reduced the viscosity of the naphthenic solvent, although at low pressure it has increased it. This unexpected result is seen to have been observed with both instruments.

III. AN EXPERIMENTAL EVALUATION OF THE HAMROCK

AND DOWSON MINIMUM FILM THICKNESS EQUATION

FOR FULLY FLOODED EHD POINT CONTACTS

Introduction

The research reported in this section was the result of the Masters
degree thesis research of Mr. K. A. Koye [4] and will be presented at
the ASME/ASLE International Lubrication Conference in August 1980
and published in Transactions ASME, Journal of Lubrication Technol-
ogy in substantially the form presented here.

The minimum thickness of the lubricating film separating the surfaces
in an EHD contact is of primary interest to a design engineer con-
cerned with such contacts. The successful separation of the surfaces
under the anticipated operating conditions can significantly increase
the useful life of the machine parts involved. If separated, the
failure mode will be the long term limitation of surface fatigue.
If the surfaces are not separated adequately, surface interaction
will shorten the contact life and may even result in sudden scuffing
failure.

The purpose of this study was to determine experimentally, for a prac-
tical range of ellipticity ratio, the effect of contact geometry on
minimum film thickness in a fully flooded isothermal EHD point contact
in pure rolling. Further, it is intended to use the data collected to
statistically examine, by regression analysis, the Hamrock and Dowson
minimum film thickness equation

$$H_{min} = 3.63 \ U^{0.68} G^{0.49} \ W^{-0.073} (1 - e^{-0.68k}) \tag{1}$$

Hamrock and Dowson [5-8] only intend this equation be used for
ellipticity ratios greater than one ($k \geq 1$) and it is speculation on
the authors' part that it is valid for ellipticity ratios less than
one ($k < 1$). As the experimental results show, this speculation is
justified.

In addition, the applicability of the Hamrock and Dowson film thick-
ness equation to contacts aligned with the major axis in the direc-
tion of rolling is evaluated.

The objective of the experimental work performed was to obtain EHD
film thickness measurements for a number of ellipticity ratios, for
each of the above alignments of the major axis, at various levels of
dimensionless speed and load. The dimensionless material parameter
was maintained constant. The dependent variable, dimensionless film
thickness, was obtained for each set of independent variables: speed,
load, and ellipticity ratio (or radius ratio), and the results then
compared with the predictions of the Hamrock and Dowson model.

Nomenclature

a	contact ellipse dimension perpendicular to the direction of motion
b	contact ellipse dimension parallel to the direction of motion
$k = a/b$	ellipticity ratio
$E' \equiv 2 \left[\dfrac{1-\nu_1^2}{E_1} + \dfrac{1-\nu_2^2}{E_2} \right]^{-1}$	E_1, E_2 and ν_1, ν_2 are elastic moduli and Poisson's ratio for body 1 and 2
F	load
$G \equiv \alpha E'$	dimensionless material parameter
$U \equiv \dfrac{\mu_o\, u}{E' R_x}$	dimensionless speed parameter
$W \equiv \dfrac{F}{E' R_x^2}$	dimensionless load parameter
h	film thickness
$h_{min.exp.}$	measured minimum film thickness
h_{min}	minimum film thickness calculated by
$H_{min} = \dfrac{h_{min}}{R_x}$	dimensionless minimum film thickness
r_x, r_y	roller radii parallel (x) and perpendicular (y) to direction of motion
R_x, R_y	equivalent principle radii of curvature of the contacting surfaces parallel (x) and perpendicular (y) to the direction of motion

$$R_x \equiv \frac{R_{x1}\,R_{x2}}{(R_{x1} + R_{x2})}$$

$$R_y \equiv \frac{R_{y1}\,R_{y2}}{R_{y1} + R_{y2}}$$

where

$R_{x1},\ R_{x2},\ R_{y1},\ R_{y2}$ are the radii of surfaces 1 and 2 in the direction of motion (x) and perpendicular to it (y)

$u \quad \equiv \frac{1}{2}\,(u_1 + u_2)$ average rolling velocity

u_1, u_2 velocity of surface 1 and 2

μ_o absolute viscosity at EHD inlet temperature

α pressure viscosity coefficient at inlet temperature

Experimental Apparatus

EHD Simulator

The apparatus used to create conditions similar to those encountered
by the contacting surfaces in rolling element bearings and gear teeth
is shown in Figure 13. The principal parts of the EHD simulator are
the contacting surfaces of a hardened steel crowned roller and a flat
synthetic sapphire disk.

The crowned roller is mounted in pillow blocks containing radial ball
bearings (9.525 mm I.D.) on an aluminum block with a slot milled just
below the surface of the crowned roller which serves as an oil bath.
The crowned roller support is shown in Figure 14.

The sapphire disk is mounted in a ball thrust bearing (11.0 cm O.D.)
and is driven about an axis perpendicular to that of the roller rota-
tion. The sapphire is driven through a bevel gear drive by a d.c.
servo motor (0.15 HP).

The sapphire in its thrust bearing and its complete drive system are
mounted on the contact loading lever. The load at the contact was
4.4 times the load at the end of the lever arm. A viscous damping
mechanism was used to eliminate mechanical vibrations and keep the
load constant.

The speed of the sapphire was measured by an optical tachometer which
was connected to the drive motor shaft through a flexible coupling.
The tachometer provided an input signal of fifty counts per revolution
to a digital counter.

To insure near pure rolling conditions (surface velocities equal) the
speed of the crowned roller was also monitored. Pure rolling was
desired to avoid the increase in lubricant temperature and subsequent
decrease in inlet viscosity due to the viscous energy dissipation
associated with sliding. A bifurcated fiber optics bundle was aimed
at an extension of the roller shaft to which two bars of reflective
plastic were glued 180° apart. The light transmitted and received
by the fiber optics bundle was conditioned into an electronic signal
of two counts per revolution as input to a digital counter. The bulk
fluid temperature was also monitored with a thermocouple attached to
a digital thermometer.

Description of the Bearing Surfaces

The crowned rollers were cut from 3.81 cm diameter A-2 tool steel bar
stock. A-2 tool steel was selected for its machinability and harden-
ability. In some cases cutting tools with the desired crown radius
were milled from 0-1 tool steel and then used to cut the radius into
the roller surface. For the smaller crown radii, less than 7.9 mm,

and the larger, greater than 15.9 mm, a step was cut into the roller of approximately the desired crown diameter in width. This step was then sanded which resulted in a curved surface. The finished rollers were then hardened to a Rockwell hardness of Rc 60. The hardened rollers were then sanded and polished with emery and polishing paper to a surface roughness of less than 0.13 μm (Arithmetic Average).

The actual finished crown radius of a roller was determined by measuring the ellipticity ratio of the elliptical contact produced by loading the sapphire disk against it in the EHD simulator. The rolling radius of the roller was measured with a micrometer. Thus knowing the ellipticity ratio and the radius in the direction of motion the crown radius could be determined from the relationship,

$$k = 1.0339 \ (R_1/R_2)^{0.636}, \quad R_1 \geq R_2 \ \text{ and } \ k \geq 1$$

derived numerically by Brewe and Hamrock [9] from Hertzian contact stress theory.

The geometry of the crowned rollers used in this investigation is given in Table 2. The physical properties of A-2 tool steel are given in Appendix B.

The synthetic sapphire (Al_2O_3) disk was chosen for its strength and hardness. In addition, it has the optical properties, transparency and refractive index, necessary for optical film thickness measurement. The disk measured 8.89 cm diameter by 0.32 cm thick with a surface roughness of 0.00635 μm A.A. and optically flat to within an eighth of a wavelength. The EHD contact surface of the disk was coated with Inconel to give a partially reflective surface.

The lubricant used was a naphthenic base mineral oil (Sunoco R-620-16). It was selected for its base viscosity at room temperature, which would insure an adequate film formation in the smaller contacts. The properties of the lubricant crucial to the film thickness equation, namely, inlet viscosity and pressure-viscosity coefficient, were measured in the Tribology Laboratory at Georgia Tech at temperatures near the operating temperature. The results of these measurements are given in Appendix B, along with other physical properties of the lubricant.

Optical Interferometry Film Thickness Measurement Technique

The optical interferometry technique for measuring EHD film thickness which was used in this investigation was developed by Foord, Wedeven, Westlake, and Cameron [10]. The technique was adapted for use on the EHD simulator used by Nagaraj [11].

A dichromatic light source was directed onto the vertical illuminator of a Leitz Metallurgical microscope to which a Polaroid camera had been mounted. The film thickness in the contact could be deduced from a color photograph of the interference pattern of the dichromatic light reflected up into the camera from the contact.

The optical arrangement used in the experimental investigation is very similar to that of Foord et al. [10]. A dichromatic light source was used which consisted of a 5460 Å green band and a 6300 Å red band. The dichromatic incident light source produces an interference pattern which consists of three predominant bright fringe colors and one dark. The three bright fringes were red, green and yellow, and the dark fringe appeared black. In between the sharp, distinct, bright and dark fringes there appeared shades of the predominant colors. The sequence in which these colors appeared varied over 2.3 μm of film thickness and then repeated.

The effect of temperature and pressure on the refractive index of the lubricant has been considered by Nagaraj [11]. Nagaraj reported the variation in refractive index due to pressure variations over the contact area to be less than ten percent for a system very similar to the one used in this investigation. In addition he reported a two percent change in film thickness for a 50 percent error in Hertz pressure estimate at 0.65 GPa, and a 1.5 percent change in refractive index for a temperature rise from 38C to 100C at 0.138 GPa. Therefore, the effect of temperature and pressure on refractive index of the lubricant were neglected in the calculation of film thickness.

The optical system used in the experimental measurements of EHD film thickness is shown schematically in Figure 15. A continuous collimated light source directs a beam of light down an optical bench into the vertical illuminator of the microscope. An aperture was used to control the amount of light from the 30 watt, variable intensity light source. The light then passes through a dichromatic filter and a condensing lens system.

The continuous light source was used to focus the interference pattern of the static EHD contact and observe films of contacts where the surface velocity was less than 10 cm/s. The EHD contact became increasingly more dynamic in the field of view of the microscope with increasing rolling speeds. This motion of the EHD contact was due to slight mechanical misalignments which are magnified by the microscope. At speeds over 10 cm/s it was necessary to photograph the interference pattern reflected from the contact with an exposure time short enough to stop the motion of the contact. A flash unit with flash durations from 30 to 40 microseconds was found to provide the correct exposure for Polaroid Type 58 Land Film when the flash unit's thyristor circuitry control for flash duration was set at manual. A Polaroid four inch by five inch film holder and camera were mounted on top of the microscope.

Experimental Technique and Method of Analysis

Design of the Experiment

The experimental procedure used to obtain minimum film thickness
measurements was designed around two primary considerations. These
considerations were first to use a practical range of dimensional
speed, dimensional load, and ellipticity ratio in obtaining film
thickness data from EHD contacts, and second, to use a sufficient
number of data points within each range to obtain a meaningful
regression analysis.

The Hamrock and Dowson equation for minimum film thickness, Equation
(1) contains four independent dimensionless variables. The equation
was developed for values of ellipticity parameter (k) greater than
one. The dimensionless material parameter G was not varied in this
investigation and was 10451. Thus, for each ellipticity ratio
examined only the dimensionless speed and dimensionless load were
varied and this variation was achieved primarily by varying the
applied load and the rolling velocity of the bearing surfaces.
(There was some variation in the rolling radius R_x caused by finish-
ing the crowned contact surfaces of the steel rollers.)

The Hamrock and Dowson minimum film thickness equation predicts the
effect of contact geometry on minimum film thickness in EHD contacts
to be most prominent for the range of ellipticity ratio between 0
and 4. The relationship between ellipticity ratio and minimum film
thickness as expressed by the Hamrock and Dowson equation is illus-
trated in Figure 16, which shows less than a ten percent effect of
ellipticity ratio on minimum film thickness above k = 4.

Early experimental work concerned with film thickness in EHD point
contacts by Archard and Cowking [12] reports similar conclusions
with respect to the effect of contact geometry (particularly side
leakage) on film thickness in EHD contacts with ellipticity ratios
in the range 0.48 < k < 5.02. Recent work by Bahadoran and Gohar
[13] shows no significant effect of ellipticity ratio on film thick-
ness in the range 3.5 < k < 7.5, which supports the upper part of
the curve in Figure 16. Gledhill, Jackson, and Cameron [14] inves-
tigated low ellipticity ratios (k $\sim$ 0.1) while studying the EHD of
asperities. Therefore, the range of interest for ellipticity ratio
in this investigation was chosen as being 1/8 < k < 4. Beginning
at the low end of this range and moving up, the practical applica-
tions of this range of ellipticity ratio include: micro-elastohydro-
dynamic lubrication of surface asperities, worm gear contacts,
roller-bearing rolling element-race contacts, and contacts in gear
teeth.

Dimensional speed and load ranges were chosen to cause the dimen-
sionless speeds and loads to lie within the ranges used by Hamrock
and Dowson in the numerical procedure used to develop their minimum

film thickness equation. These ranges of dimensionless speed and load were maintained for all but a few cases at the extreme ends of the ellipticity ratio range. The few cases which did lie outside the desired range of dimensionless speed and load used by Hamrock and Dowson never did so by more than an order of magnitude.

The range of dimensionless speed maintained was

$$2.14 \times 10^{-11} < U = \frac{\mu_0 u}{E'R_x} < 8.90 \times 10^{-11} \quad ,$$

which, for the mechanical system used in this investigation (with an average rolling radius taken as R_x = 1.5875 cm) correspond to a speed range of, 31 cm/s < u < 128 cm/s. The range of dimensionless load maintained was

$$0.038 \times 10^{-6} < W = \frac{F}{E'R_x^2} < 5.32 \times 10^{-6} \quad ,$$

which corresponded to a range on dimensional load of 2.74 N < F < 384 N.

For each ellipticity ratio examined, three levels of speed and three levels of load were selected from within the ranges mentioned above. This resulted in nine cases of speed and load for each ellipticity ratio, except for a few sets of speed and load which were prohibited by equipment limitations. The levels at which speed and load were set were selected in equal logarithmic intervals of each other.

The rolling velocities used were 50, 90 and 125 cm/s for every ellipticity ratio at every load except for k = 0.117, where 30, 50 and 90 cm/s was used. (Photographing this contact was difficult at high velocities.) These rolling velocities were selected as being at a level of practical application and were well suited to the mechanical drive system used to drive the sapphires rotations.

The three levels of load used for each ellipticity ratio were chosen to yield a maximum Hertz pressure in the EHD point contact of 0.69, 1.03 and 1.55 GPa (100 x 10^3, 150 x 10^3, and 225 x 10^3 psi).

The loads and speeds used were checked to insure the operating regime was in the elastic-variable viscosity (EHD) regime according to the elliptical contact regime theory of Hamrock and Dowson [15] for those cases of k ≅ 1.0, 3.0 for which regime charts are available. For the cases of k < 1, it was assumed that Hertz pressures of 0.69 GPa (100 kpsi) or more should insure operation in the EHD regime.

Experimental Procedure

Individual film thickness measurements were made by a set procedure. After the load to the contact was zeroed, the desired load to the contact was applied by placing the appropriate dead weights on the loading platform hanging from the end of the loading lever beam. The static interference pattern was located and focussed in the field of view of the microscope using the continuous light source. The flash unit was then mounted in its position on the optical bench.

Motion of the contacting surfaces was initiated by supplying power to the d.c. motor. The power was increased until the desired speed was obtained as evidenced by the readout on the display of the digital counter. The rotational speed of the sapphire was checked against that of the crowned roller to insure they were equal, which indicates pure rolling.

When the desired rotational speeds of the contacting surfaces were achieved the resulting interference pattern was photographed by opening the camera's shutter and triggering the flash unit. The entire process, from the moment motion was initiated to the moment the photograph was taken, took 60 seconds on the average. The minimum film thickness was then determined from the photograph.

In all, seven crowned rollers with seven different radius ratios were used at three levels of speed for each of three levels of load. Sixty-three film thickness measurements were individually attempted by the above procedure for the sixty-three combinations of the three independent variables of interest. Fifty-seven useful film thickness measurements were obtained. The six cases which did not prove fruitful were because of extremes in the load necessary to generate desired Hertz pressure.

Statistical Analysis of the Experimental Data

After the minimum film thickness for each of the fifty-seven combinations of speed, load, and ellipticity ratio were obtained, the film thickness results and the corresponding independent variables from Equation (1) were entered on a computer data file. This data file was used as an input file.

The minimum film thickness was calculated for an EHD point contact using the Hamrock and Dowson equation (Equation 1) given the necessary physical property data and the operating parameters (speed and load) for the solid-lubricant-solid system. Also calculated was the absolute value of the difference between the measured minimum film thickness, $h_{min.exp}$, and the calculated value, h_{min}, expressed as

$$\left| h_{min.} - h_{min.exp} \right| \quad ,$$

and the ratio expressed as

$$(h_{min.exp}/h_{min.}) \quad .$$

The variables of Equation (1) were transformed into the natural logarithm of these variables for use in a log-multilinear regression analysis.

The data stored on the output file were used as input for a Biomedical Computer Programs [16] P-series regression routine called P1R. BMDP1R estimates a multiple linear regression that relates a dependent variable to several independent variables. The routine uses a least squares method to estimate the coefficients β_1, β_2, ..., β_p and the intercept α in the equation

$$Y = \alpha + \beta_1 X_1 + \beta_2 X_2 + \cdots + \beta_p X_p + \varepsilon \qquad (2)$$

where

Y - dependent variable

X - independent variable p

ε - error

The estimates of the intercept α and the coefficients β, denoted a and b, are found by minimizing the expression

$$\Sigma \, (Y - a - b_1 X_1 - b_2 X_2 - \cdots - b_p X_p)^2 \qquad (3)$$

for all cases of dependent and independent variables supplied.

A multilinear regression analysis was performed by BMDP1R with the data supplied from the output file for the constants α and β_p in the equation

$$\ln(H_{min.exp}) = \alpha + \beta_1 \ln(U) + \beta_2 \ln(W)$$
$$+ \beta_3 \ln(1 - e^{-0.68k}) \quad . \qquad (4)$$

Perfect correlation of the experimental data with the Hamrock and Dowson model would result in values of

$$\alpha = \ln(3.63) + 0.49 \ln(10454) = 5.82$$

$$\beta_1 = 0.68$$

$$\beta_2 = -0.073$$

$$\beta_3 = 1.0$$

BMDP1R also performs univariate statistics on all the variables supplied. The statistics calculated include: mean, standard deviation, and variance. The coefficients of correlation for the regression are also supplied.

Results of the Experimental Investigation
and Statistical Analysis of the Data

Experimental Results

The measured dimensionless minimum film thickness results and the corresponding dimensionless speeds and loads for the seven ellipticity ratios examined are presented in Tables 3 through 9. In addition, the absolute value of the difference between the measured dimensionless minimum film thickness and the value predicted by the Hamrock and Dowson Equation (Equation 1), along with the quotient of the two, are also presented. Examples of the photo-micrographs used to measure minimum film thickness for each of the seven ellipticity ratios examined are presented in Figure 17 through 23 corresponding to rollers in Tables 3 through 9 respectively. The original photomicrographs were in color. The reproductions shown are from black and white high contrast photographs of the original with unfiltered light. In Figures 17 and 18 the flow is from bottom to top while in the remaining figures it is from right to left. In all cases the minimum film thickness is on the side or trailing edge depending on conditions.

Figure 24 is a plot of measured dimensionless minimum film thickness versus the dimensionless film thickness predicted by the Hamrock and Dowson model. The line $H_{min} = H_{min.exp}$ represents perfect agreement between the experimental results and the predictions of the Hamrock and Dowson model.

Results of the Statistical Analysis

The multilinear regression estimated the coefficients α, β_1, β_2 and β_3 in the equation

$$\ln(H_{min.exp}) = \alpha + \beta_1 \ln(U) + \beta_2 \ln(W) + \beta_3 \ln(1 - e^{-0.68k}) \quad (5)$$

as

$$\alpha = 7.344$$

$$\beta_1 \quad 0.751 \pm 0.045$$

$$\beta_2 = -0.097 \pm 0.021$$

$$\beta_3 = 0.955 \pm 0.010$$

Thus, the model developed by the multilinear regression analysis was

$$H_{min} = 16.60 \ U^{0.751} \ G^{0.49} W^{-0.097} \ (1 - e^{-0.68k})^{0.955} \ . \quad (6)$$

The correlation coefficient, R, product of correlation, R^2, and the standard error of the estimate for the multilinear regression were

$$R = 0.9856$$
$$R^2 = 0.9713$$

STANDARD ERROR OF ESTIMATE = 0.1439

where a correlation coefficient of one and a standard error of the estimate of zero indicate perfect correlation.

The univariate statistics performed by BMDP1R were of particular interest for the variables

$$|h_{min} - h_{min.exp}|$$

and

$$(h_{min.exp}/h_{min}) \quad .$$

The mean and standard deviation of these two variables are given in Table 10.

The ratio of experimentally measured to calculated film thickness was also examined for each ellipticity ratio. The mean and standard deviation for this statistic is shown in Table 11. As seen from these data there is somewhat of a trend for the experimental film thickness to deviate more from the calculated value for the lower ellipticity ratios. This is not necessarily attributed to the lack of predictability

of the equation at low ellipticity ratio. It can also be attributed
to the fact that the measurement technique has a minimum uncertainty
which is a larger fraction of the measured film thickness as the film
thickness decreases, as it does for the low ellipticity ratio cases.
The measurement of the film thickness is more difficult at the lower
ellipticity ratio (light loads, smaller interferograms) also. If we
restrict the comparison to ellipticity ratios of approximately one
or more, as Hamrock and Dowson intended for their equation, the mean
ratio of experimental to calculated film thickness is 1.23 and the
standard deviation about nine percent. This is only slightly better
than the overall statistics of 1.30 and 0.11 respectively.

Also examined in the statistical analysis were the residuals based on
the generated regression equation (6). These residuals and their
squares were plotted as functions of the dependent variable (calculated
film thickness) and each of the independent variables (ellipticity
ratio, speed, and load). There were no obvious trends of the residuals
with any of the variables except that the spread of them was larger
at the smallest film thicknesses as might be expected. Even in that
case the residuals were centered around zero.

Discussion

The results presented show a reasonable agreement between the measured
film thickness data and the Hamrock and Dowson model.

The regression coefficients estimated by the multilinear regression
analysis did not differ significantly from the corresponding exponents
of the Hamrock and Dowson minimum film thickness equation but the
multiplicative constant was greater by a factor of 4.5.

$$H_{min} = 3.63 U^{0.68} G^{0.49} W^{-0.073} (1 - e^{-0.68k}) \qquad (1)$$

The model developed by the multilinear regression analysis,

$$H_{min} = 16.6 \ U^{0.751} G^{0.49} W^{-0.097} (1 - e^{-0.68k})^{0.955} , \qquad (6)$$

fit the experimental film thickness data well; the correlation coeffi-
cient was $R = 0.9856$. The mean measured minimum film thickness was
within one percent of the multilinear regression model (Equation 6)
prediction with a standard deviation of 13.98 percent. The F-ratio
from this regression analysis was 666.767 with three degrees of freedom
in the regression and 59 degrees of freedom in the residual. Applying
the F-ratio test, this implies that the independent variables used
(speed, load and ellipticity ratio) account for the variation of the
dependent variable (film thickness) at the 99.999 percent confidence
limit (P(tail) = 0.00000).

Evidence of the correlation between the measured film thickness data
and the Hamrock and Dowson model can be found in Table 10 and 11. The
mean difference between measured and predicted minimum film thickness
was 6.682 μin. (0.17 μm). The mean percent difference was 30.2 per-
cent and the standard deviation was 21.4 percent. The mean film
thickness measured was 26.27 μin. (0.667 μm). The procedure for
measuring the minimum film thickness from the photomicrograph of
the interference pattern is only good within plus or minus 2.5 micro-
inches (0.0127 μm). Thus, for a mean measured film thickness of 26.7
microinches the experimental procedure came within 30.2 percent of the
Hamrock and Dowson equations prediction, 8.01 μin, of which only 2.5
microinches could be attributed to lack of accuracy in measuring the
film thickness. The data presented in Table 10 show that on the average
the measured film thickness data was thirty percent more than the
Hamrock and Dowson predictions and 68 percent (i.e., ± one standard
deviation) of all of the measured minimum film thickness data were
from ten percent more than to 50 percent more than the Hamrock and
Dowson predictions. (Assuming a normal distribution of $h_{min.exp}/h_{min}$).
Figure 24 presents the dimensionless minimum predicted film thickness
from the Hamrock and Dowson equation and the corresponding experimental
measurement. It illustrates the fact that the measured minimum film
thicknesses were greater than those predicted.

However, if the comparison is restricted to the ellipticity range for
which the Hamrock and Dowson equation was intended ($k \geq 1$), it is
seen from Table 11 that the agreement between experiment and theory is
better in that the mean of the measured film thickness is only 15 per-
cent greater than the prediction and the standard derivation is also
smaller (about eight percent). Therefore in the range of ellipticity
ratio for which the equation was developed, plus and minus one standard
derivation of the experimental data range from about seven percent to
about 23 percent more than the predicted values.

As indicated it was speculative to expect the Hamrock and Dowson
equation to be applicable for ellipticity ratios less than one; a
range which was not considered by Hamrock and Dowson in developing
the equation. However, as seen from Equation (6), the multilinear
regression model developed from the data, the exponent on the ellip-
ticity function for the best fit regression is 0.955 when the entire
ellipticity range is included ($0.117 \leq k \leq 3.70$) compared to an
exponent of one on their model. This is particularly significant
when it is recalled that the ellipticity ratios in this work were the
experimentally measured values.

It is interesting to point out that the value of 0.751 for the exponent
on the dimensionless speed is close to the value of 0.744 arrived at
experimentally by Archard for point contacts, and through analytical
methods by Grubin, Crook and Dowson and Higginson for line contacts [17].

The exponent on the load term from the regression model is somewhat greater than that in the analytical equation (i.e., 0.097 compared to 0.073) which indicates the experimental data exhibited a somewhat greater dependence on load than expected.

In this experimental work every effort was made to assure conditions that were assumed in developing the Hamrock and Dowson equation except for considering k < 1 and the material parameter (G = 10451) which was greater than Hamrock and Dowson range. Of their 34 cases considered 31 were for G = 4522 and one each at 2310, 3491, 6785. There was a good knowledge of the properties of the lubricant, particularly viscosity and pressure viscosity coefficient, at the operating conditions. The lubricant was Newtonian. Thermal effects were minimized to satisfy the isothermal assumption. The roller support assembly used was free of any extraneous frictional effects at the contact surface. In addition, by photographing the contact interference pattern within one minute of the beginning of motion, individually for each set of conditions examined, little time was allowed for bulk thermal effects to develop in a rolling contact, (as opposed to a sliding contact). The bulk fluid temperature of the lubricant was never noted as having varied more than $0.5C$ ($1^{\circ}F$) about $23C$ ($74F$). In spite of these precautions, the mean measured minimum film thickness was 30 percent greater than the predicted values calculated from the Hamrock and Dowson equation (1).

Conclusions

The collective results of the evaluation of the Hamrock and Dowson model for minimum lubricant film thickness in elastohydrodynamic point contacts support the model. In addition, there was no significant deviation of the model from the experimental data for any particular range of ellipticity ratio examined. The mean measured minimum film thickness was 30 percent greater than the Hamrock and Dowson prediction (with a standard deviation of 21.4 percent). Therefore, it is the conclusion of this evaluation the Hamrock and Dowson model conservatively predicts the minimum film thickness in EHD contacts within the accuracy normally required in mechanical design calculations for the entire range of ellipticity ratio examined (0.117 < k < 3.7). The apparent advantage in accuracy of the model developed by the multilinear regression analysis (Equation 6) compared with the Hamrock and Dowson equation (Equation 1) (one percent versus 30 percent on average) may not justify recommending Equation (6) over the well-known Hamrock and Dowson equation (Equation 1).

It is also concluded from this study that the Hamrock and Dowson equation can be applied to contacts with the major axis aligned in the direction of motion. With respect to the definition of ellipticity ratio, given by Hamrock and Dowson as the ratio of the

semi-major axis to the semi-minor axis of the contact ellipse, the
authors would like to suggest that the variable k in Equation 1 be
redefined as the ratio of the axis of the contact ellipse perpen-
dicular to the direction of motion to the axis parallel with the
direction of motion since the former definition precludes a value
of k less than one. This would permit the application of the
Hamrock and Dowson equation for contacts with the major axis of
the contact ellipse aligned in the direction of motion, an orienta-
tion which has important implications but which is outside the stated
range of applicability for their equation.

IV. SIMULTANEOUS TEMPERATURE MAPPING AND TRACTION
MEASUREMENTS IN EHD CONTACTS

The research presented in this section was in part conducted by
Mr. E. H. Kool as his Master's degree thesis research [22]. It
was also presented at the 1979 Leeds-Lyon Conference and will
be published in the conference proceedings in substantially the
present form.

Introduction

One perspective of the contact temperature problem is to divide
the temperature rise in the contact into two parts: 1) the bulk
temperature rise, and 2) the local flash temperature rise. The
bulk temperature is "a temperature representative of a fairly
uniform level of those parts of the temperature fields in the
rubbing bodies that do not lie too close to the conjunction zone"
[18] and the flash temperature is "the maximum temperature (rise
above the bulk temperature) occurring in the conjunction zone"
[18]. Past research has been primarily directed toward the flash
temperature component. However, when one gets to specific cases
both the bulk and flash temperatures are difficult to predict in
a tribological system. In his 1969 review, Blok [18] presented
an adaption of the network theory in heat transfer to predict
bulk temperatures. Since that time several routine programs have
become available which can be used to predict bulk temperatures
in complex systems subject to the extent of understanding of
input parameters such as convection coefficients which are not well
defined in most tribological systems.

A major objective of the research reported here was to develop a
technique in which both bulk and flash temperatures could be
measured in a tribological system as a function of time and space.
A scanning infrared photometer was employed which covered a region
including the conjunction region. Several commercial instruments
were evaluated and are compared. One device was further employed
in several tribological experiments reported.

Infrared Temperature Measuring Technique

In the previous infrared temperature measuring work in this laboratory
[19, 20, 21] a single spot microdetector (Barnes RM2A) was used.
To automatically scan the region of interest a different IR system
was required. Several were commercially available and considered.

A brief discussion of the relative characteristics of several instruments is presented in Appendix C. The discussion below pertains to the AGA 750 which was used primarily because it was available to us at no cost from the School of Architecture at Georgia Tech and met most of our requirements.

Radiation Contributions

Figure 25 shows the various sources contributing to the radiation received by the detector from the scanned area of the ball in the EHD simulator.

The four contributions N_b, N_f, N_s and N_o are the nonattenuated values of radiations emitted by the ball, fluid, sapphire and the ambient respectively. Each of the above contributions is associated with an attenuation factor which includes absorption losses in various media and Fresnel reflection losses at interfaces between any two media.

The ball surface, being opaque, only emits and absorbs. The fluid and sapphire are partially transparent and partially absorbing media. The ambient radiation refers to the background radiation from surrounding objects in the room reflected by the ball. The radiation collected by the detector-lens is the sum of all the above contributions and is given by

$$N = \eta_b N_b + \eta_F N_F + \eta_s N_s + \eta_o N_o .$$

One infrared filter was used to partially eliminate the contribution from the fluid, and is chosen based on the spectral emission characteristic of the lubricant used (Fluid Nl, See Appendix D for lubricant definition). The spectral characteristics of the lubricant at 20C and the IR filter are shown in Figure 26. The emission curve for the fluid corresponds to a film thickness of 25 μm sandwiched between two 16 mm thick sapphire disks. This unit shows that the lubricant emission is in the range of 3.1 - 3.7 μm with peak emission at 3.4 μm. By using the wide band, high pass filter, all IR emission below 3.75 μm, thus all fluid emission is eliminated.

The dotted lines in Figure 26 show the monochromatic black body radiation as a function of wavelength at two different temperatures, plotted in arbitrary units. These curves show that the spectral region of interest in this study is to the left of the peak in black body radiation, even at temperatures of 177C. The ball radiation, which can be considered grey body radiation (emissivity is constant over all wavelengths) is therefore more predominant in the region of 3.75 - 5.5 μm compared with the region below 3.75 μm.

Radiation Analysis

The ball radiation N_b is given by the expression $N_b = \varepsilon_b \cdot k\, N_{BB}\, (T_b)$. The quantity ε_b is the emissivity of the ball surface and has been determined to be essentially constant and equal to 0.21. T_b is the ball surface temperature. $k\, N_{BB}\, (T_b)$ stands for the observed black body radiation at temperature T_b after filtering by the IR filter. The factor k is a dummy factor to make distinction between filtered and unfiltered radiation. Since the variable $k\, N_{BB}\, (T)$ is dependent on the geometry and sensitivity of the detector and also on the IR filter characteristics, a calibration was necessary. By using a calibrated black body source, the calibration of the modified AGA 750 unit with three extension rings and the wide band filter was performed.

The ball attenuation η_b is dependent on the optical properties of the sapphire and oil. The attenuation factor is determined by reflection losses at the sapphire-oil and sapphire air interfaces and absorption in the sapphire and lubricant film. Therefore

$$\eta_b = \tau_s (1 - \rho_1)(1 - \rho_2)\ \tau_F(h,T_F)\quad .$$

Since the IR filter used eliminates all radiation of wavelength lower than 3.75 μm, all radiation absorbed in the oil would be eliminated at lower temperatures. This makes $T_F(h,T_F)$ equal to 1. From [11] the following data for sapphire transmissivity and fresnel reflections are obtained

$$\tau_s = 0.97,\ \rho_1 = 0.076,\ \rho_2 = 0.0064\quad .$$

As total result

$$\eta_b N_b = \eta_b \varepsilon_b\ k\, N_{BB}(T_b) = 0.187 * k\, N_{BB}(T_b)$$

It should be noted that η_b in this situation is equivalent to the attenuation of the sapphire radiation (η_s).

By using the wide band IR filter, the radiation coming from the fluid, N_F, is eliminated at low temperatures. Therefore $\eta_F * N_F = 0$.

The contribution from the sapphire disk is difficult to analyze and, as shown before, is very small. Neglecting this radiation would not effect the accuracy tolerance of the temperature determination.

Ambient radiation, that enters the infrared camera lens is mostly reflected by the sapphire and ball. This radiation can be divided into two parts as illustrated in Figure 27. The "ambient" (1 and 2) can be assumed as a uniformly distributed radiation source with emissivity 1 and radiation level according to that of a black body at "room temperature". Because the IR lens is transparent, and the detector is cooled inside, less radiation [19] will be emitted to the ball and sapphire for reflection. Since the ball is very reflective, the image of the lens is a dark spot on the ball. Experimentally it is found that the size of this lens image is three times the maximum contact diameter. Good alignment will provide a situation where the EHD contact is in the center of the dark spot.

The amount of ambient radiation from 1 and 2 that is observed by the detector, can be determined in the following way

$$k \, N_o = \varepsilon_o \, k \, N_{BB} \, (T_o) = k \, N_{BB} \, (T_o) \quad .$$

Because the ambient has a uniform temperature distribution, it acts like a black body at room temperature; the emissivity is therefore equal to 1.

The ambient attenuation is dependent on the three different paths of the radiation as demonstrated in Figure 25. This results in the following formulation of η_o

$$\eta_o = \underbrace{\rho_1}_{\text{1st reflexion}} + \underbrace{\tau_s^2 \, (1 - \rho_1)^2 \, \rho_2}_{\text{2nd reflexion}} + \underbrace{\rho_b \, \eta_s^2 \tau_F \, (2h, T_F)}_{\text{3rd reflexion}}$$

Numerical values for these properties were found in [11]. By using the IR filter, $\tau_F(2h, T_F)$ will equal 1 and the other property values inserted in the η_o formulation will give

$$\eta_o = 0.076 + (0.97)^2 * (1 - 0.076)^2 * 0.0064$$
$$+ \, 0.79 * (0.89)^2 * 1$$

The observed ambient radiation outside the dark spot is therefore

$$\eta_o \, k \, N_o = 0.7076 \, k \, N_{BB} \, (T_o) \quad .$$

Inside the dark spot the influence of ambient source 3 is important. Because the transmissivity of the infrared camera lens is not known,

no analytical determination of radiation reduction could be made. Experimentally it was found that the loss of ambient radiation at room temperature after filtering valued approximately 0.4 Isotherm Units (ISU).

The total observed radiation by the detector is as follows:

outside dark spot:

$$kN \begin{cases} = 0.187 * k\ N_{BB}\ (T_b) + 0.7076 * k\ N_{BB}\ (T_o)\ [ISU] \\ \\ \text{in dark spot:} \\ \\ = 0.187 * k\ N_{BB}\ (T_b) + 0.7076 * k\ N_{BB}\ (T_o) - 0.4\ [ISU] \quad . \end{cases}$$

From the radiation formula outside the dark spot, the influence of the sapphire radiation can be obtained. Suppose a situation where the ball and ambient have equivalent temperature

$$kN = 0.187 * k\ N_{BB}\ (T_o) + 0.7076 * k\ N_{BB}\ (T_o)$$

$$= 0.8946 * k\ N_{BB}\ (T_o)$$

Expected is

$$kN = 1\ x\ k\ N_{BB}\ (T_o)\ .$$

The difference is the loss of radiation in the sapphire disk. Part of this will be emitted as infrared sapphire radiation and part will be transformed into a different type of energy and will be dissipated in a different way.

Ball-surface Temperature Determination

Under operating conditions the scanning device will provide a picture of the ball in the EHD region and a small part of the sapphire disk holder. Because the temperature change of this sapphire holder during one test is not more than $4^o C$, its radiation level can be determined. The black spots on the sapphire holder can be considered to be on the radiation level of a black body at the temperature during operation and will be referred to as $\Delta N (= N_{BB}(T_{SH}))$. Relative to this level, the level of all other points in the picture can be measured with isotherm level settings. This relative level will be referred to as ΔR. The radiation level of any point on the ball is

in the light region:

$$kN = \Delta\ kN + \Delta R = 0.187 * k\ N_{BB}(T_{ball}) + 0.7076 * k\ N_{BB}(T_{amb})$$

in the dark spot:

$$kN = \Delta kN + \Delta R = 0.187 * k\ N_{BB}(T_{ball}) + 0.7076 * k\ N_{BB}(T_{amb}) - 0.4.$$

Therefore

$$k\ N_{BB}(T_{ball}) = \frac{\Delta kN + \Delta R - 0.7076 * k\ N_{BB}(T_{amb}) + (0.4)}{0.187}\ .$$

By using the calibration curve, the ball radiation level will give the ball temperature.

The IR analysis for the Timken-type friction tester described below is less complicated than that for the EHD device because there is no sapphire plate and the magnification used was much less, hence, eliminating the reflected black spot.

The Tribological Devices and Method

Two devices were studied with the IR scanning system discussed above. One was a sphere on flat EHD simulator designed specifically for the work and the other was a commercially available LFW-1 Timken-type tester. These two devices are shown schematically in Figures 29 and 30.

EHD Simulator

The simulator was a ball driving a sapphire disk. The disk is mounted vertically in order to meet the infrared camera requirement of horizontal radiation detection. In this configuration the ball radiation in and around the EHD contact can be exposed to the field of view of the camera. The ball is driven through a flexible coupling and the normal load is applied by air pressure. When the traction force in the EHD contact is larger than the friction force in sapphire support bearing, rotational energy from the ball is transmitted to the sapphire disk. Both the normal and traction force are measured simultaneously by the three-dimensional piezo-electric load cell, mounted immediately behind the ball support. Rapid response is possible, because the natural frequency of this transducer is 8 kHz.

The tachometers used for the ball and sapphire speed give 20 pulses/rev and 10 pulses/rev respectively. The instrumentation is adequate for

the determination of the average velocities, but instantaneous speed changes cannot be detected.

After the machine was built and the measurement equipment installed, three major imperfections were found. Their origin and implications are discussed.

1. In order to obtain a small slide-roll ratio, the amount of friction in the sapphire support ball bearing was reduced by eliminating some balls. Out of the 15 balls in the angular contact bearing, nine were excluded and a new separating cage was built for the remaining six balls. Teflon was used as cage-material, again to reduce friction. However, the retaining cage left some room for tangential motion of the balls. The friction between the Teflon and the bearing elements was therefore not constant. This consequently led to an alternation in the traction force and sapphire speed during rolling experiments.

2. The sapphire is mounted in a holder, which is mounted inside the inner race of the angular contact bearing. Unexpected inaccuracies due to the machining operation on the sapphire holder caused the sapphire surface not to be exactly parallel to the rolling track of the balls in the outer race of the support bearing resulting in a cam action. Because of this movement the piston in the pneumatic-cylinder also moves. The change in air volume in the cylinder together with changing friction force between the piston and the cylinder-wall, were responsible for an alternating normal load in the contract. From measurements the maximum piston friction force is estimated to be 20 Newtons. Under operation conditions the average normal load was varied between 95N and 375N to create Hertzian pressures from 1.0 to 2.0 GPa. Hence the cam action caused from 5 to 20 percent load variation.

3. Alignment of the ball drive shaft with respect to the motor drive shaft was difficult. In addition, the axis of the ball shaft was moving because of the ball movement induced by the sapphire wobble. The spring elements in the flexible coupling created an axial force along the ballshaft (x direction). Therefore, the x direction force detected was a combination of traction force due to spin in the EHD contact and the axial spring force.

Only by using the very sensitive triaxial force transducer were these discrepancies between the ideal and real situation detected. However, most EHD simulators and traction drives will also have similar imperfections.

LFW-1 Standard Test Device

This device is a commercially available Timken-type test device for which there is an ASTM Standard Method (D-2714-68) to be used for calibration. The results quoted below for it were the result of following that calibration procedure. A schematic of the system is shown in Figure 30. The IR scanner viewing direction was coaxial with axis of rotation of the ring. The temperatures reported from IR method were of the side of the test block as close to the contact as could be discriminated and the lock-nut holding the ring on the shaft.

Experimental Results

EHD Configuration

Two series of measurements were made for two fluids (N1 and Santotrac 50). Because the emission spectra in the 2 μm to 5.5 μm wavelength range are almost identical, the same filter could be used to reduce fluid radiation for both fluids. The fluid properties are summarized in Appendix D.

The temperatures were determined in the following manner (See Figure 31).

1. The sapphire holder temperature is measured with a thermocouple at the beginning and end of the experiment. Usually this difference is less than 3C in rolling conditions and no more than 15C in sliding conditions. By using a timer, the total experiment duration and the time at which data is taken are known. The temperature of the sapphire holder at the time of observation can be estimated.

2. Relative to this radiation level, the radiation levels in the center of the contact and in the oil wake can be determined. At these two places the film thickness is smallest, therefore possible fluid influences are minimal.

The radiation level can be set on the scale to the left of the picture, causing all points of this radiation level to be bright white. In Figure 31a the radiation level is set for the sapphire holder and gives a value of 0.05 on the scale. In Figure 31b the radiation level is set for the oil wake and we observe this level to be 0.31. The difference in radiation levels between the sapphire holder and the oil wake is equal to the difference on the scale, multiplied by the range; thus: (0.31-0.05) * 20 = 5.2 isotherm units. In the same way the difference between the EHD center and sapphire holder is determined. By using the procedure described in the previous section, the absolute temperature and the temperature difference on the ball surface, between the EHD center and wake, can be obtained.

Measurements in Rolling Conditions

Traction and temperature measurements were simultaneously taken in the low slide-roll ratio range. The operating conditions varied in rolling speed from 0.5 m/sec to 1 m/sec; in load from 1.0 GPa to 1.9 GPa maximum Hertzian pressure. The slide-roll ratio was always less than 0.07.

Because the temperature rise was expected to be small (less than 10C), some of the measurements were performed without the IR filter. In this way, the total amount of radiation received by the detector would increase by approximately 100 percent and the difference in radiation levels could be determined more readily.

The maximum error observed in the unfiltered case was 2.25 isotherm units (ISU). Assuming a ball temperature of 40C, the temperature error range is then four degrees C. For the highest load and maximum speed the radiation difference ΔN was equal to 1.6 (ISU). Since this value is smaller than the error band, no discrete values of temperature rise can be given. Nevertheless, it can be stated from the observations that with both fluids the temperature rises under the previously mentioned EHD conditions are less than six degrees C.

From the force measurements the following results were obtained. In situations closest to pure rolling, no brake used, the average traction force in all runs was almost constant and equal to six Newton. When the brake was used, slide-roll ratio and traction force increased. The maximum values for traction coefficient were with some braking 0.08 for N1 and 0.10 for Santotrac 50.

Measurements in Sliding Conditions

The operating conditions in this series of measurements varied in ball surface speed from 0.5 m/sec to 1 m/sec and in maximum Hertzian pressure from 1.2 GPa to 2.0 GPa. The infrared filter was always used. The experimental results of temperature difference are given in Figures 32 and 33.

The system thermal transient effects required about 300 sec; the data reported were taken in steady state thermal conditions. The equilibrium traction coefficients were about 0.1 and 0.05 for the Santotrac 50 and N1 respectively.

Because the radiation levels of EHD center and the reference (sapphire holder) must appear on the same picture, a larger IR range setting (Figure 31) must be used with increased temperature difference. The temperature error band due to observation was, in this case, also 4C. During the radiation observation, a horseshoe shaped area of elevated radiation was found around the EHD contact. The maximum levels appeared at the ends of the horseshoe. Figure 34 gives an example of this observation.

An explanation for this appearance was found with help of Dr. Lauer [23]. The emission spectra of fluids are the same as the absorption spectra and are dependent on temperature and pressure. By increasing the temperature, the emission band around 3.4 μm tends to shift to a longer wavelength and also broadens. An approximation for this broadening effect is given in [24]. The halfband width is expressed by

$$\Delta\nu_{1/2} = \delta_o + A \exp \; (-U_{OR}/kT)$$

δ_o: residual width

U_{OR}: mean reorientation potential barrier

At 70C fluid temperature, it can be expected that some fluid radiation will pass the wide band filter.

In sliding conditions lubricant temperature just outside the contact area will be equivalent to the ball temperature in that region, which vary between 60C and 150C. Because the fluid radiation is a function of temperature and film thickness, the effects of fluid band broadening in the EHD center and wake are small; but outside the EHD region where the film is thick, the fluid radiation becomes observable. The accumulation of this hot fluid explains the two maxima in the horseshoe.

LFW-1 Configuration

The results presented from this configuration consist of IR surface temperatures of the friction block near the contact zone and the lock nut holding the ring in place. Temperatures of the block center and oil bath measured by thermocouples are also shown. These and friction as a function of time during a standard ASTM calibration test are shown in Figure 35. The calibration test is for steel-on-steel at a sliding speed of 7.9 m/min (26 fpm), initial Hertz pressure of 372 MPa (54 kpsi) and a bath temperature of 43C (110F). The specified oil was a "white mineral oil" unformulated. The EHD film support is negligible and wear extensive under these conditions. The band on the block contact temperature during the early part of the test is the result of changing emissivity during that time because of buildup of oil and wear debris which increases the local emissivity from 0.7 of the initial dry block surface to 0.99 of the dirty surface.

The results show that the conjunction region is always at least 5C above the block center as read by the thermocouple. The temperatures are also influenced by both the friction process and the bath

temperature which on this particular device cycles through a 13C amplitude.

Discussion of Results

The small temperature rise in rolling conditions does not, under the most severe circumstances studied, exceed seven degrees C in the work reported in [21]. This is in agreement with the result found in this work.

However, in sliding conditions the comparison gives a discrepancy. The temperature-difference values from [19-21] are much higher than those reported in Figure 32 where the same lubricant and operating conditions were employed. Two arguments are used to explain this discrepancy.

First, it should be noted that different detectors were used. The diameter of the spatial resolution of the Barnes RM2A (used in [19-21]) is 38 μm and approximately 3.3 times smaller than the modified AGA 750 (spacial resolution: 125 μm). The area over which the radiation is integrated to obtain a single-spot output, is therefore 11 times smaller for the RM2A, and the spacial resolution of the temperature distribution much better. If we consider a typical highly loaded EHD contact in our simulator (p_H = 1.5 GPa), the diameter of the contact area is approximately 500 μm. The AGA 750 minimum spotsize is about six percent of the contact while the RM2A minimum spotsize is about 0.5 percent. It was found in the previous work that the thermal gradients in the Hertz region can be very large. The spotsize area where the maximum temperature is measured, is therefore bigger with the AGA 750. The integration over this area will level the peak radiation more.

Secondly, a closer look at the surrounding conditions shows a difference in base temperature. The temperature-controlled fluid bath in [19-21] provided a constant ball and fluid temperature, except in the contact. Usually this temperature was 40C. In the measurements reported here, the base temperature was the ball temperature reached after the thermal transient. This temperature is dependent on the operating variables. The range of this base temperature varied from 60C to 140C. At these high temperatures the traction coefficient is lower and less heat generated in shearing the film. Therefore a lower temperature difference is expected.

Based on both calculations and previous measurements the film thickness to surface roughness ratio was from 4 to 40 in the EHD measurements reported here. The difference in traction coefficient between N1 and Santotrac 50 is clearly reflected in the temperature rise. The

higher traction of Santotrac 50 results in a higher contact temperature rise as would be expected.

In the LFW-1 result we see the influence of the system transient and the importance of the global thermal characteristics on the conjunction temperatures. The bath thermal control forces the level of the entire system to fluctuate. A preliminary analysis of the system suggests that the dominate mode of heat rejection is conduction out the shaft. The entire ring and shaft end are at essentially the same temperature as the block surface very near the contact region.

In general although the scanning infrared system permits determination of surface temperatures both in the contact and the surrounding region, the method of signal conditioning and display makes it difficult to follow the rapid transients and steep gradients anticipated in tribological systems. The scanned IR signal inherently contains the information for better time and spatial resolution but must be handled differently to take full advantage of it. We are currently developing an analog recording capability for post analysis of the signal which will permit a more complete display of the information.

Conclusions

An infrared scanning system has been adapted to two tribological systems. In many respects the scanner expands the versatility of the IR temperature mapping but the added complication and cost are not readily justified. The results are consistent with previous more detailed IR temperature mapping which is more tediously acquired. Further development of the signal handling approach to the scanning method is expected to make it much more valuable to tribological studies.

Acknowledgments

34

V. A FILM THICKNESS ANALYSIS FOR LINE CONTACTS UNDER PURE ROLLING CONDITIONS WITH A NON-NEWTONIAN RHEOLOGICAL MODEL

Introduction

This analysis was conducted by Mr. Burak Gecim as an extension of his Masters' thesis research and will be presented at the 1980 ASME/ASLE International Lubrication Conference and published in substantially this form in the Transactions ASME Journal of Lubrication Technology.

High viscosity fluids, especially when subjected to high rolling speed conditions may show a discrepancy in film thickness, from the predictions based on the Newtonian theory. Dyson and Wilson [27] proposed a power-low form, nonlinear constitutive equation to represent the shear rheological behavior of silicone fluids and compared the theoretical predictions with their experimental film thickness data on these fluids. But, it should be realized that lubrication with these high viscosity lubricants, especially under low loading (as in their experiment) is hardly expected to be in the EHD regime, and increasing the rolling speed results in further deviation from the EHD regime on generalized lubrication regime configurations, Figure 36. This ambiguity associated with Dyson and Wilson's analysis indicated the need of a generalized analysis of film thickness behavior with fluids which behave predominately non-Newtonian over all regimes of operation.

The present analysis utilized the nonlinear constitutive equation proposed by Winer and Bair [25], which was modified and applied in an EHD film thickness analysis by Gecim and Winer [28] for low viscosity lubricants. In [28] it was shown that low limiting shear stress parameters, which are material properties, and/or high sliding speeds are the major causes of decrease in film thickness from Newtonian theories. In the present analysis of high viscosity fluids with lower limiting shear stresses, derivations are confined to the pure rolling case and the objective is to see the effect of the low limiting shear stresses on film thickness. The analysis is carried out for a line contact geometry under pure rolling, in fully flooded full film regime, with the assumption of isothermal conditions.

Fluids of high viscosity may have a low limiting shear stress because as the material pressure is increased (or temperature decreased) at a given rate the characteristic (or relaxation) time of the high viscosity material will become equal to the characteristic time of the process at a lower pressure (or higher temperature than would be the case for a low viscosity fluid). This will result in the liquid-solid transition occurring at a lower density than for a comparable low viscosity material. The lower "frozen-in" density

will result in a lower limiting shear stress. Although this characteristic is generally expected and experimentally observed for some high viscosity silicones [2], additional measurements of limiting shear stress parameters for high viscosity fluids should be made.

Nomenclature

E_r Equivalent modulus of Elasticity $\left[= 2 \Bigg/ \left(\dfrac{1 - \nu_1^2}{E_1} + \dfrac{1 - \nu_2^2}{E_2}\right)\right]$

g_1 Dimensionless parameter for Figure 36. $\left[= \left(\dfrac{\alpha^2 (w/L)^3}{\mu_o \bar{u} \, R^2}\right)^{1/2}\right]$

g_3 Dimensionless parameter for Figure 36. $\left[= \left(\dfrac{(w/L)^2}{\mu_o \bar{u} \, E_r R}\right)^{1/2}\right]$

h Film thickness

h_o Nominal film thickness

h' Dimensionless film thickness parameter $\left(= \left(\dfrac{w/L}{\mu_o \bar{u}}\right)^{.765} \left(\dfrac{h_o}{R}\right)\right)$

m slope of the limiting shear stress-pressure relation $\tau_L = mp$

P Pressure generated in the fluid

P_H Maximum Hertzian pressure $\left[= 0.42 \left(\dfrac{w/L \cdot E_r}{R}\right)^{1/2}\right]$

P' Pressure gradient in x_1 direction

R   Equivalent Radius $\left[R^{-1} = \dfrac{R_1 \pm R_2}{R_1 \, R_2} \right]$

u_1 Lubricant velocity in x_1 direction

$\bar{u}$ Surface and rolling speed

w/L   Load per unit length of contact

x_1 and x_3 Parallel and perpendicular to the plane of film coordinate

           axis respectively

τ Shear stress in the fluid

τ_S Shear stress on the surfaces

τ_L Limiting shear stress of fluid

α Pressure coefficient of viscosity

μ Viscosity

μ_o Zero pressure value of viscosity

Shear Rheological Model and Derivations
of the Governing Equations

The non-Newtonian constitutive equation

$$\frac{du_1}{dx_3} = \frac{\tau_L}{\mu} \tanh^{-1} \left(\frac{\tau}{\tau_L} \right) \tag{1}$$

is written in terms of its Taylor series expansion as

$$\frac{du_1}{dx_3} = \frac{\tau_L}{\mu} \left[\frac{\tau}{\tau_L} + \frac{1}{3} \left(\frac{\tau}{\tau_L} \right)^3 + \frac{1}{5} \left(\frac{\tau}{\tau_L} \right)^5 + \cdots \right] \quad , \tag{2}$$

or

$$\frac{du_1}{dx_3} = \frac{\tau_L}{\mu} \sum_1^\infty \frac{1}{(2n-1)} \left(\frac{\tau}{\tau_L} \right)^{2n-1} \quad , \tag{2'}$$

and then coupled with the integrated momentum equation

$$\tau = \left(\frac{dP}{dx_1} \right) x_3 \quad \text{for} \quad -h/2 \leq x_3 \leq h/2 \tag{3}$$

where

$$\tau = \tau(x_1, x_3) = 0 \text{ at } x_3 = 0$$

as shown in Figure 37. Then the velocity distribution predicted by the model, is obtained by integrating Equation (2') subject to Equation (3) and is

$$u_1 = \bar{u} + \frac{\tau_L}{\mu} \sum_1^\infty \frac{1}{(2n-1)} \frac{1}{2n} \left(\frac{P'}{\tau_L}\right)^{2n-1} \left[x_3^{2n} - \left(\frac{h}{2}\right)^{2n}\right] \qquad (4)$$

which is integrated in the continuity equation

$$\int_{-h/2}^{+h/2} u_1 \, dx_3 = \bar{u} \, h_m \qquad (5)$$

where $h = h_m$ when $\frac{dP}{dx_1} = 0$. Then the governing non-Newtonian equation, corresponding to Reynold's equation of the Newtonian model is found as,

$$\sum_1^\infty \frac{1}{2n-1} \frac{1}{2n+1} \left(\frac{P'h}{2\tau_L}\right)^{2n-1} = \frac{2\mu\bar{u}}{\tau_L} \left(\frac{h-h_m}{h^2}\right) \qquad (6)$$

or

$$\frac{1}{2} \tanh^{-1} \left(\frac{P'h}{2\tau_L}\right) - \frac{1}{2} \frac{1}{\left(\frac{P'h}{2\tau_L}\right)} \left[\tanh^{-1}\left(\frac{P'h}{2\tau_L}\right) - \left(\frac{P'h}{2\tau_L}\right)\right]$$

$$= \frac{2\mu\bar{u}}{\tau_L} \left(\frac{h-h_m}{h^2}\right) \qquad (6')$$

where $P' = \frac{dP}{dx_1}$ and $\tau_S = |\frac{P'h}{2}|$ is the shear stress on either surface. The surface shear stresses are equal in magnitude but opposite in sign under pure rolling with the configuration shown in Figure 37. If $|\frac{\tau}{\tau_L}|_{max} = |\frac{\tau_S}{\tau_L}|$ is about 0.6 or less, then the LHS of (6') can be approximated by $\frac{2}{3} |\frac{\tau_S}{\tau_L}|$ which yields the classical Reynolds' equation. For $0.6 \leq |\frac{\tau_S}{\tau_L}| \leq 1$, the LHS of (6') can be approximated by,

$$\left[0.946 \left|\frac{\tau_S}{\tau_L}\right|^{1.616}\right] \text{ within } |5|\% \text{ Error.}$$

With this approximation the governing equation will take the form

$$\frac{dP}{dx_1} = 4.88(\mu\bar{u})^C \tau_L^{1-C} \frac{(h-h_m)^C}{h^{2C+1}} \tag{7}$$

where

$$C = \frac{1}{1.616} \cong 0.62 \ .$$

It should be realized that in entering the converging wedge of a contact, the shear buildup in the fluid passes through stages where it is still Newtonian with $\left|\frac{\tau_S}{\tau_L}\right| < 0.6$, but for the purpose of simplifying the formulation it is assumed that the fluid is predominantly non-Newtonian in the contact entrance, with $\left|\frac{\tau_S}{\tau_L}\right| \geq 0.6$. Obviously high viscosities and high rolling speeds support this assumption. Newtonian-non-Newtonian transition in terms of the shear stress to limiting shear stress ratio is a more complex phenomena, Since at each x_1 location

$$\left|\frac{\tau(x_3)}{\tau_L(x_1)}\right| \leq \left|\frac{\tau_S(x_1)}{\tau_L(x_1)}\right|$$

with $\tau(x_3) = 0$ at $x_3 = 0$. Hence, for the sake of simplicity, equation (7) is considered to be the governing equation.

In the following section the dimensionless film thickness equation for those four different regimes are presented with a given set of physical operating conditions. The appropriate regime, hence, which film thickness equation is valid, is determined from the criteria given in Hooke [26], with the following exception. In reference [26] it is noted that for values of h' greater than 11.31 (See Figure 36, where $h' = \frac{h_{min} \ W/L}{\mu_o \bar{u} \ R}$), although there is a localized flattening of the film thickness in advance of the pressure spike, the bulk of

the contact retains its cylindrical shape and is regarded as being essentially rigid. In the present study that region with h' ≥ 11.31 is considered to be in EHD region resulting in a larger EHD area and a smaller rigid surface-variable viscosity area.

In fact, the present R-V equation being a multiple of the R-I equation, even in the new borders defined as above, is accurate away from the transition lines between the regions. The R-V region, being relatively more complicated to formulate but practically less important than the other regimes, is believed to be fairly approximated. This point will further be explored in the discussion.

Film Thickness Equations

Solution of the Governing Equation in EHD Regime with Elastically Deformed Surfaces and Pressure Dependent Viscosity (E-V)

In this lubrication regime viscosity changes with pressure as

$$\mu = \mu_o \, e^{\alpha P} \quad ,$$

and the limiting shear stress is expressed as

$$\tau_L = mP \quad ,$$

where the zero pressure value is dropped since it is relatively less important than the slope m in expressing the pressure dependency of the limiting shear stress, especially in the high pressure region of practical interest in lubricated contacts.

Solution of the governing equation, Equation (7) with these expressions is outlined in Appendix E and the resulting dimensionless film thickness is

$$\left(\frac{h_o}{R}\right) = 2.48 \, m^{0.4} \, (\alpha E_r)^{0.651} \left(\frac{\mu_o \bar{u}}{E_r R}\right)^{0.651} \left(\frac{E_r R}{w/L}\right)^{0.175} \frac{I(P)^{-1.05}}{\alpha^{.651}} \quad (8)$$

where

$$I(P) = \int_o^{P_i} \frac{e^{-0.62\alpha P}}{P^{0.38}} \quad \text{and} \quad \left[\frac{I(P)^{-1.05}}{\alpha^{.651}}\right] \cong 0.5$$

The numerical value of 0.5 for the bracketed term results from the use of an inlet pressure (P_i) of 0.68 GPa and a range of representative values of α. This numerical value is quite insensitive to the values of both α and P_i in the ranges of those variables usually associated with EHD.

Solution of the Governing Equation in the Elastically Deformed Surface Isoviscous Regime (E-I)

In this isoviscous case, $\mu = \mu_o$ and the dimensionless film thickness equation is

$$\left(\frac{h_o}{R}\right) = 1.5 \ m^{0.4} \left(\frac{E_r}{P_i}\right)^{.651} \left(\frac{\mu_o \bar{u}}{E_r \cdot R}\right)^{.651} \left(\frac{E_r \cdot R}{w/L}\right)^{.175} \tag{9}$$

since

$$I(P) = \frac{P_i^{\ 0.62}}{0.62}$$

for this case. It should be remembered that this regime is the lubrication of soft materials with relatively low elastic moduli, such that the pressures generated are low enough not to cause an increase in viscosity but do cause elastic deformation. A limiting case of maximum P_i might be in the neighborhood of $\frac{1}{\alpha}$ so that $(e^{\alpha P})$ does not contribute an order of magnitude change to the viscosity.

Solution of the Governing Equation in the Rigid Body Isoviscous Regime. R-I

In this regime pressures generated in the contact are considerably

lower, so that neither elastic deformation nor significant change in viscosity will occur. As outlined in Appendix (F) the dimensionless film thickness equation for this regime is

$$\left(\frac{h_o}{R}\right) = 1.738 \; m^{0.469} \left(\frac{\mu_o \bar{u}}{w/L}\right)^{0.765} \tag{10}$$

Solution of the Governing Equation in the Rigid Body - Variable Viscosity Regime. (R-V)

As in the Newtonian case and outlined in Appendix (G), the film thickness in this regime is expected to be a multiple of the film thickness in rigid body-isoviscous case. The inlet pressure values of interest will be larger than $\frac{1}{\alpha}$ which will cause significant changes in viscosity but are bounded to a range which will not cause significant elastic deformation. This range of inlet pressure can be of the order of 1.0 to 5.0 times $\frac{1}{\alpha}$. Therefore for a range of pressure viscosity coefficient of from 14 to 45 GPa^{-1} (1 to 3 x 10^{-4} psi^{-1}) the constant multiplier ranges from 2 to 3. Hence, for all practical purposes, this constant is taken to be 2.5 and the dimensionless film thickness equation for this case is

$$\left(\frac{h_o}{R}\right) = 2.5 \left(\frac{h_o}{R}\right)_{\text{Rigid body-isoviscous}} . \tag{11}$$

The film thickness equations presented above are plotted in Figures 38 through 43 within the ranges as shown in Tables 13 through 16. Viscosities with three different orders of magnitude and two loads with one order of magnitude difference are used. For each case rolling speed is varied within two orders of magnitude, and the limiting shear stress parameter m is assigned three different values.

The corresponding Newtonian film thickness equations for each regime are listed for comparison [29]

$$\left(\frac{h_o}{R}\right) = 4.9 \left(\frac{\mu_o \bar{u}}{w/L}\right) \qquad \text{R-I} \qquad (12a)$$

$$\left(\frac{h_o}{R}\right) = 2.3 \times \left(\frac{h_o}{R}\right)_{R-I} \qquad \text{R-V} \qquad (12b)$$

$$\left(\frac{h_o}{R}\right) = \left(\frac{1.6}{0.75}\right) (\alpha E_r)^{0.6} \left(\frac{\mu_o \bar{u}}{E_r \cdot R}\right)^{0.7} \left(\frac{E_r \cdot R}{w/L}\right)^{0.13} \qquad \text{E-V} \qquad (12c)$$

Note, for these figures the contact materials were taken to be steel on steel with E_r = 220 GPa ($\cong$ 3.3 x 10^7 psi). Therefore, elastic-isoviscous regime is not involved in the example plots.

Generalized Regime Charts

By defining g_1 and g_3 as defined in Reference [26], and by letting

$$h' = \left(\frac{w/L}{\mu_o \bar{u}}\right)^{0.765} \left(\frac{h_o}{R}\right)$$

the four different film thickness equations can be represented as

$$h' = 1.738 \, m^{0.469} \qquad \text{R-I} \qquad (13a)$$

$$h' = 2.5 * h'_{R-I} \qquad \text{R-V} \qquad (13b)$$

$$h' = 1.24 \, m^{0.4} \, g_1^{0.724} \, g_3^{-0.496} \qquad \text{E-V} \qquad (13c)$$

$$h' = 1.5 \, m^{0.4} \, C \, g_3^{0.95} \qquad \text{E-I} \qquad (13d)$$

where $C = \left(\dfrac{E_r}{P_i}\right)^{0.651}$ and $\left(\dfrac{E_r}{P_i}\right)$ is assumed to be in order of one to ten for these E-I conditions.

Note, however, that the Figures 44 and 45 are only approximate since in deriving Equation (13c) above the power of E_r and α are not satisfied by the definition of g_1 and g_3; likewise, in Equation (13d) powers of $(\mu_o \bar{u})$ and w/L are different then the ones in the original equation. Hence, the purpose of including these two charts of regimes is just to get a rough idea of which lubrication regime is to be expected under a given set of operating conditions.

Finally it should be noted that the regime charts for the present non-Newtonian model have the same characteristics as the charts based on Newtonian models [26], except that the extension of E-V region, and therefore, R-V region being confined to a smaller area. This point will further be explored in the discussion.

Discussion

The shear constitutive equation proposed by Winer and Bair [25], has an elastic term and a nonlinear viscoplastic term to describe the shear rheological response of the fluids in EHD contacts, that is

$$\dot{\gamma} = \frac{1}{G_\infty} \frac{d\tau}{dt} + \frac{\tau_L}{\mu} \tanh^{-1}\left(\frac{\tau}{\tau_L}\right)$$

High viscosity fluids, with relatively low G_∞ values are expected to have some elastic characteristics of behavior, therefore, it was first attempted to solve the full model in a conventional film thickness analysis.

The term $\dfrac{d\tau}{dt}$ can be written as $\dfrac{d\tau}{dx_1} \dfrac{dx_1}{dt}$ where $\dfrac{dx_1}{dt} \cong \bar{u}$ and since

$$\tau = \left(\frac{dP}{dx_1}\right) x_3 + F(x_1) \quad \text{from the momentum equation}$$

and therefore

$$\frac{1}{G_\infty} \frac{d\tau}{dt} \cong \frac{\bar{u}}{G_\infty} \frac{d\tau}{dx_1} = \frac{\bar{u}}{G_\infty} \left[\frac{d^2P}{dx_1^2} x_3 + \frac{dF(x_1)}{dx_1} \right]$$

Inclusion of the second derivative of pressure in the model results in extremely high pressures (and pressure gradients) in the inlet zone and therefore causes numerical problems. Although the approximation $\frac{dx_1}{dt} \cong \bar{u}$ can give some idea for comparing the relative effects of elastic and viscoplastic terms of the constitutive equation, the velocity profile is not constant across the film and this assumption may be causing the numerical problems when the whole constitutive equation is twice integrated across the film.

The apparent viscosity versus shear rate curves in Reference [27] imply a visco-plastic behavior for high viscosity fluids (although the viscous region is confined to very low shear rates), and resembles the limiting shear stress-plastic deformation characteristic of visco-plastic behavior as presented in [25], by Winer and Bair. Therefore it is assumed that the visco-plastic portion of the shear constitutive equation, Equation (1), can be used in the film thickness analysis with high viscosity lubricants.

The governing equation, Equation (6'), is approximated by a simpler function within ± 5 percent error in order to make the formulation easier. This approximation is valid for $|\frac{\tau_s}{\tau_L}| \geq 0.6$. For $|\frac{\tau_s}{\tau_L}| < 0.6$ behavior is purely viscous and the governing equation is the well-known Reynold's equation. This fact is also seen from the shear constitutive equation because for the argument $|\frac{\tau}{\tau_L}|$ less than approximately 0.6, $\tanh^{-1} |\frac{\tau}{\tau_L}|$ is approximately equal to $|\frac{\tau}{\tau_L}|$ and the constitutive equation is simply Newton's law of viscosity. The non-Newtonian characteristic of the proposed shear constitutive model will be dominant for $|\frac{\tau}{\tau_L}| \geq 0.6$. It should also be noticed that both the velocity distribution, Equation (4), and the governing equation, Equation (6), can be reduced to their Newtonian counterparts by taking the limit τ_L approaching infinity. As explained above for this characteristic, $|\frac{\tau}{\tau_L}| < 0.6$ is sufficient.

After deriving the governing equation by following the conventional

procedure of continuum mechanics, this equation is solved for the film thickness for several cases. These are, as outlined in the introduction, the four different regimes of lubrication. The importance of discriminating between these regimes is seen by noting that the difference between Martin's solution and Dowson and Higginson's solution will be more than 50 percent, for the data of Figure 42. This difference, however, will decrease as the regime shifts from R-I to R-V and subsequently approaching E-V region.

Early studies of R-V regime indicated that the film thickness in this regime can be expressed as a multiple of the film thickness of R-I regime, and the multiplication factor is a function of the pressure coefficient of viscosity [30]. However, in Reference [30] it is pointed out that the limit of this factor is approximately 2.3. Beyond this limit, the solution for this region is referenced to some extrapolations of Blok's results [31]. However, in Greenwood's paper [31], it is shown that the extrapolation will not deviate much from the Grubin's E-V film thickness equation. Also in Reference [26] it is noted that for the cases which result in factors larger than 2.3 there is a localized flattening of the film in advance of the pressure spike. These all imply the possibility of extending the E-V region, and confining the R-V region to a smaller extent, as presented in this analysis. Hence, for the non-Newtonian R-V region, which is believed to be of relatively less practical importance and more difficult to formulate, the film thickness is assumed to be 2.5 times the film thickness of R-I region.

The film thickness equation for E-I region is not used in the numerical examples presented because the contact materials are considered to be made of steel and therefore, the pressure generated in the film cannot be high enough to deform steel and yet low enough not to cause significant change in viscosity. In drawing Figures 44 and 45, the value for E_r/P_i is assumed to be in the order of 1 to 10 because of the low modulus materials involved. The border lines of the regimes are only weakly dependent on (E_r/P_i) of E-I case. As explained in the introduction the limiting shear stress parameters tend to decrease with increasing viscosity. Although this characteristic is generally accepted the present analysis suffers from the lack of experimental data for the slope m values in the high viscosity ranges used. In a previous study [28], for the viscosities in the order of 10^{-1} to 10^{-2} Pas [10^{-5} or 10^{-6} lbs/in^2], the experimentally measured slopes of 0.1 or 0.05 have been used and it has been observed that the zero pressure value of τ_L is relatively less important than the slope m. In the present study with viscosities ranging from 1 Pas [10^{-4} lbs/in^2]

to 10^2 Pas [10^{-2} lbs/in^2], slopes ranging from 0.01 to 0.001 are thought to be reasonable. In [32] capillary viscosity measurements indicate that dimethylsiloxane (10^2 Pas at 27C) has a limiting shear stress of 4 MPa at 550 MPa confirming that the slope is in the order of 10^{-3}. This measurement was at low temperature and increasing the temperature is expected to result in further decrement of the limiting shear stress. Finally, it should once again be remembered that the order of the slope m is very important in predicting the film thickness since the dimensionless film thickness is directly related to viscosity and m, the effect of increase of the former can only be compensated, other parameters remaining the same, by a decrease in the latter. Hence, substantially lower film thickness measurements with high viscosities imply the necessity of assigning low limiting shear stress parameters in such analytical studies.

Conclusions

In a recent paper Gecim and Winer analyzed the effect of lubricant limiting shear stress on film thickness, based on a non-Newtonian rheological model [28]. In that study the viscosity range was fairly low so that, the deviation (≈ 40 percent) from the Grubin's conventional theory is attributed to high sliding and, to some extent, low limiting shear stress parameters (which have been measured and reported in [2]). No drastic deviation from Newtonian solution, or a sudden collapse is expected for that case, as concluded in [28]. However, as the experimental studies indicated, EHD contacts failed to form a lubricant film with high viscosity lubricants and the results of the present analysis imply this analytically. Since the theoretical film thickness equation of the present analysis is directly related to the viscosity, it is concluded that, for this pure rolling case, these deviations from the Newtonian theory are due to their low limiting shear stresses.

For each viscosity case, with low loads where the regime falls into R-I region, greater deviation is predicted than with high loads where the regime will be in E-V region. It should be recalled that the R-I region implies low contact pressures, hence, low limiting shear stresses. Increase of rolling speed for each curve results in an increase in the deviation of non-Newtonian lines from the corresponding Newtonian line.

Thermal effects, which might be considerable with high viscosities, indicate the need of inclusion of the energy equation in the nonlinear formulations of the present analysis. The authors do not address that question in the work.

Although the present isothermal analysis is not able to match
the experimental data of Reference [27] with the m values used,
it should be noted as it is reported in Reference [27] that the
test fluids with these viscosities were too viscous to circu-
late into the contact and, some fracture was observed at high
rolling speeds. This tends to confirm the inability of these
high viscosity fluids to form a satisfactory lubricant film, due
to their low limiting shear stresses which might be reached even
far out in the inlet zone.

Finally, it is concluded that, with steel on steel line contacts
the lubrication with high viscosity fluids falls into R-I regime
under the loads of the order of 10^4 N/m [10^2 lb/in], and into E-V
region if the loading is in the order of 10^5 N/m [10^3 lb/in] or
higher for the rolling speeds of practical interest. The inter-
mediate R-V regime is confined to a smaller region and thought
as being less important.

The present study supports the observation of film thicknesses
which are smaller than predicted by traditional lubrication analysis
for high viscosity fluids and implies the need for

      i)   including the energy equation in the nonlinear
            formulations, and

     ii)   measurements of limiting shear stress parameters
            for high viscosity fluids.

REFERENCES

1. Winer, W. O., and Bair, S., "Surface Temperatures and Glassy State Investigations in Tribology", NASA CR-3031 (July 1979).

2. Bair, S., and Winer, W. O., "Shear Strength Measurements of Lubricants at High Pressure", *Trans. ASME, Journal of Lubrication Technology 101, 3* (July 1979) 251-257.

3. Johnson, K. L., and Tevaarwerk, J. L., "Shear Behaviour of Elastohydrodynamic Oil Films", *Proc. Roy. Soc. of London, 365A,* (1977) 215-236.

4. Koye, K. A., "Experimental Evaluation of the Hamrock and Dowson Elastohydrodynamic Point Contact Theory", M.S. Thesis, Georgia Institute of Technology (November 1979).

5. Hamrock, B. J., and Dowson, D., "Isothermal Elastohydrodynamic Lubrication of Point Contacts: Part 1 - Theoretical Formulation", *Trans. ASME Journal of Lubrication Technology 98* (April 1976) 223.

6. Hamrock, B. J., and Dowson, D., "Isothermal Elastohydrodynamic Lubrication of Point Contacts: Part 2 - Ellipticity Parameter Results", *Trans. ASME, Journal of Lubrication Technology 98* (July 1976) 375.

7. Hamrock, B. J., and Dowson, D., "Isothermal Elastohydrodynamic Lubrication of Point Contacts: Part 3 - Fully Flooded Results", *Trans. ASME, Journal of Lubrication Technology 99* (April 1977) 264.

8. Hamrock, B. J., and Dowson, D., "Isothermal Elastohydrodynamic Lubrication of Point Contacts: Part 4 - Starvation Results", *Trans. ASME, Journal of Lubrication Technology 99* (1977) 15.

9. Brewe, D., and Hamrock, B. J., "Simplified Solution for Elliptical-Contact Deformation Between Two Elastic Solids", *Trans. ASME 99,* Series F, No. 4 (1977) 485-487.

10. Foord, C. A., Wedeven, L. D., Westlake, F. J., and Cameron, A., "Optical Elastohydrodynamics", *Proc. Inst. Mech. Eng., 184,* Part 1, London (1969-1970).

11. Nagaraj, H. S., "Investigation of Some Temperature-related Phenomena in Elastohydrodynamic Contacts including Surface Roughness Effects", Ph.D. Thesis, Georgia Institute of Technology (December 1976).

50

12. Archard, J. F., and Cowking, F. W., "Elastohydrodynamic Lubrication at Point Contacts", *Proc. Inst. Mech. Eng.* (1965-1966) 180.

13. Bahadoran, H., and Gohar, R., "The Oil Film in Elasto-hydrodynamic Elliptical Contacts", *Wear 29* (1974) 264-270.

14. Gledhill, R. H., Jackson, A., Cameron, A., "An Interfero-metric Study of the EHL of Elliptical Contacts Aligned in the Direction of Rolling", *Proc.of the 5th Leeds-Lyon Symposium*, (September 1978) Editors: D. Dowson, C. M. Taylor, M. Godet.

15. Hamrock, B. J., and Dowson, D., "Minimum Film Thickness in Elliptical Contacts for Different Regimes of Fluid-Film Lubrication", NASA Technical Paper No. 1342 (October 1978).

16. Dixon, W. J., and Brown, M. B. (Editors) "BMDP Biomedical Computer Programs P-Series, 1979", Health Science Computing Facility, Department of Bio-Mathematics University of California, Los Angeles, California, University of California Press.

17. Archard, J. F., "Experimental Studies of Elastohydrodynamic Lubrication", *Proc. Inst. Mech. Eng, 180,* Part 3-B, 17-30.

18. Blok, H., "The Postulate about the Constancy of Scoring Temperature", *NASA Symposium on Interdisciplinary Approach to the Lubrication of Concentrated Contacts, I* (July 1969).

19. Nagaraj, H. S., Sanborn, D. M., and Winer, W. O., "Direct Surface Temperature Measurement by Infrared Radiation in Elastohydrodynamic Contacts and the Correlation with the Blok Flash Temperature Theory", *Wear 49* (1978) (Note several figures and captions were incorrectly paired in the original. An errata appears in *Wear 51* (1978) 400).

20. Ausherman, V. K., Nagaraj, H. S., Sanborn, D. M., and Winer, W. O., "Infrared Temperature Mapping in Elastohydrodynamic Lubrication", *Trans. ASME, Journal of Lubrication Technology 98* (1976) 236-243.

21. Nagaraj, H. S., Sanborn, D. M., and Winer, W. O., "Surface Temperature Measurements in Rolling and Sliding EHD Contacts", *Trans. ASLE, 22* (1979) 277-285.

22. Kool, E. H., "Thermal Effects in Traction Drive Elements", Masters Thesis, School of Mechanical Engineering, Georgia Institute of Technology (1979).

23. Lauer, J., Correspondence with Dr. J. Lauer at Rensselaer Polytechnic Institute.

24. Hijuchi, S., Tanaka, S., and H. Kamada, *Spectrochimica Acta 28A* 1972) 1721-1730.

25. Bair, S., and Winer, W. O., "A Rheological Model for EHD Contacts Based on Primary Laboratory Data", *ASME Journal of Lubrication Technology 101* (July 1979) 258.

26. Hooke, C. J., "The Elastohydrodynamic Lubrication of Heavily Loaded Contacts", *Journal of Mechanical Engineering Science, IMechE 1977, 19,* No. 4 (1977).

27. Dyson, A., and Wilson, A. R., "Film Thickness in Elastohydrodynamic Lubrication by Silicone Fluids", *Proc. Inst. Mech. Eng., 180,* Part 3K (1965-1966).

28. Gecim, B., and Winer, W. O., "Lubricant Limiting Shear Stress Effect on EHD Film Thickness", *Trans. ASME, Journal of Lubrication Technology, 102,* No. 2 (April 1980) 213-221.

29. Dowson, D., and Higginson, G. R., "Elastohydrodynamic Lubrication SI Edition", *International Series in Materials Science and Technology, 23,* Pergamon International Library, Pergamon Press.

30. Blok, H., "Discussion of Paper by E. McEwen", *Journal of Institute Petroleum 38* (1952) 673.

31. Greenwood, J. A., "Presentation of Elastohydrodynamic Film Thickness Results", *Journal of Mechanical Engineering Science 11(2)* (1969) 128.

32. Jakobsen, J., and Winer, W. O., "High Shear Stress Behavior of Some Representative Lubricants", *Trans. ASME, Journal of Lubrication Technology 97* (1975) 479-485.

Appendix A
Experimental Fluids
(Section II)

SYMBOL: R620-15 (See also Appendix D)

SOURCE: Sun Oil Company

TYPE: Naphthenic Base Oil

PROPERTIES: Kinematic Viscosity at 37.8C m^2/s

                  24×10^{-6}

                  Kinematic Viscosity at 98.9C m^2/s

                  3.7×10^{-6}

                  Density at 20C kg/m^3

                  0.916×10^3

                  Average Molecular Weight - 305

SYMBOL: R620-16 (See also Appendix B)

SOURCE: Sun Oil Company

TYPE: Naphthenic Base Oil

PROPERTIES: Kinematic Viscosity at 37.8C m^2/s

                  114×10^{-6}

                  Kinematic Viscosity at 98.9C m^2/s

                  8.1×10^{-6}

                  Density at 20C kg/m^3

                  0.930×10^3

                  Average Molecular Weight - 357

SYMBOL: PL4520, PL4521, PL4523

SOURCE: Rohm and Haas Company

TYPE: Polyalkylmethacrylate
                 (Polymer additive used in solution in R620-15,
                 49% polymer by weight)

                 The chemical composition of each is the same. They
                 differ only in molecular weight and are supplied in
                 a carrier oil similar to R620-15

PROPERTIES:	PL4520	PL4521	PL4523
POLYMER WT.:	42.6 %	36.1%	19.0%
VISCOSITY AVERAGE MOLECULAR WEIGHT	355,000	560,000	2,000,000

Appendix B
Properties of Steel Rollers and Sapphire Disk
(Section III)

A-2 TOOL STEEL ROLLERS

MODULUS OF ELASTICITY $E = 207$ GPa (30×10^6 psi)

POISSON'S RATIO $\nu = 0.3$

HARDNESS OF ROLLER - 59 ROCKWELL C 40 MIN @ 1000C (1830 F)

SURFACE ROUGHNESS $\sigma_r = 0.13$ μm AA

SYNTHETIC SAPPHIRE Al_2O_3 DISK

MODULUS OF ELASTICITY $E = 365$ GPa (53×10^6 psi)

POISSON'S RATIO $\nu = 0.25$

HARDNESS Moh 9, Knoop microindenter 2000

($\simeq$ 63 Rockwell C)

TENSILE STRENGTH 0.40 GPa (58×10^3 psi)

COMPRESSIVE STRENGTH 20.7 GPa (30×10^5 psi)

REFRACTIVE INDEX $\eta = 1.76$

SURFACE ROUGHNESS $\sigma_s = 0.00635$ μm AA

SAPPHIRE DISK - STEEL ROLLER COMBINATION

EFFECTIVE MODULUS OF ELASTICITY

$E' = 286$ GPa (41.4×10^6 psi)

WHERE

$$E' = 2 \left[\frac{1 - \nu_{STEEL}^2}{E_{STEEL}} + \frac{1 - \nu_{SAPPHIRE}^2}{E_{SAPPHIRE}} \right]^{-1}$$

COMPOSITE SURFACE ROUGHNESS $\sigma = \sqrt{\sigma_r^2 + \sigma_s^2} = 0.13$ μm

<u>Properties of the Lubricant</u>
<u>(Section III)</u>

NAME: SUNOCO NAPHTHENIC OIL-2

CODE: R-620-16

AVERAGE MOLECULAR WEIGHT: 357

REFRACTIVE INDEX   1.5173

DENSITY @ 20°C   930.3 Kg/m^3

                           0.0336 $1bm/in^3$

VISCOSITY INFORMATION

TEMPERATURE   VISCOSITY

°C	F	mPas	REYN (x 10^6)
24.0	75.0	316	45.9
27.2	80.9	246	35.7
40.0	104.0	93	13.5
98.9	210.0	7.4	1.1

PRESSURE VISCOSITY COEFFICIENT

TEMPERATURE   α

°C	GPa^{-1}	Psi^{-1} (x 10^4)
24	36.7	2.51
27	35.7	2.459
40	31.9	2.178
99	19.8	1.365

TEMPERATURE VISCOSITY COEFFICIENT

$20 < T (°C) < 40$ $\delta = 0.047 \ F^{-1} = 0.086 \ C^{-1}$

Appendix C

Comparison of Several Commercial IR Detectors
(Section IV)

The simplest IR microscopic detector is the single spot detector.
This type, which is used in previous work cf. [19,20,21], has no
automatic scanning option. The integrated radiation coming from
a spot, 0.001 inch in diameter, is measured. Since the contact
diameter and region of interest is much larger, an automatic scan-
ning device is required.

In order to compare the different available devices, some labora-
tory tests were performed while the instruments were on loan.
The basic test was to find the temperature distribution on the
ball-side of a sapphire-steel EHD contact. Necessary data to make
a comparison is given in Table 12 . Some devices have the option
of scanning one line in the field of view separately. The renewal
of this line is usually faster than the renewal of the whole view.
In case of rapid transient effects, this could be a very useful
option.

By analyzing the different features of the detectors, the follow-
ing criteria could be set to obtain the desirable temperature
information from a EHD contact.

   a. From the geometrical point of view, a spacial resolution
       of less than 1/1000 inch and a focusing distance of more
       than 1 inch are needed.

   b. The temperature resolution for a gray body ($\varepsilon = 0.2$)
       should be better than 1°C ($\rightarrow$ Black body resolution
       better than 2°C).

   c. For transient measurement a rapid scanning feature
       would be needed.

   d. For storage reasons a digital output is preferable to
       a picture; combination of both would provide a good
       information.

These criteria could not be fulfilled by any available detector.
Comparing the data information, the UTI - 900 unit comes closest
to the requirements.

<u>Appendix D</u>
<u>Lubricants Employed - EHD Simulator</u>
(Section IV)

SYMBOL: N1

SOURCE: Sun Oil Company

TYPE: Naphthenic base oil R-620-15A

PROPERTIES: Viscosity at 37.8C m^2/sec

$24.1 * 10^{-6}$

Viscosity at 98.9C m^2/sec

$3.73 * 10^{-6}$

Density at 20C kg/m^3 915.7

Pressure Viscosity Coefficient at 25C GPa^{-1} 26

Pressure Viscosity Coefficient at 40C GPa^{-1} 22.5

Pressure Viscosity Coefficient at 100C GPa^{-1} 15

SYMBOL: Santotrac 50

SOURCE: Monsanto Company

TYPE: Synthetic Cycloaliphatic Hydrocarbon Traction Fluid

PROPERTIES: Viscosity at 37.8C m^2/sec

$34 * 10^{-6}$

Viscosity at 98.9C m^2/sec

$5.6 * 10^{-6}$

Density at 37.8C kg/m^2 889

Pressure Viscosity Coefficient at 20C GPa^{-1} 39

Pressure Viscosity Coefficient at 40C GPa^{-1} 26

Pressure Viscosity Coefficient at 70C GPa^{-1} 16.7

Pressure Viscosity Coefficient at 100C GPa^{-1} 12.8

Appendix E

Derivation of the Dimensionless Film Thickness Equation in Elastically Deformed Surfaces, Variable Viscosity Regime (i.e. EHD)
(Section V)

The governing non-Newtonian pressure gradient equation, Equation (7) was

$$\frac{dP}{dx} = 4.88 \ (\mu \ \bar{u})^C \ \tau_L^{1-C} \ \frac{(h-h_m)^C}{h^{2c+1}} \quad \text{where} \quad c \cong \frac{1}{1.616} = 0.62 \quad (A.1)$$

Defining μ, and τ_L as functions of pressure, $\mu = \mu_o e^{\alpha P}$ and $\tau_L = mP$ and assuming that pressure is zero at a large distance from the inlet point, Equation (A.1) can be integrated

$$\int_0^{p_i} \frac{e^{-c\alpha P} \ dP}{(mP)^{1-c}} = 4.88 \ (\mu_o \ \bar{u})^C \int_{-\infty}^0 \frac{(h-h_o)^C}{h^{2c+1}} \ dx \quad (A.2)$$

where $h_m = h_o$ the nominal gap of the EHD region. The elastically deformed inlet zone film shape

$$h = h_o + \frac{a^2}{2R} \left\{ \left[\frac{x}{a} \left[\left(\frac{x}{a}\right)^2 - 1 \right]^{1/2} - \ln \left[\left| \frac{x}{a} \right| + \left[\left(\frac{x}{a}\right)^2 - 1 \right]^{1/2} \right] \right\}$$

can be approximated by the expression

$$h = h_o + \frac{a^2}{2R} \left(4 \ \frac{\sqrt{2}}{3} \right) |\Sigma|^{3/2} \quad \text{where} \quad \Sigma = \left| \frac{x}{a} \right| - 1 \ \text{for} \ |\Sigma| \ll 1 \ . \quad (A.3)$$

as in Reference [27].

If we let the LHS of Equation (A.2) to be $I(p_i)$, then Equation (A.2) will take the form

$$I(P_i) = 4.88 \, (\mu_o \, \bar{u})^C \, a \int_{-\infty}^{0} \frac{\left(\frac{a^2}{R} \frac{2^{3/2}}{3}\right)^C |\Sigma|^{3c/2}}{\left[h_o + \frac{a^2 \cdot 2^{3/2}}{3 \cdot R} |\Sigma|^{3/2}\right]^{2c+1}} \, d\Sigma$$

If we change variable of integration on the RHS by letting

$$\frac{a^2}{Rh_o} \frac{2^{3/2}}{3} |\Sigma|^{3/2} = \tan^2\theta$$

then

$$I(P_i) = 4.88(\mu_o \, \bar{u})^C \, a \, \frac{h_o^C}{h_o^{2c+1}} \, K \int \frac{\tan^{2c}\theta[1 + \tan^2\theta]\tan\theta}{[\tan^2\theta + 1]^{2c+1} \tan^{2/3}\theta} \, d\theta$$

where

$$K = \frac{4}{3} \left(\frac{Rh_o}{a^2} \frac{3}{2^{3/2}}\right)^{2/3}$$

The integral on the RHS is simply

$$\int \frac{\tan^{2c + 1/3}\theta}{(\tan^2\theta + 1)^{2c}} \quad \text{or} \quad \int \sin\theta^{2c + 1/3} \cos\theta^{2c - 1/3} \, d\theta$$

Therefore the governing equation will be

$$I(P_i) = 4.88(\mu_o\bar{u})^C \, a \, \frac{h_o^C}{h_o^{2c+1}} \frac{4}{3} \left(\frac{Rh_o}{a^2} \frac{3}{2^{3/2}}\right)^{2/3} \int_0^{\pi/2} \sin\theta^{2c+1/3}\cos\theta^{2c-1/3} d\theta$$

since

$$a \approx 2 \left[\frac{2}{\pi} \cdot \frac{W/L \cdot R}{E_r} \right]^{1/2}$$

$$I(P_i) = 4.88 (\mu_o \bar{u})^C \frac{h_o^C}{h_o^{2C+1}} \frac{4}{3} \frac{1}{2^{1/3}} \left(\frac{\pi}{2} \right)^{1/6} \left(\frac{E_r}{W/L \cdot R} \right)^{1/6} R^{2/3} h_o^{2/3} \left(\frac{3}{2^{3/2}} \right)^{2/3} I(\theta)$$

where the integral at the RHS, $I(\theta)$, is ≈ 0.41 for $c = 0.62$.
Therefore

$$I(P_i) = \left(4.88 \frac{4}{3} \cdot \frac{1}{2^{1/3}} \left(\frac{\pi}{2} \right)^{1/6} \left(\frac{3}{2^{3/2}} \right)^{2/3} 0.41 \right) (\mu_o \bar{u})^C \frac{R^{2/3}}{h_o^{C+1/3}} \left(\frac{E_r}{W/L \cdot R} \right)^{1/6}$$

or

$$I(P_i) = 2.374 \left(\frac{\mu_o \bar{u}}{R} \right)^C \frac{R^C \cdot R^{2/3}}{h_o^{C+1/3} \cdot R^{1/3}} \left(\frac{E_r \cdot R}{W/L} \right)^{1/6}$$

Therefore, finally

$$\left(\frac{h_o}{R} \right)^{C+1/3} = 2.374 \left(\frac{\mu_o \bar{u}}{R} \right)^C \left(\frac{E_r \cdot R}{W/L} \right)^{1/6} \frac{1}{I(P_i)}$$

recall that c = 0.62.

Therefore

$$\left(\frac{h_o}{R}\right) = 2.48 \left(\frac{\mu_o \bar{u}}{R}\right)^{.651} \left(\frac{E_r \cdot R}{W/L}\right)^{.175} \frac{1}{I(P_i)^{1.05}}$$

or

$$\left(\frac{h_o}{R}\right) = 2.48 \; (\alpha \; E_r)^{.651} \left(\frac{\mu_o \bar{u}}{E_r \cdot R}\right)^{.651} \left(\frac{E_r \cdot R}{W/L}\right)^{.175} \frac{I(P_i)^{-1.05}}{\alpha^{.651}} \tag{A.4}$$

where

$$I(P_i) = \int_o^{P_i} \frac{e^{-\alpha c P} \, dP}{(mP)^{1-c}}$$

Equation (A.4) is the dimensionless film thickness equation based on the non-Newtonian constitutive equation.

Appendix F
Derivation of the Dimensionless Film Thickness
Equation in Rigid Body Isoviscous Regime
(Section V)

The governing equation, Equation (7) with $\mu = \mu_0$ will take the form

$$\frac{dP}{dx} = 4.88 \; \mu_0^c \; \bar{u}^c \; \tau_L^{1-c} \; \frac{h_0^c}{h_0^{2c+1}} \; \frac{\left[\dfrac{x^2}{2Rh_0} - \dfrac{x_m^2}{2Rh_0} \right]^c}{\left[1 + \dfrac{x^2}{2Rh_0} \right]^{2c+1}} \tag{A.5a}$$

where $h = h_0 + \dfrac{x^2}{2R}$, hence $h_m = h_0 + \dfrac{x_m^2}{2R}$. If we let $\tan\theta = \dfrac{x}{\sqrt{2Rh_0}}$,

and $\dfrac{dx}{d\theta} = \dfrac{1}{\cos^2\theta} \sqrt{2Rh_0}$

$$\int \frac{dP}{p^{0.38}} = 4.88 \; \mu_0^c \; \bar{u}^c \; m^{0.38} \; \frac{h_0^c}{h_0^{2c+1}} \; \sqrt{2Rh_0} \int \left[\cos^2\theta - \frac{\cos^4\theta}{\cos^2\theta_m} \right]^c d\theta \tag{A.5b}$$

where

$$\tan^2\theta_m = \frac{x_m^2}{2Rh_0}$$

since $P = 0$ at $\theta = -\dfrac{\pi}{2}$ (i.e., $x = -\infty$)

and $\quad P = 0$ at $\theta = \theta_m$ (Reynold's B.C)

the value of θ_m is found by trial and error until

$$\int_{-\pi/2}^{\theta_m} \left[\cos^2\theta - \frac{\cos^4\theta}{\cos^2\theta_m} \right]^c d\theta = 0$$

This value is

$$\theta_m = 0.4525$$

then

$$P = \left[3.03\ m^{0.38}\ \mu_0{}^c\ \bar{u}^c\ \frac{h_o{}^c}{h_o{}^{2c+1}}\ \sqrt{2Rh_o}\ \int_{-\pi/2}^{\theta} \left[\cos^2\theta - \frac{\cos^4\theta}{\cos^2\theta_m}\right]^c d\theta \right]^{1/0.62}$$

Since

$$W/L = \sqrt{2Rh_o}\ \int_{-\pi/2}^{\theta_m} P\ \frac{d\theta}{\cos^2\theta}\ , \text{ and recall that } c = 0.62,$$

then

$$W/L = \sqrt{2Rh_o}\ m^{0.613}\ \mu_0\ \bar{u}\ \frac{h_o}{h_o{}^{1/c+2}}\ \left(\sqrt{2Rh_o}\right)^{1/c}$$

$$\times \int_{-\pi/2}^{\theta_m} \left[\int_{-\pi/2}^{\theta} \left[\cos^2\theta - \frac{\cos^4\theta}{\cos^2\theta_m}\right]^c\right]^{1/c}$$

The value of the integral at the RHS is found to be 0.142 with 1000 grid points of numerical integration between $\theta = -\pi/2$ and $\theta = \theta_m = 0.4525$. Then, finally, the dimensionless film thickness equation for this case is

$$\left(\frac{h_o}{R}\right) = 1.738\ m^{0.469} \left(\frac{\mu_0\ \bar{u}}{W/L}\right)^{0.765} \tag{A.6}$$

Appendix G
Derivation of the Dimensionless Film Thickness
Equation in Rigid Body - Variable Viscosity Regime
(Section V)

In this case, the RHS of the Equation (A.5b) is the same but the LHS pressure integral has the form

$$\int_{o}^{P} \frac{e^{-\alpha cP}}{P^{1-c}} \, dP$$

Writing the exponential term in Taylor series expansion and integrating results in

$$\int_{o}^{P} \frac{e^{-\alpha cP}}{P^{1-c}} \, dP = P^{c} \sum_{o}^{\infty} \frac{(-\alpha cP)^{n}}{(n+c)n!}$$

which can be approximated by the form, within $|5|$ percent error, $[AP^{0.62}]$, which will lead to a similar solution as in R-I case, where the values of A changes with the pressure range in each α case, and with α itself. But, as stated in the text, for all practical purposes, the variation of the coefficient in front of the rigid body-isoviscous solution, between ≈ 2.0 to ≈ 3.0, is handled by assuming it to be 2.5.

Hence, the dimensionless film thickness equation for this case is

$$\left(\frac{h_{o}}{R}\right) = 2.5 \left(\frac{h_{o}}{R}\right)_{\text{Rigid body-isoviscous}} \tag{A.7}$$

Table 1. Pressure Viscosity Coefficients[+]

Material	Temperature/C	α_o/GPa^{-1}	α^*/GPa^{-1}
R620-15	26	27.4	27.7
	99	15.4	14.8
	227	12.0	8.85
R620-15 + PL4523	26	25.5	25.7
	99	17.1	15.0
	227	16.8	10.3
R620-15 + PL4521	26	24.2	24.9
	99	15.0	15.3
	227	13.8	9.8
R620-16	26	35.6	35.8
	99	19.8	19.8
	227	10.8	10.6

where

$$\alpha^* = \left[\int_{p\,=\,0}^{p\to\infty} \frac{\mu_o}{\mu}\ dP \right]^{-1} \quad \text{at constant temperature}$$

$$\alpha_o = \left. \frac{\partial \ell n\mu}{\partial p} \right|_{T\,=\,\text{const.}}$$

[+]from falling body viscometer data.

Table 2.   Geometry of the Crowned Rollers

k	r_x		r_y		R_y/R_x
	in	cm	in	cm	
3.70	0.616	1.56	4.57	11.62	7.42
2.40	0.624	1.58	2.35	5.97	3.77
0.958	0.609	1.55	0.60	1.51	0.99
0.651	0.615	1.55	0.33	0.84	0.54
0.360	0.615	1.56	0.13	0.33	0.21
0.305	0.615	1.56	0.10	0.25	0.16
0.117	0.609	1.55	0.022	0.056	0.036

Table 3. Dimensionless Speed, Load and Corresponding Measured
Minimum Film Thickness Results for $k = 3.7$, $R_y/R_x = 7.42$

$U(x\ 10^{10})$	$W(x\ 10^5)$	$H_{min.exp}(x\ 10^6)$	$\lvert H_{min.exp} - H_{min}\rvert$	$(H_{min.exp}/H_{min})$
0.353	0.16136	68.5	4.29	1.067*
0.633	0.16136	111.2	15.55	1.163
0.880	0.16136	120.9	1.30*	1.011
0.353	0.53153	70.6	11.76	1.200
0.633	0.53153	103.7	16.06	1.183
0.880	0.53153	131.7	21.98*	1.200

*Each asterisk denotes one standard deviation from the mean.

Table 4. Dimensionless Speed, Load and Corresponding Measured
Minimum Film Thickness Results for $k = 2.4$, $R_y/R_x = 3.77$

$U(\times 10^{10})$	$W(\times 10^6)$	$H_{min.exp}(\times 10^6)$	$\lvert H_{min.exp} - H_{min}\rvert$	$(H_{min.exp}/H_{min})$
0.348	0.968	64.4	6.57	1.114
0.625	0.968	95.0	8.85	1.100
0.869	0.968	104.6	3.15*	0.971*
0.348	3.2621	60.3	2.51	1.140
0.625	3.2621	102.4	23.5*	1.298
0.869	3.2621	108.7	10.0	1.101

*Each asterisk denotes one standard deviation from the mean.

Table 5. Dimensionless Speed, Load and Corresponding Measured
Minimum Film Thickness Results for k = 0.958, R_y/R_x = 0.99

$U(\times 10^{10})$	$W(\times 10^6)$	$H_{min.exp}(\times 10^6)$	$\|H_{min.exp} - H_{min}\|$	$(H_{min.exp}/H_{min})$
0.357	0.343	57.3	19.57*	1.519*
0.641	0.343	81.1	24.90**	1.443
0.890	0.343	93.1	22.79*	1.324
0.357	1.0164	49.8	14.89	1.427
0.641	1.0164	74.7	22.78*	1.438
0.890	1.0164	87.7	22.73*	1.350
0.357	3.4248	38.9	2.09	1.220
0.641	3.4248	62.7	15.20	1.320
0.890	3.4248	81.1	21.670*	1.360

*Each asterisk denotes one standard deviation from the mean.

Table 6. Dimensionless Speed, Load and Corresponding Measured
Minimum Film Thickness Results for $k = 0.651$, $R_y/R_x = 0.54$

$U(x\ 10^{10})$	$W(x\ 10^6)$	$H_{min.exp}(x\ 10^6)$	$|H_{min.exp} - H_{min}|$	$(H_{min.exp}/H_{min})$
0.353	0.15236	40.7	10.93	1.37
0.634	0.15236	59.0	14.76	1.33
0.882	0.15236	66.5	11.13	1.20
0.353	0.48882	38.5	11.24	1.41
0.634	0.48882	56.7	16.09	1.40
0.882	0.48882	64.2	13.37	1.26
0.353	1.5934	26.8	1.79*	1.07*
0.634	1.5934	45.0	2.87	1.21
0.882	1.5934	55.8	9.12	1.20

*Each asterisk denotes one standard deviation from the mean.

Table 7. Dimensionless Speed, Load and Corresponding Measured Minimum Film Thickness Results for $k = 0.360$, $R_y/R_x = 0.21$

$U(x\ 10^{10})$	$W(x\ 10^{7})$	$H_{min.exp}(x\ 10^{6})$	$|H_{min.exp} - H_{min}|$	$(H_{min.exp}/H_{min})$
0.353	0.63483	26.8	2.72	1.40
0.634	0.63483	38.5	9.89	1.35
0.881	0.63483	45.0	9.20	1.26
0.353	3.1107	26.8	9.71	1.57*
0.634	3.1107	39.7	14.17	1.56*
0.881	3.1107	46.0	14.11	1.44
0.353	7.4276	20.3	4.26	1.26
0.634	7.4276	30.1	6.14	1.26
0.881	7.4276	38.5	8.60	1.29

*Each asterisk denotes one standard deviation from the mean.

Table 8. Dimensionless Speed, Load and Corresponding Measured
Minimum Film Thickness Results for k = 0.305, R_y/R_x = 0.16

$U(\times 10^{10})$	$W(\times 10^7)$	$H_{min.exp}(\times 10^6)$	$\lvert H_{min.exp} - H_{min} \rvert$	$(H_{min.exp}/H_{min})$
0.353	0.38090	23.6	6.38	1.37
0.634	0.38090	36.4	10.80	1.42
0.881	0.38090	40.7	8.60	1.27
0.353	1.2062	23.6	7.76	1.49
0.634	1.2062	34.3	10.75	1.46
0.881	1.2062	45.0	15.58	1.53*
0.353	3.7455	18.2	3.65*	1.25
0.634	3.7455	27.8	6.12	1.28
0.881	3.7455	36.4	9.30	1.34

*Each asterisk denotes one standard deviation from the mean.

Table 9. Dimensionless Speed, Load and Corresponding Measured
Minimum Film Thickness Results for k = 0.117, R_y/R_x = 0.036

$U(\times 10^{10})$	$W(\times 10^7)$	$H_{min.exp}(\times 10^6)$	$\|H_{min.exp} - H_{min}\|$	$(H_{min.exp}/H_{min})$
0.214	0.64740	2.0	0.61*	1.13
0.357	0.64740	9.7	2.88*	1.42
0.641	0.64740	23.8	13.66	2.35***
0.214	0.97111	5.4	0.75*	1.16
0.357	0.97111	10.8	4.23*	1.64*
0.641	0.97111	13.0	3.12*	1.32
0.214	1.5538	3.3	1.22*	0.728**
0.357	1.5538	10.8	4.45	1.70*
0.641	1.5538	12.0	2.47*	1.26

*Each asterisk denotes one standard deviation from the mean.

Table 10. Film Thickness Statistics

	Mean		Standard Deviation	
$\ln(H_{min.exp})$	- 10.06095		0.82934	
$h_{min.exp}$	26.27	$\mu in.$		
	0.667	μm		
$\|h_{min} - h_{min.exp}\|^{(1)}$	6.682	$\mu in.$	4.069	$\mu in.$
	0.170	μm	0.103	μm
$(h_{min.exp}/h_{min.})^{(1)}$	1.302		0.214	
$(h_{min.exp}/h_{min.})^{(2)}$	1.0095		0.1398	

(1) h_{min} calculated by Hamrock and Dowson Model Equation (1)

(2) h_{min} calculated by regression model Equation (6)

Table 11. Film Thickness Statistics as a Function of Ellipticity Ratio (k)

| k | $\dfrac{h_{min.exp.}}{h_{min.}}$ [1] | |
	Mean	Standard Deviation
3.70	1.16	0.07
2.40	1.14	0.10
0.958	1.38	0.09
0.651	1.27	0.11
0.360	1.37	0.12
0.305	1.38	0.10
0.117	1.41	0.45
All combined	1.30	0.11

[1] h_{min} calculated by Hamrock and Dowson Model Equation (1).

Table 12. Data for Comparing Commercial IR Detectors

	Barnes RM2A	Barnes RM50	AGA 680	Mod AGA 750	UTI 900
Automatic scanning option	No	yes	yes	yes	yes
scanning time (per frame)	---	1 sec	1/16 sec	1/25 sec	1 sec
Magnification-maximum usable	15X	10X	15X	ca 5X	6X
line scanner	no	yes	yes	no	yes
scanning time of line	NA	1 sec	1/16 sec		1/400 sec
Output mode	m Volt	picture	picture isotherm unit	picture isotherm unit	picture
spacial resolution, m (minimum detector spotsize)	$3.8 * 10^{-5}$	$15 * 10^{-5}$	$10 * 10^{-5}$	$125 * 10^{-5}$	$5 * 10^{-5}$
Minimum detector temperature difference of BB at room temperature	0.5C	0.1C	0.15C	0.25C	0.20C
Absolute temperature accuracy for gray body ($\epsilon = 0.2$)	2.5C	5C	5C	2C	---
Working distance (at magnification listed)	$2.5 * 10^{-2}m$	$10 * 10^{-2}m$	$3.5 * 10^{-2}m$	$5 * 10^{-2}m$	$1.25 * 10^{-2}m$
Tested in Laboratory	yes	yes	yes	yes	no

Table 13. Load per unit length and corresponding
Maximum Hertzian Pressure

| Case 1 | 87.6 kN/m (500 lb/in) | 0.5 GPa (72746 psi) |
| Case 2 | 876 kN/m (5000 lb/in) | 1.6 GPa (230,043 psi) |

Table 14. Zero pressure value of viscosity in each loading
case, and corresponding limiting shear stress
parameters

Dynamic Viscosity at 30°C	Slope of the Limiting Shear Stress-pressure Relation
0.863 Pas $(1.24 \times 10^{-4} \text{ lbs/in}^2)$	0.01
11.68 Pas $(1.69 \times 10^{-3} \text{ lbs/in}^2)$	0.01 and 0.005
91.0 Pas $(1.32 \times 10^{-2} \text{ lbs/in}^2)$	0.005 and 0.001

Table 15. Physical Input Parameters

Pressure coefficient of viscosity	14.5 GPa^{-1} ($1 \times 10^{-4} \text{ psi}^{-1}$)
Equivalent Radius	0.0127 m (0.5 in)
Equivalent modulus of Elasticity	220 GPa (3.3×10^{7} psi)
Materials	steel on steel
Rolling Speed $\bar{u}$	127 cm/sec (50 in/sec) to 1778 cm/sec (700 in/sec)

Table 16. Conventional Dimensionless Parameters

Load Parameters $\left(\dfrac{E_r \cdot R}{w/L}\right)$ W	$3.3 \times 10^{+4}$ and $3.3 \times 10^{+3}$
Material Parameter G $\quad (\alpha \cdot E_r)$	$3.3 \times 10^{+3}$

Speed parameter $U = \left(\dfrac{\mu_o \bar{u}}{E_r \cdot R}\right)$ has the following ranges:

$\mu_o = 0.863$ Pas	3.76×10^{-10} to 5.26×10^{-9}
$\mu_o = 11.68$ Pas	5.12×10^{-9} to 7.17×10^{-8}
$\mu_o = 91.0$ Pas	4×10^{-8} to 5.6×10^{-7}
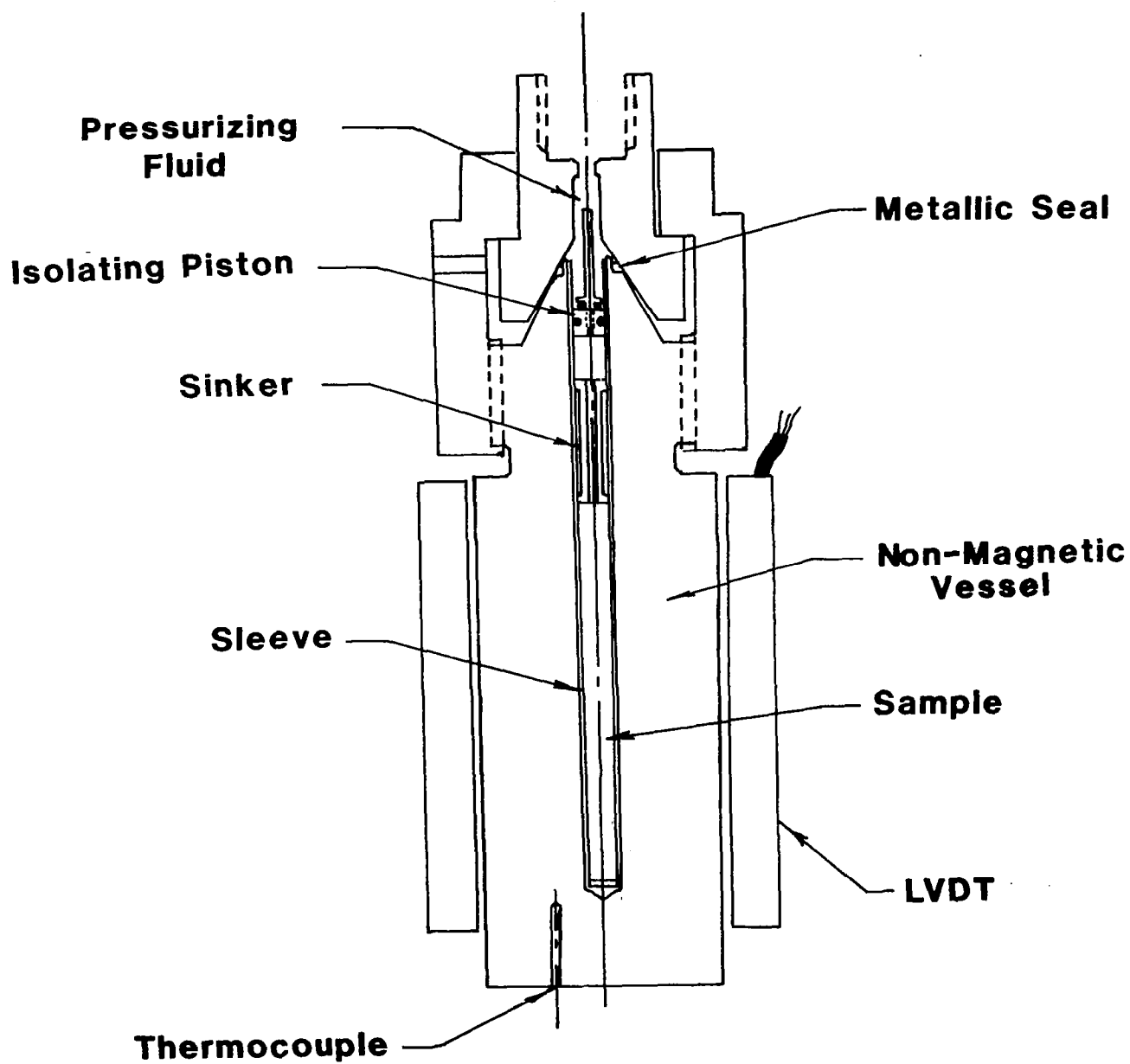
Figure 1. High Temperature Viscometer
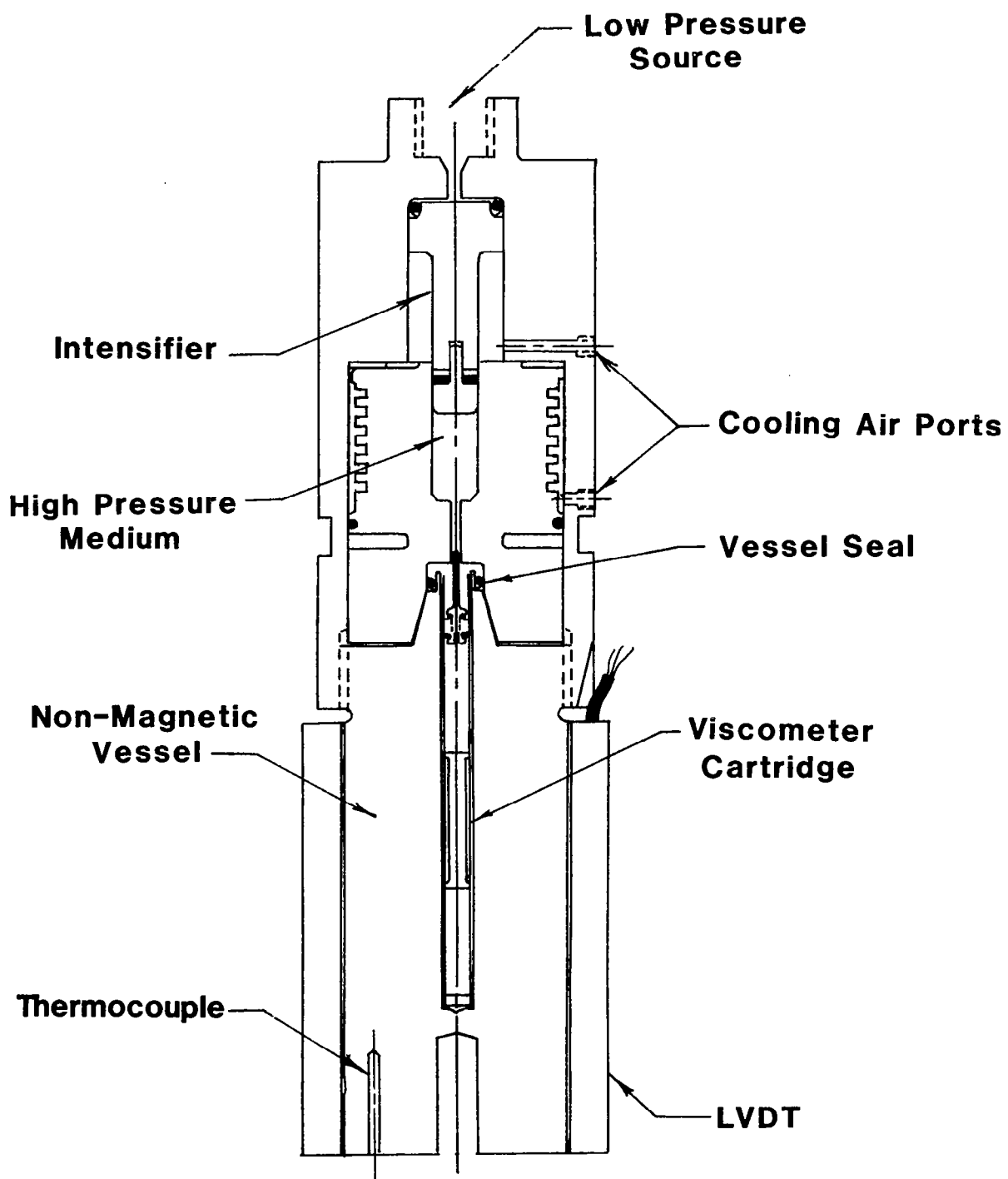
Figure 2. High Pressure Viscometer

Roller

Disc

Timing Belts

Microscope or IR Detector

Tachometer

Sideslip
Micrometer

Traction
Force Transducer

Thrust Bearing

Slide-Roll
Micrometer

Motor

Position Transducer

Load Weights
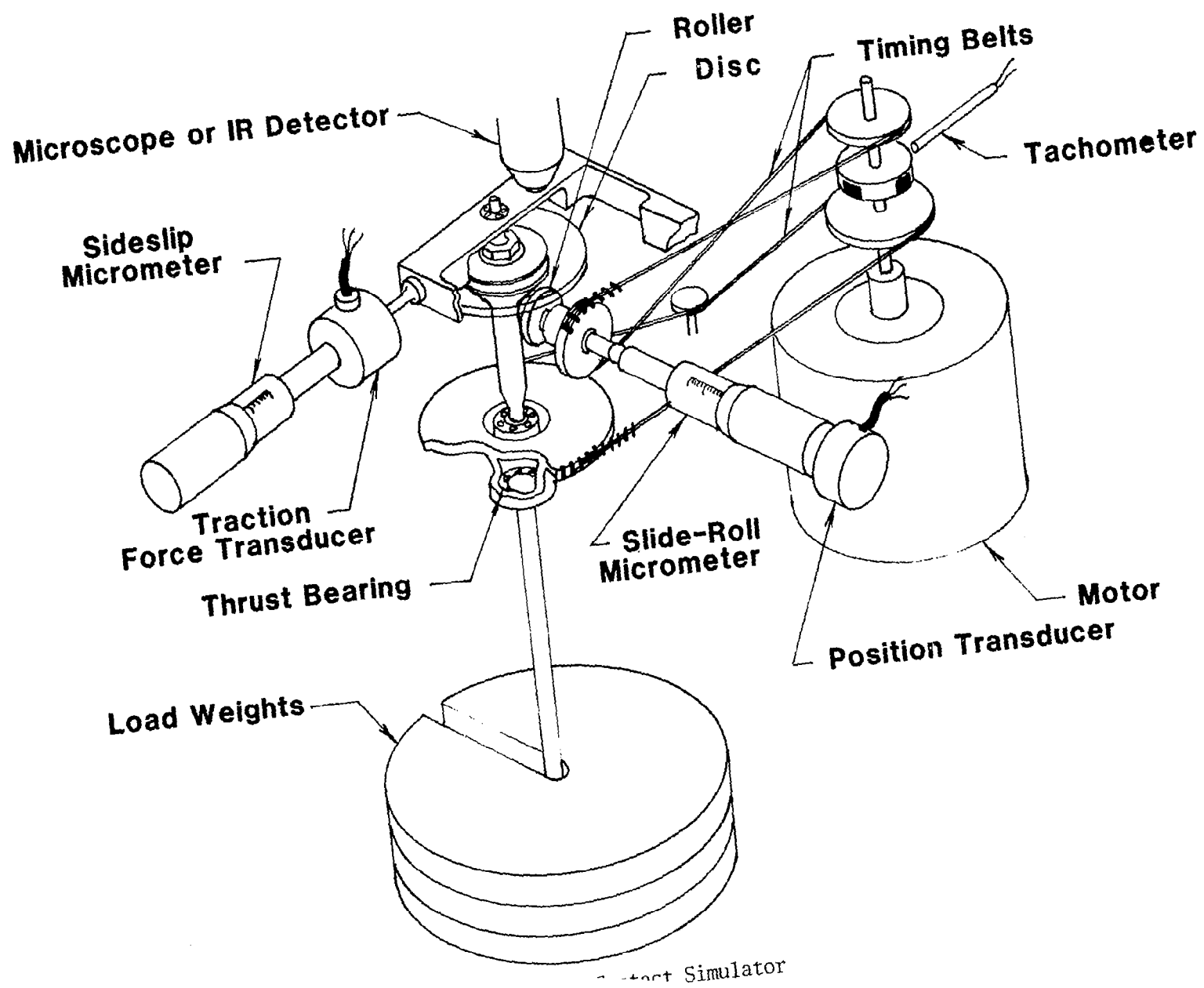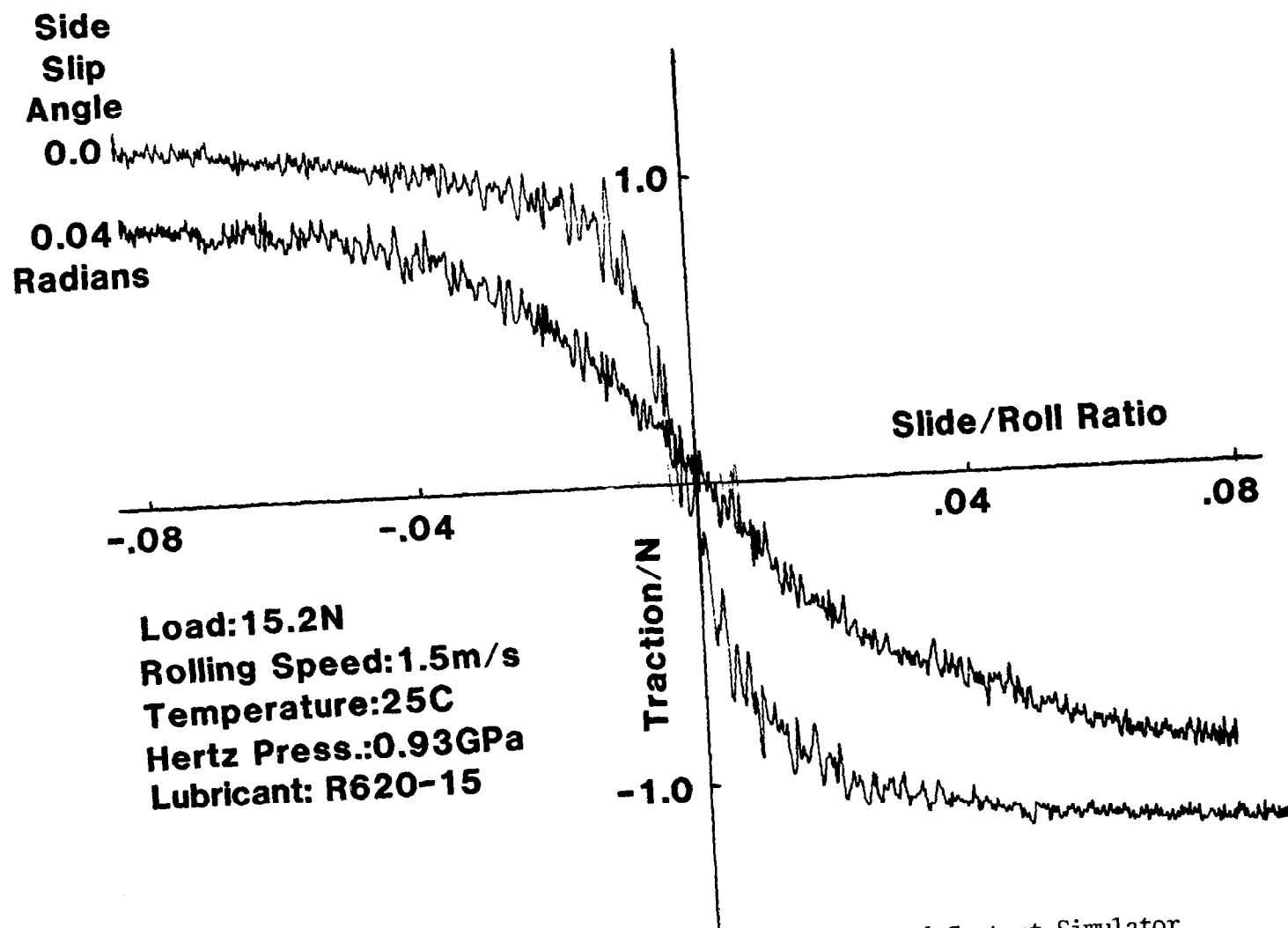
Contact Simulator

Figure 4. Preliminary Traction Curve from New Concentrated Contact Simulator
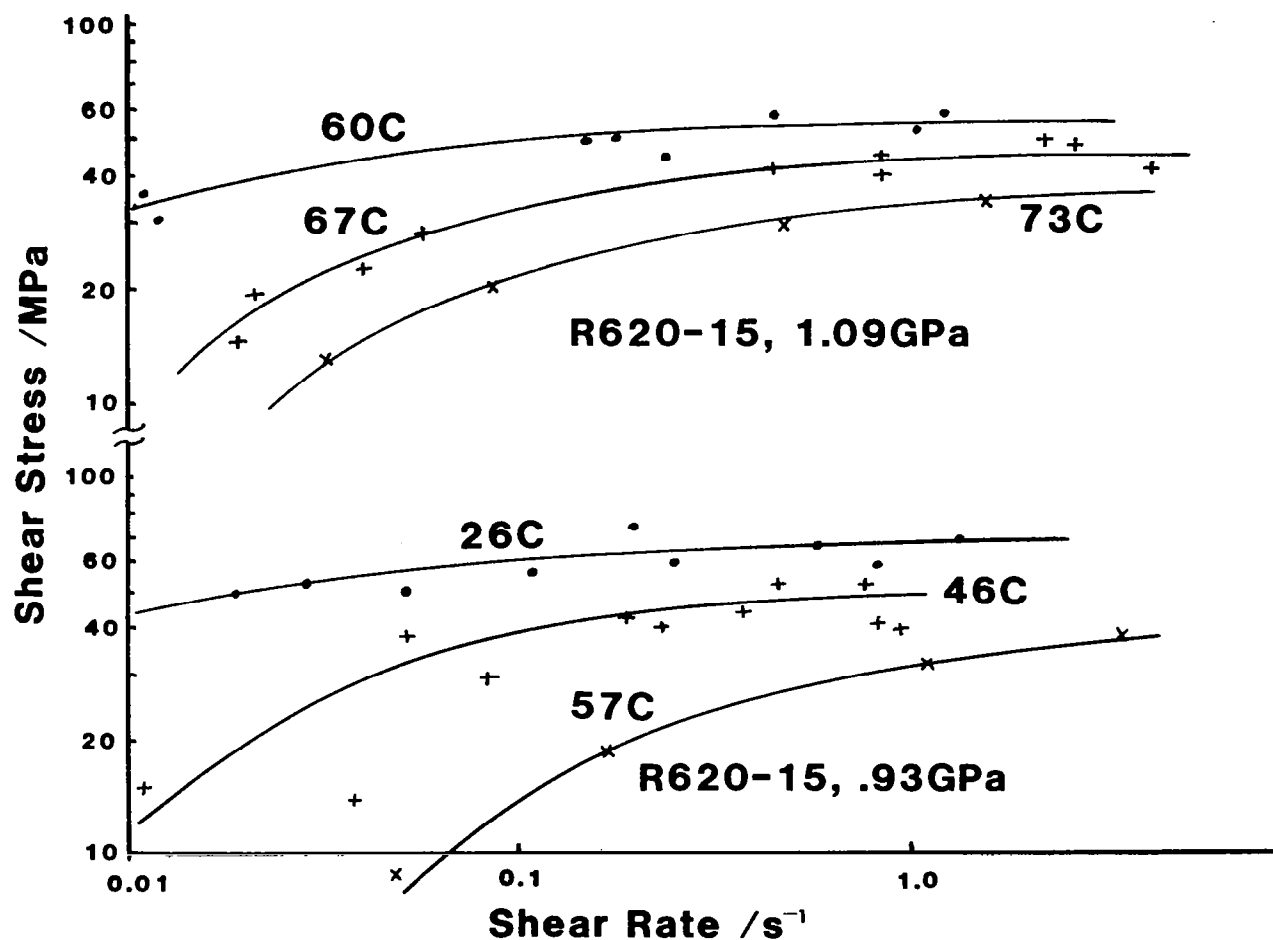
Figure 5. Flow Charts for Naphthenic Base Oil at Pressures of 1.09 GPa and 0.93 GPa
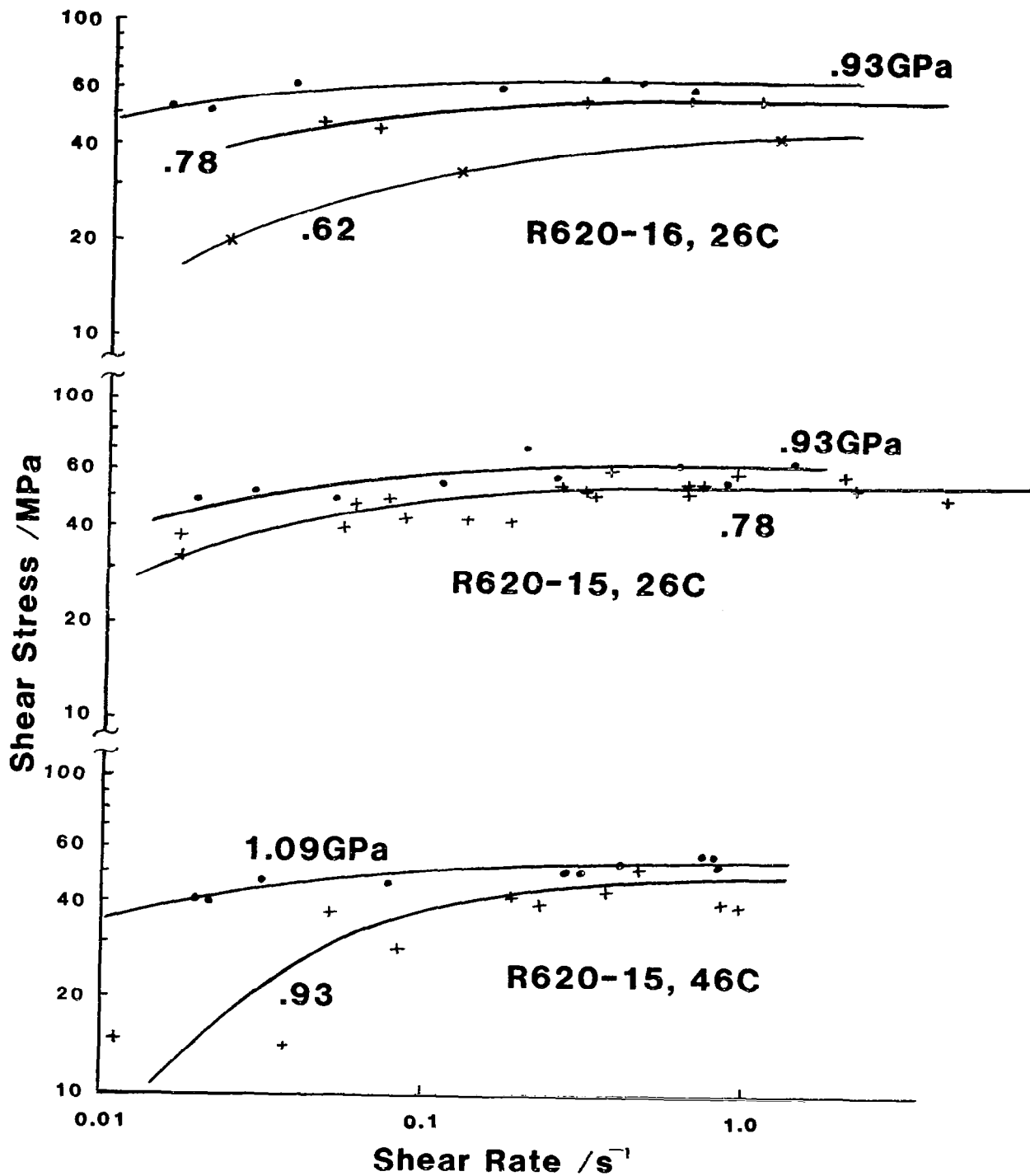
Figure 6. Flow Charts for Two Naphthenic Oils of Different
Viscosity
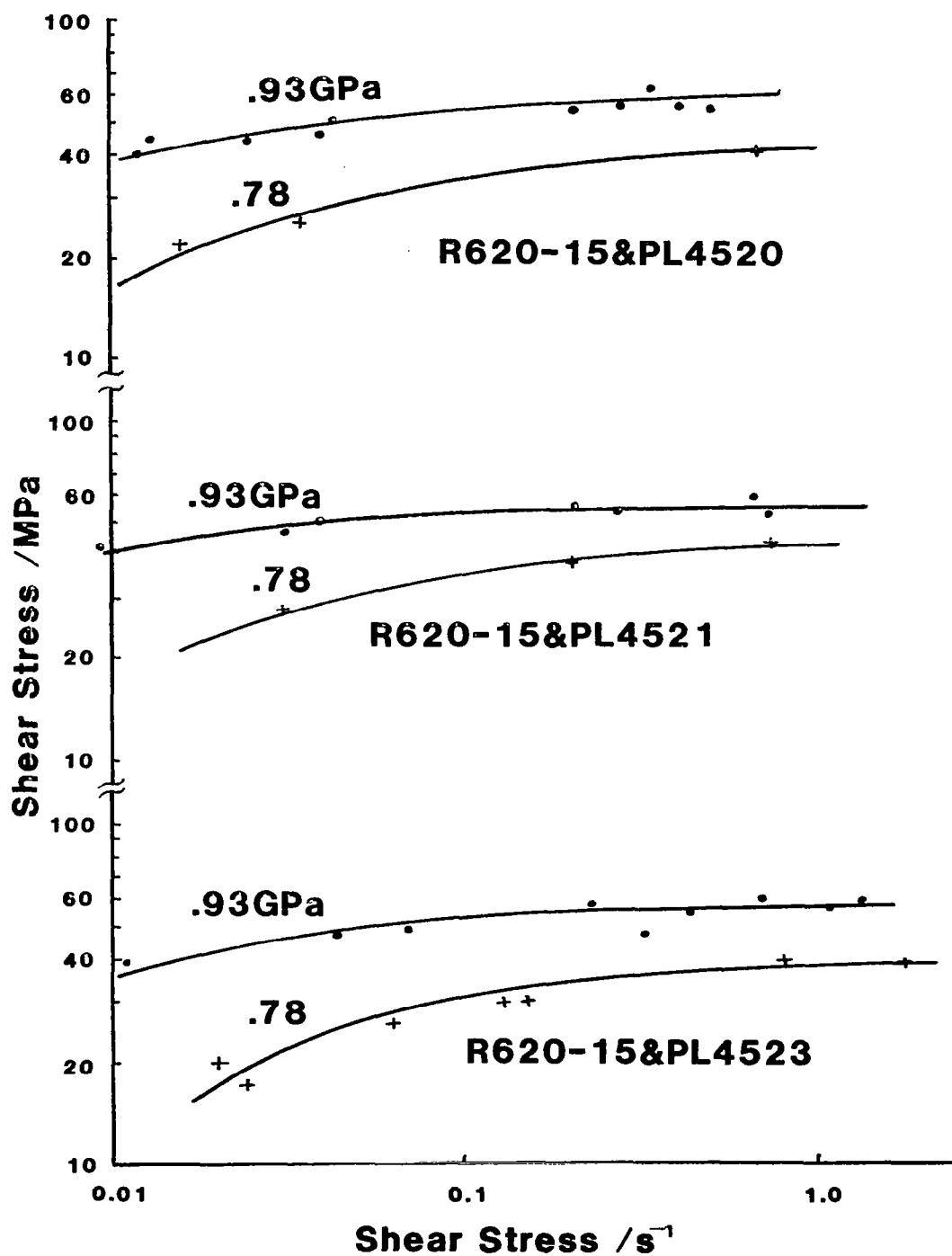
Figure 7. Flow Charts for Three Polymer Blends at 26C. (Identical Base Oil and Three Different Molecular Weight Polyalkyl-methacrylates.)
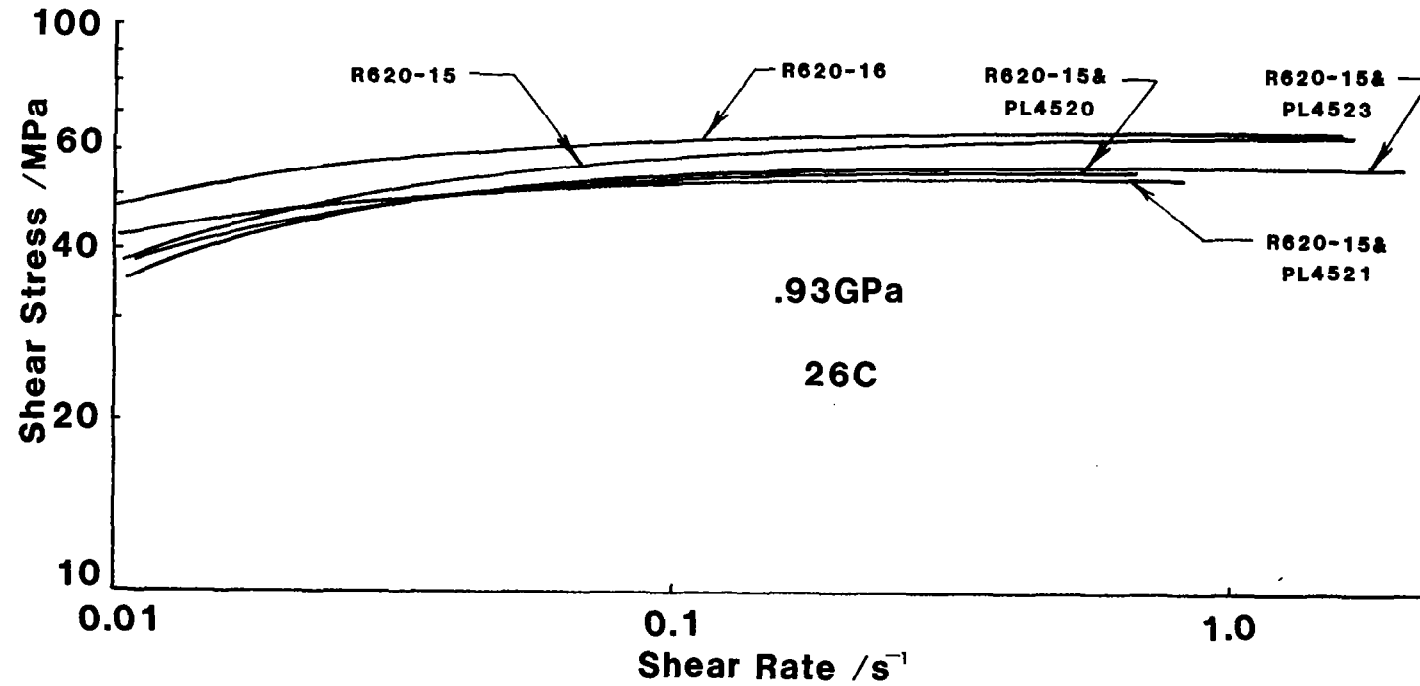
Figure 8.   Comparison of the Shear Behavior of Two Naphthenic Base Oils and
Three Blends of Polyalkylmethacrylate and Base Oil
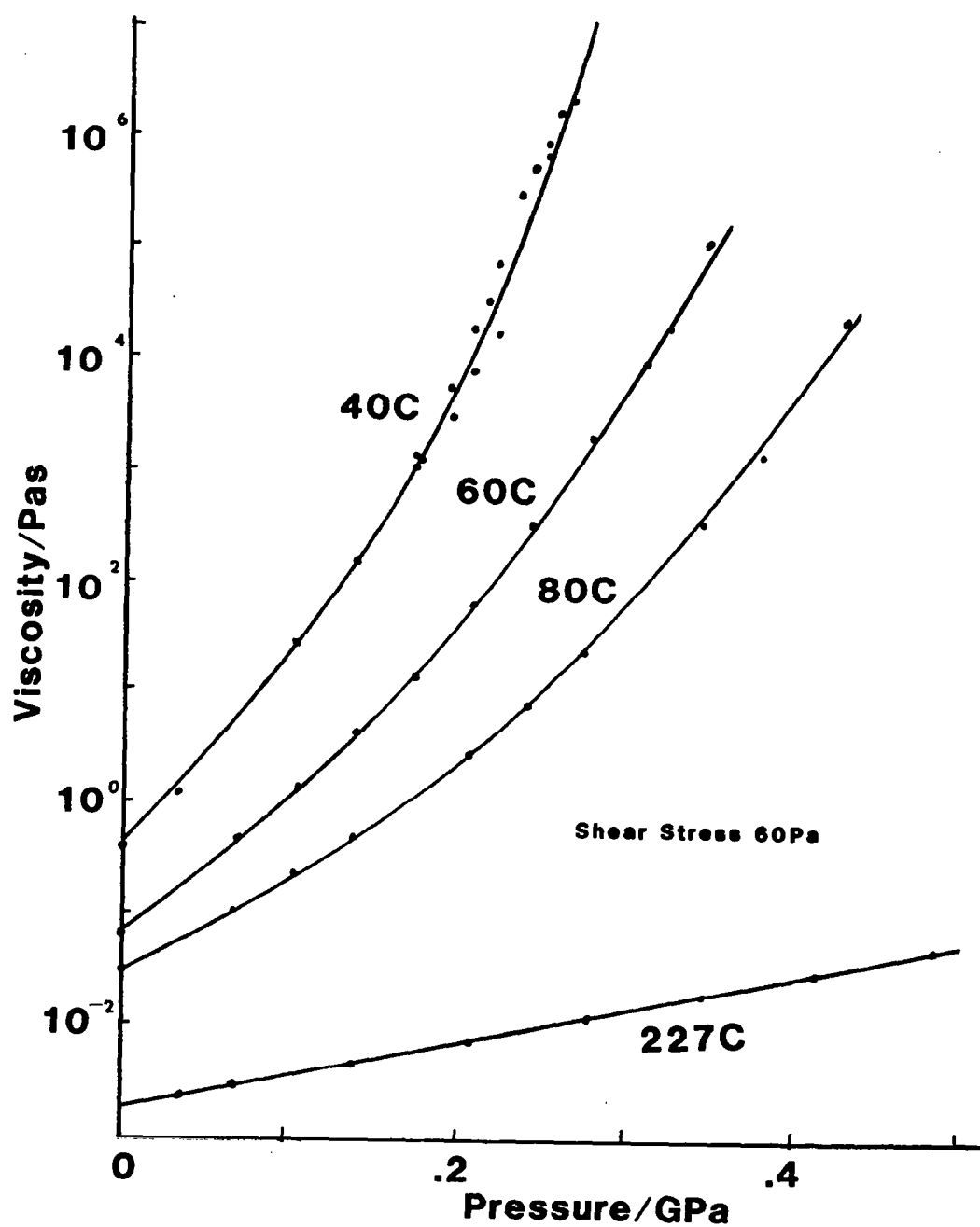
Figure 9. Pressure-Viscosity Isotherms for 5P4E
(Polyphenol Ether)
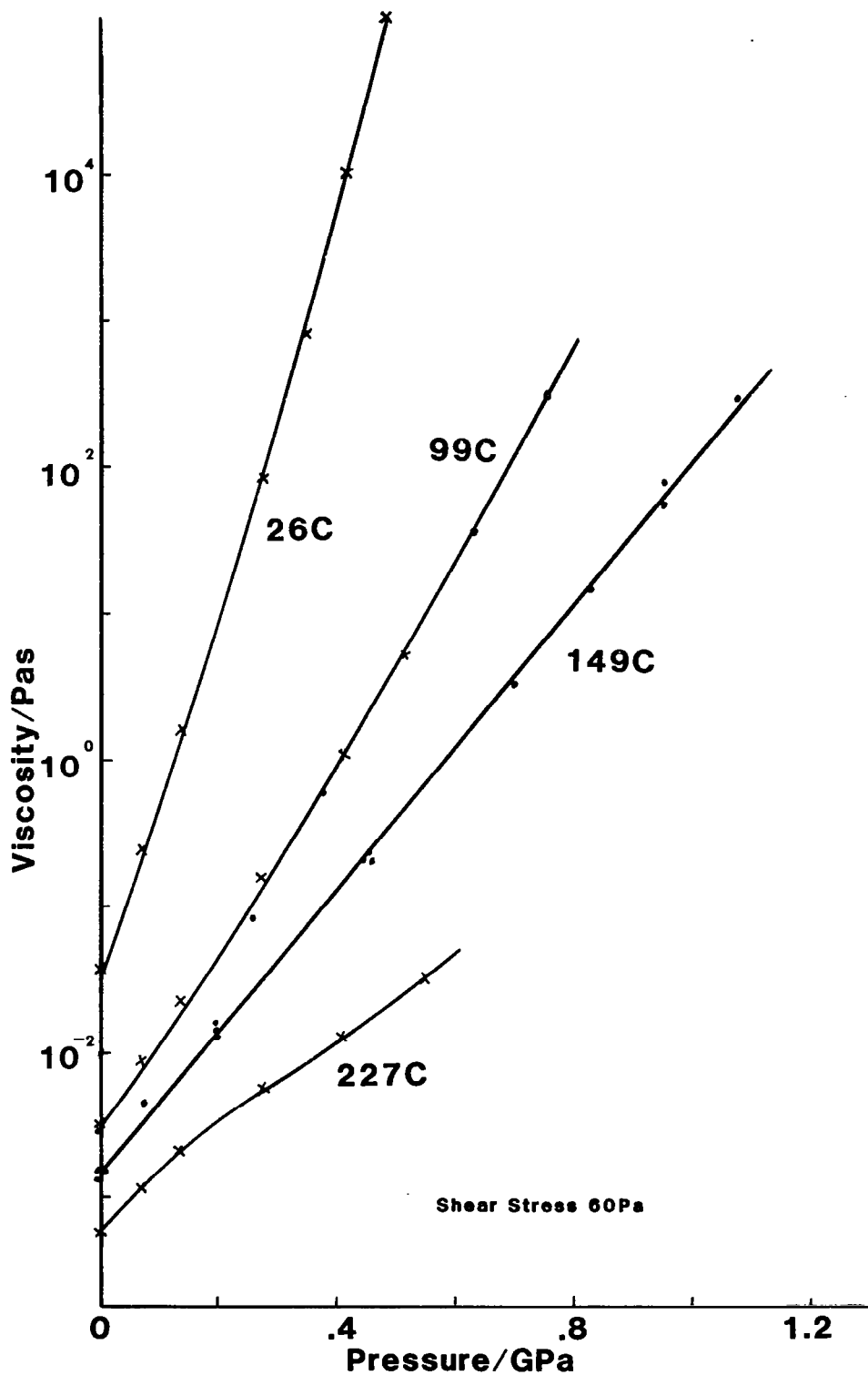
Figure 10. Pressure-Viscosity Isotherms for R620-15 from (•)
Extra-High Pressure Viscometer (x) High Temperature
Viscometer
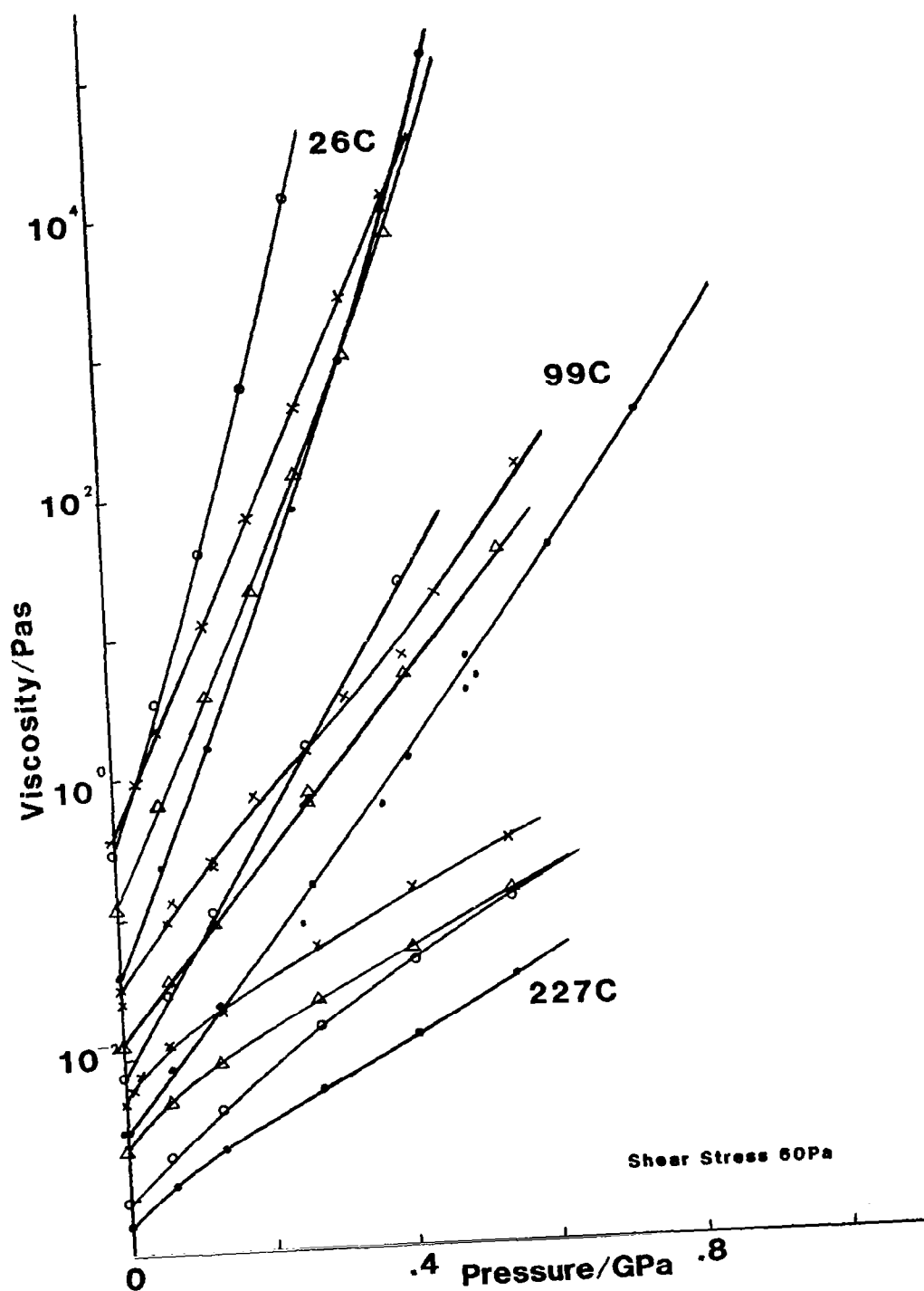
Figure 11. Pressure-Viscosity Isotherms for (•) R620-15, (o) R620-16, (x) R620-15 + PL4523, (Δ) R620-15 + PL4521
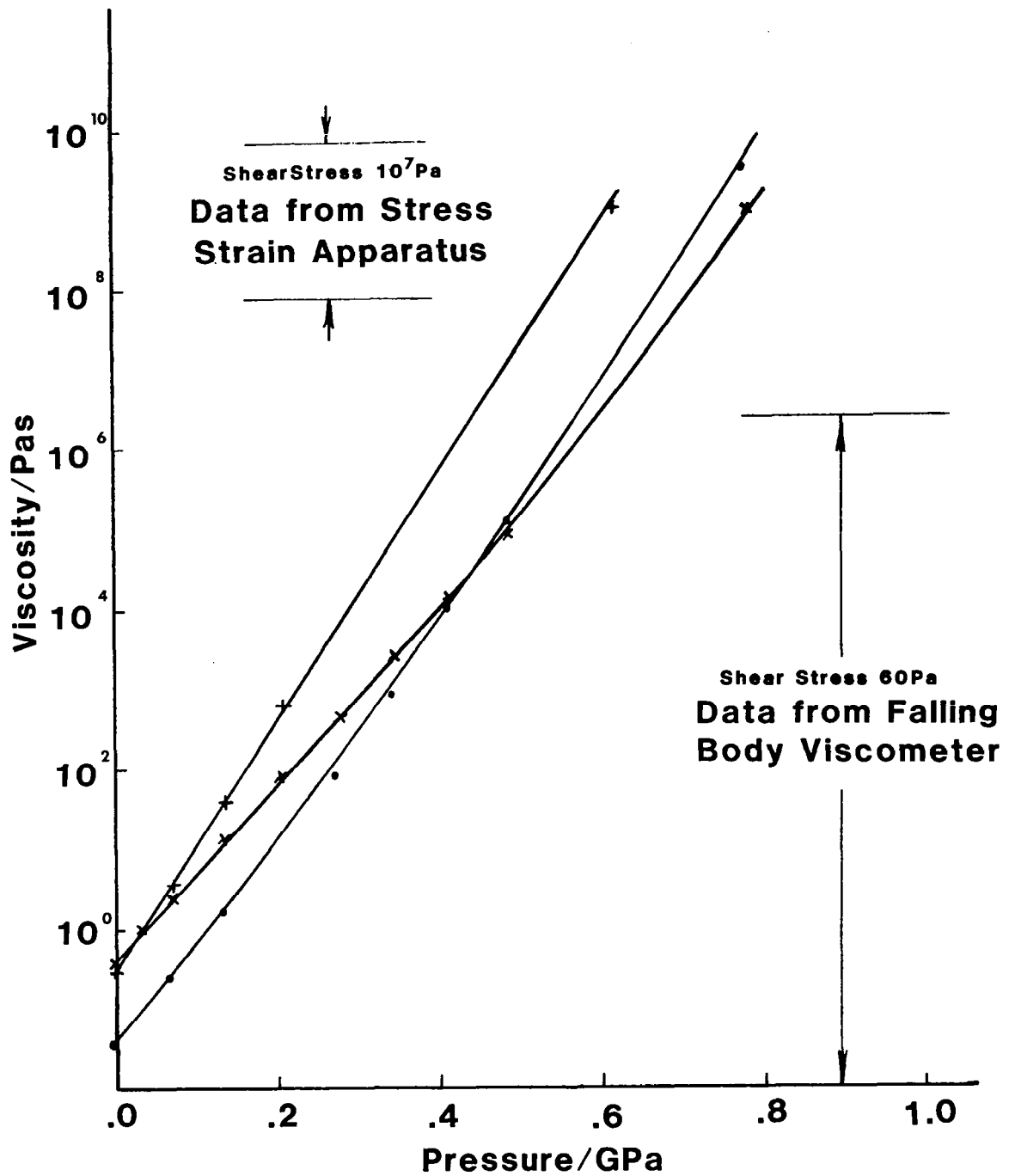
Figure 12. Low Shear Stress Viscosity by Two Techniques for
            (.) R620-15, (+) R620-16, (x) R620-15 + PL4523
            at 26C

Figure 13. EHD Simulator

HARDENED STEEL
CROWNED ROLLER

FLEXIBLE
COUPLING

3.2 cm

ALUMINUM BASE

BEARINGS

OIL BATH

7.6 cm

FULL SCALE
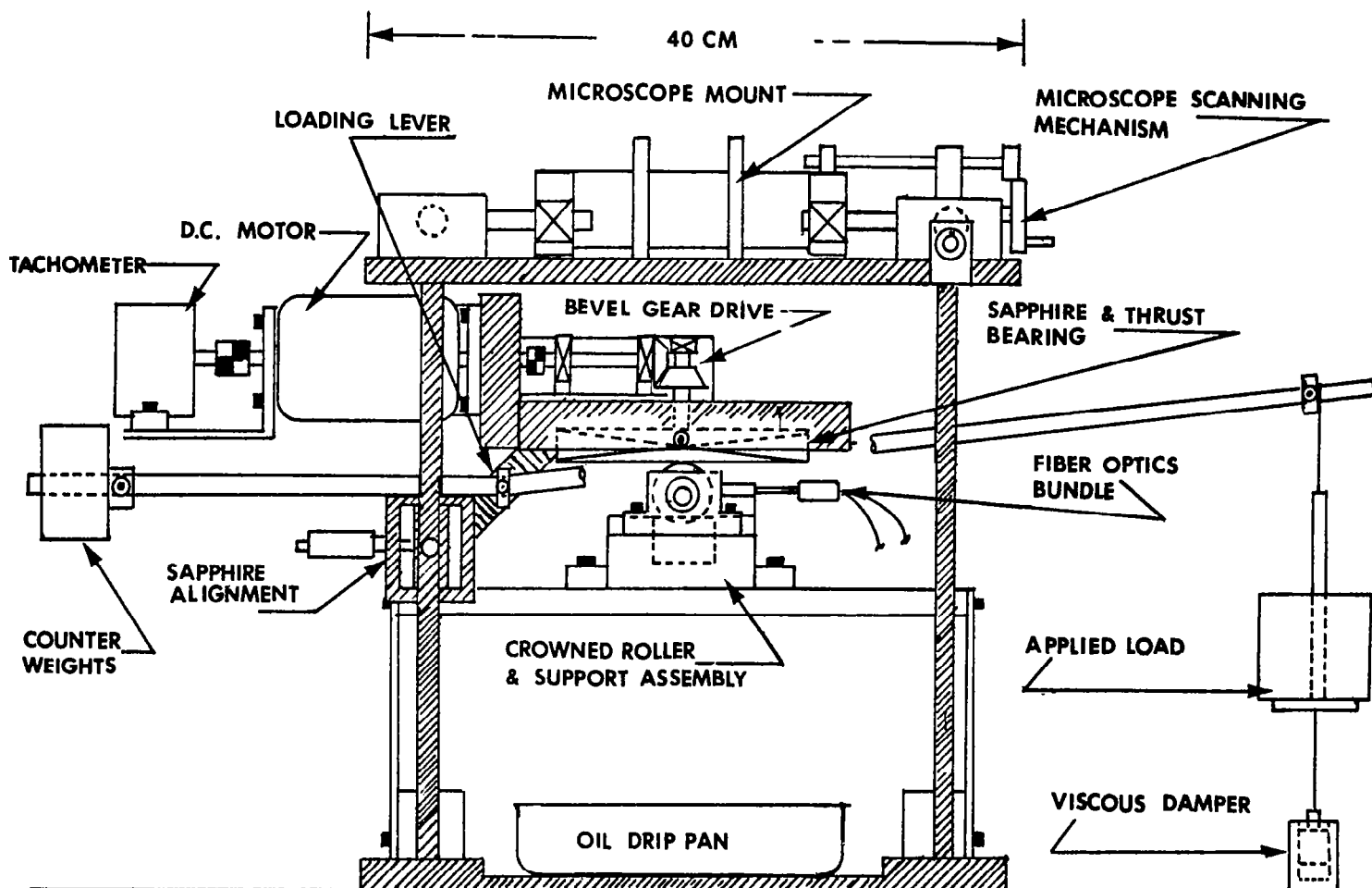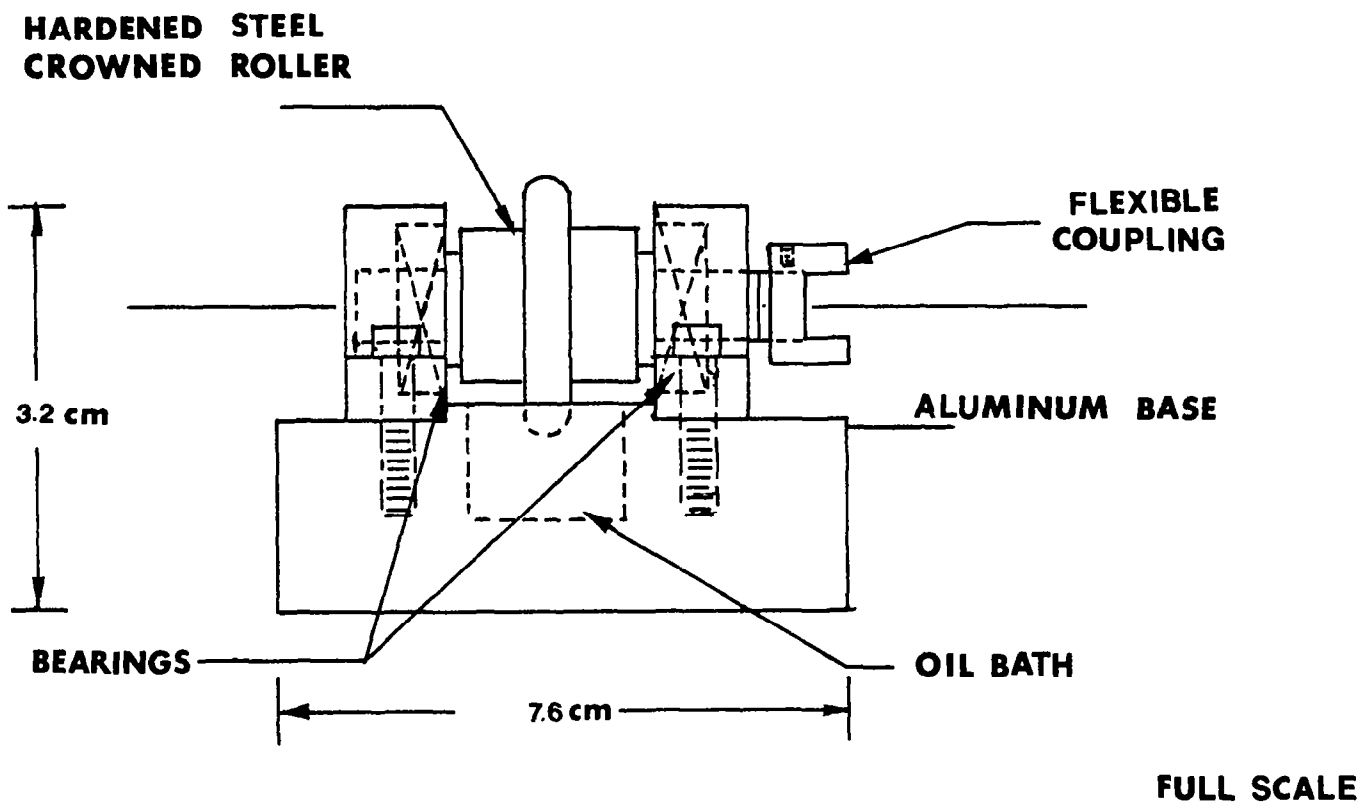
Figure 14. Crowned Roller and Support Assembly
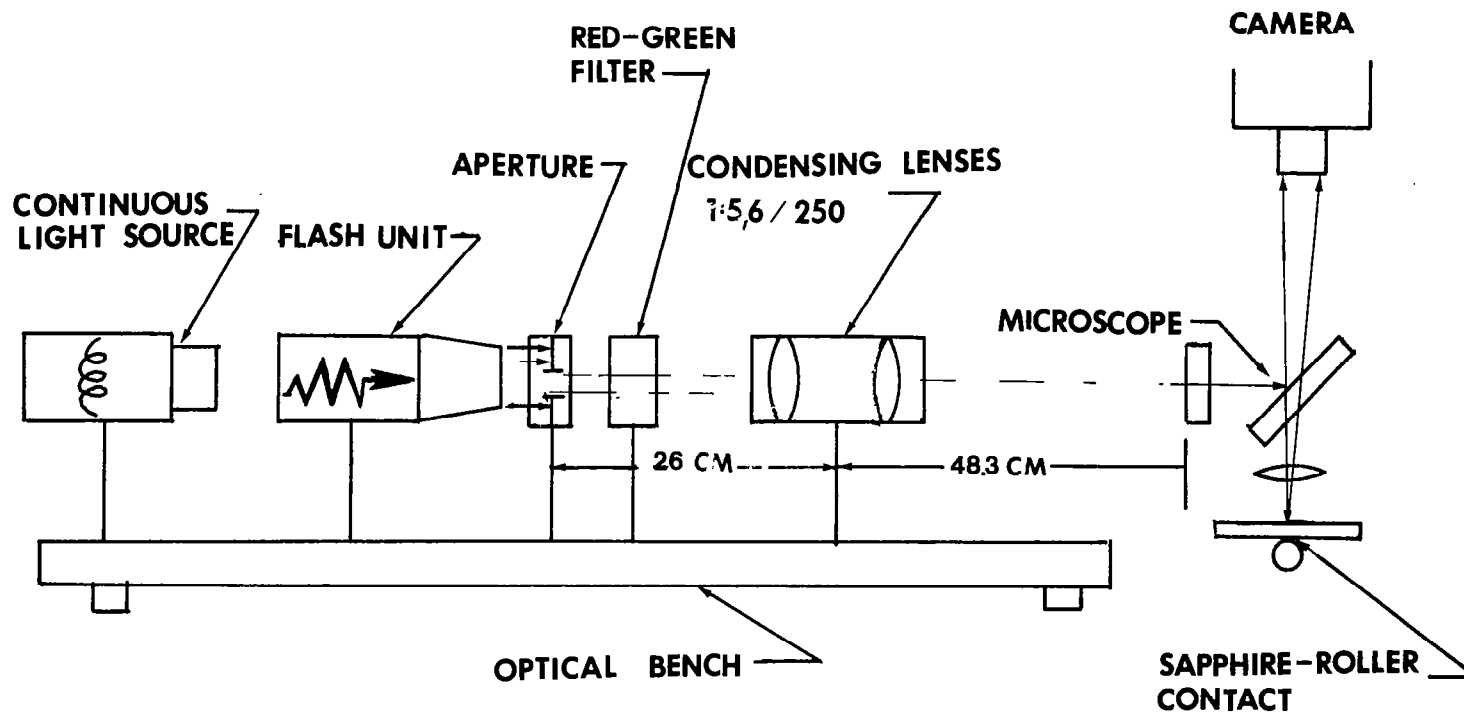
Figure 15. Schematic Diagram of the Optical System

$$K = 1.033 \left[\frac{R_y}{R_x} \right]^{0.636}$$
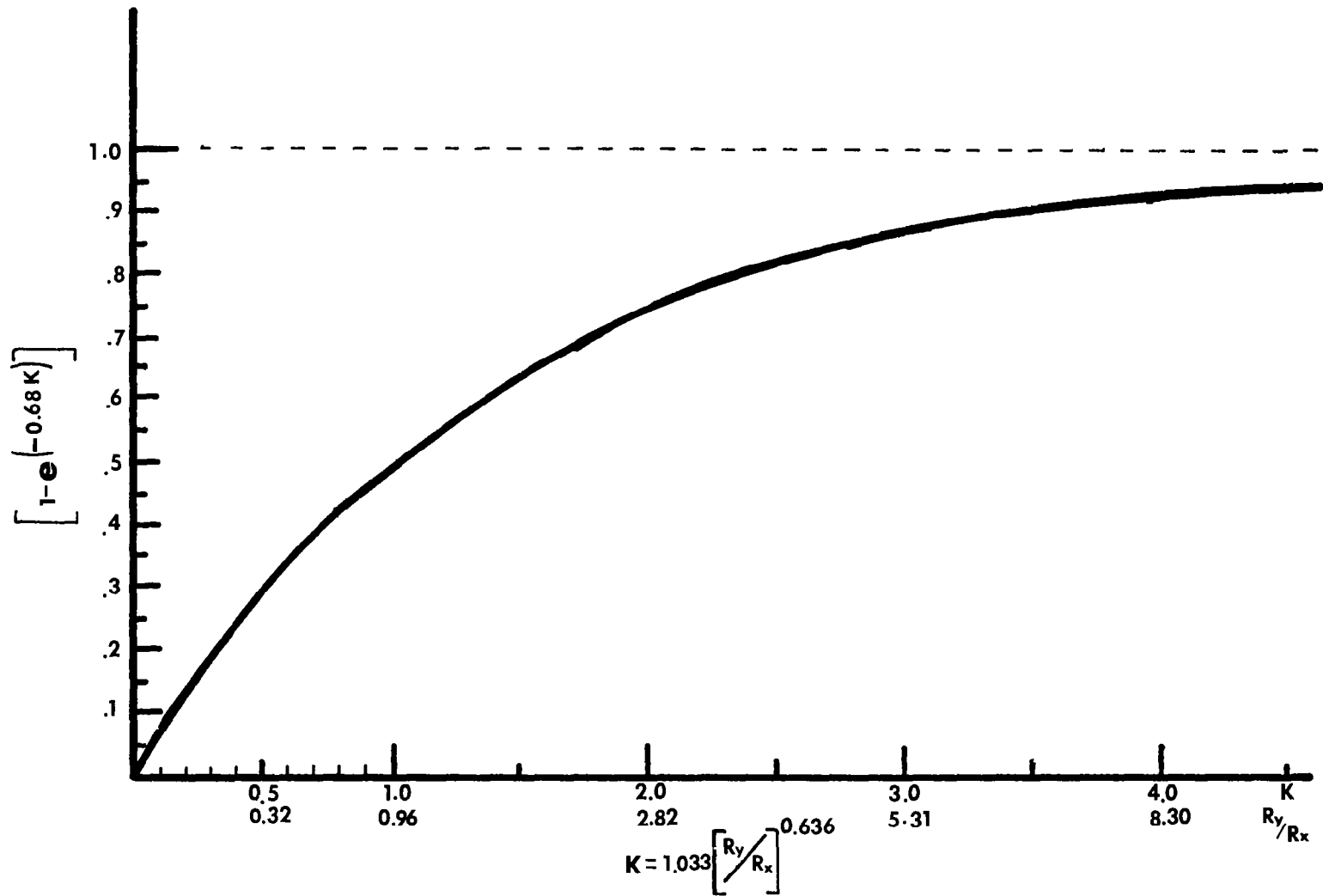
Figure 16. The Relationship between Ellipticity Ratio and Minimum Film Thickness predicted by the Hamrock and Dowson Equation.

Figure 17.* Interferogram: $k = 3.7$, $R_y/R_x = 7.42$, $u = 0.5$ m/s, $F = 113.4$ N, $h_{min.exp.} = 1.1$ μm
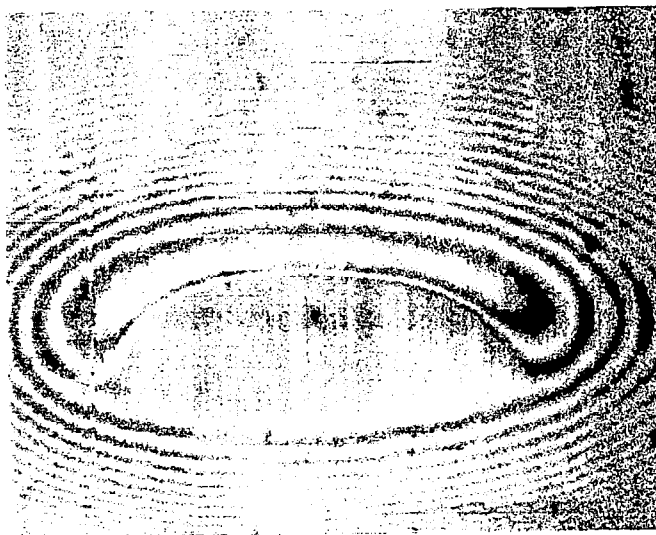
Figure 18.* Interferogram: $k = 2.37$, $R_y/R_x = 3.77$, $u = 0.5$ m/s, $F = 69.8$ N, $h_{min.exp.} = 1.02$ μm

*flow from bottom to top of figure
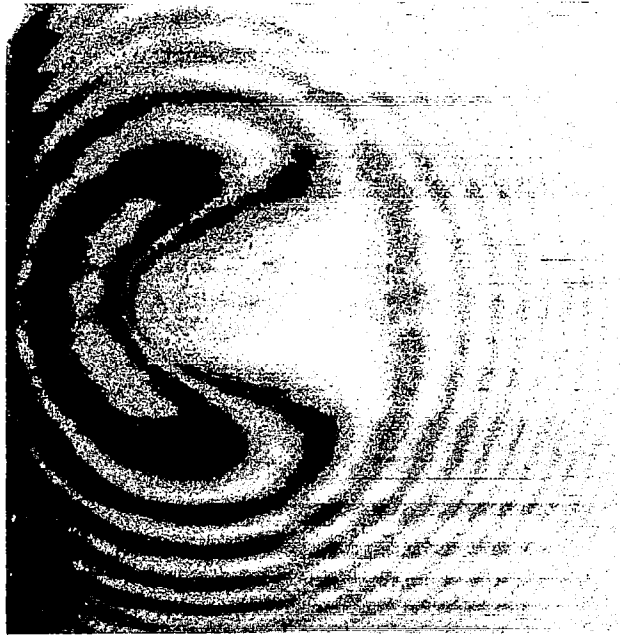
Figure **19.*** Interferogram: $k = 0.958$, $R_y/R_x = 0.99$, $u = 0.5$ m/s, $F = 22.7$ N, $h_{min.exp.} = 0.89$ μm
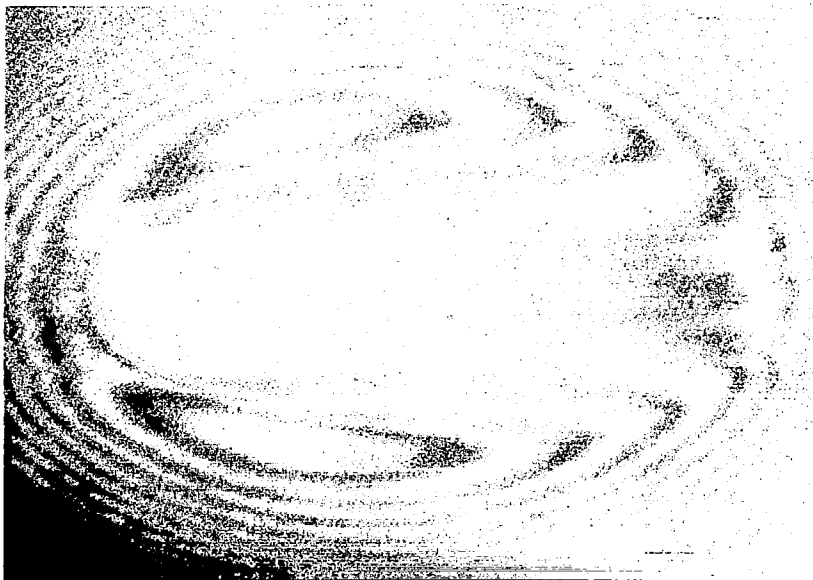
Figure 20.* Interferogram: $k = 0.65$, $R_y/R_x = 0.54$, $u = 0.9$ m/s, $F = 111.6$ N, $h_{min.exp.} = 0.7$ μm

*flow from right to left of figure

Figure 21.*   Interferogram: k = 0.36, R_y/R_x = 0.21, u = 0.5 m/s, F = 52N, $h_{min.exp.}$ = 0.32 μm
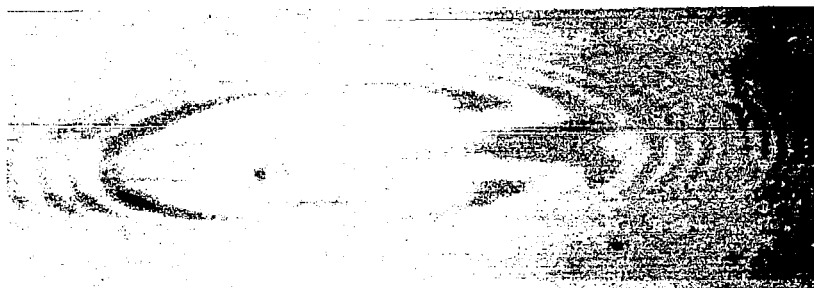
Figure 22.*   Interferogram: k = 0.30, R_y/R_x = 0.16, u = 0.5 m/s, F = 26.2N, $h_{min.exp.}$ = 0.28 μm
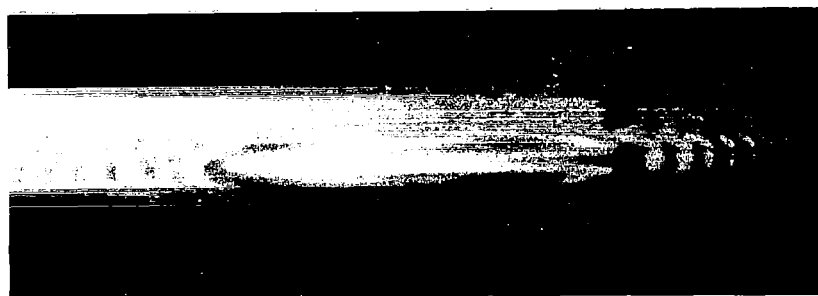
Figure 23.*   Interferogram: k = 0.117, R_y/R_x = 0.036, u = 0.9 m/s, F = 6.7N, $h_{min.exp.}$ = 0.2 μm

*flow from right to left of figure
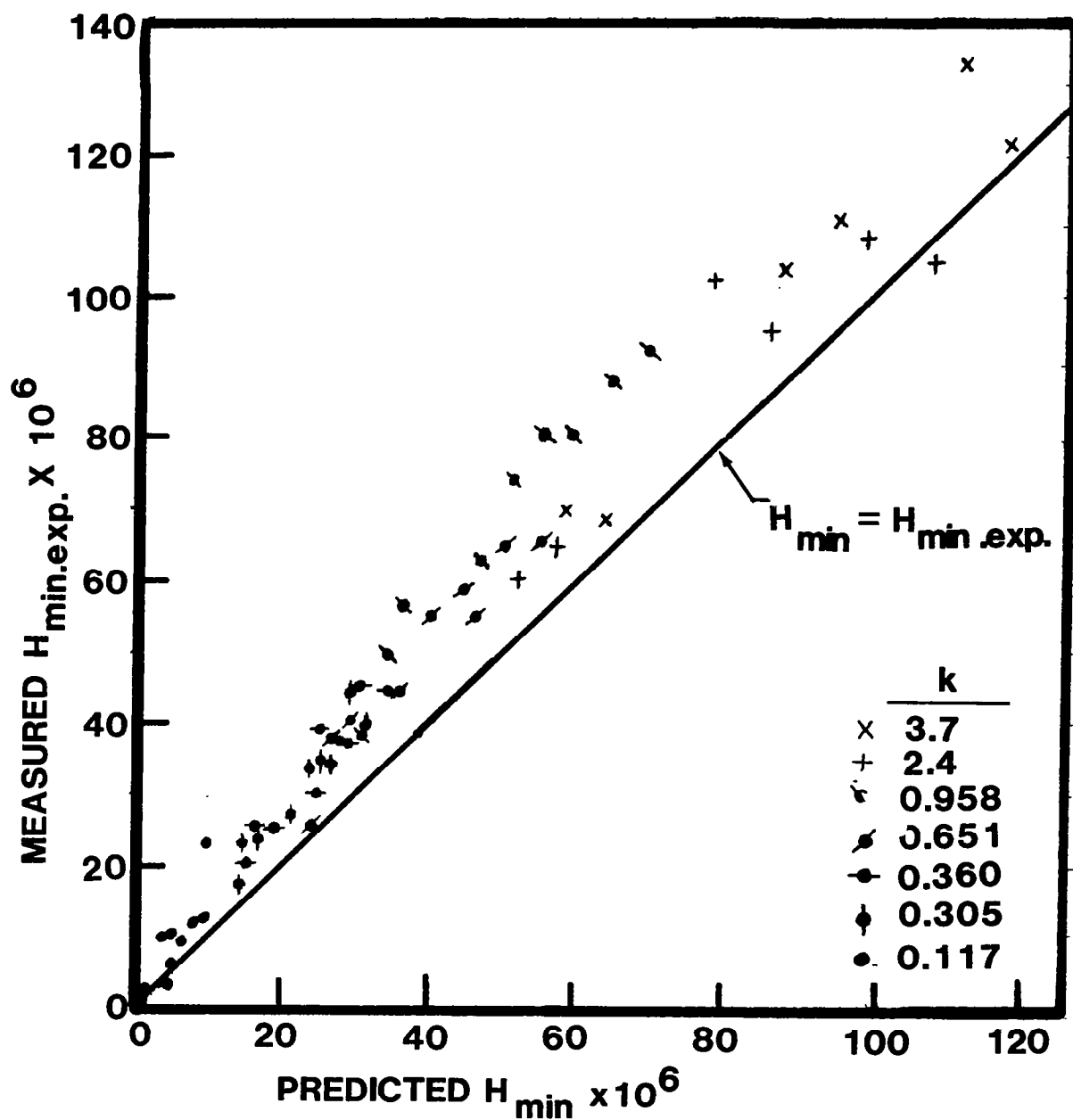
Figure 24. Predicted Dimensionless Minimum Film Thickness vs.
Measured Dimensionless Minimum Film Thickness
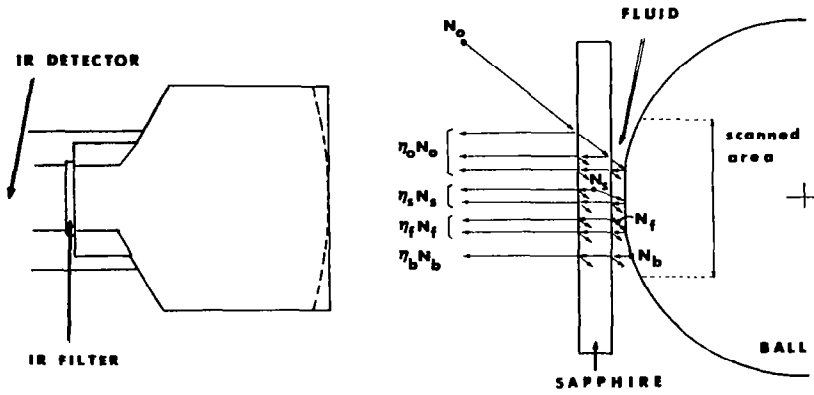
Figure 25. Sources of IR emission entering detector lens
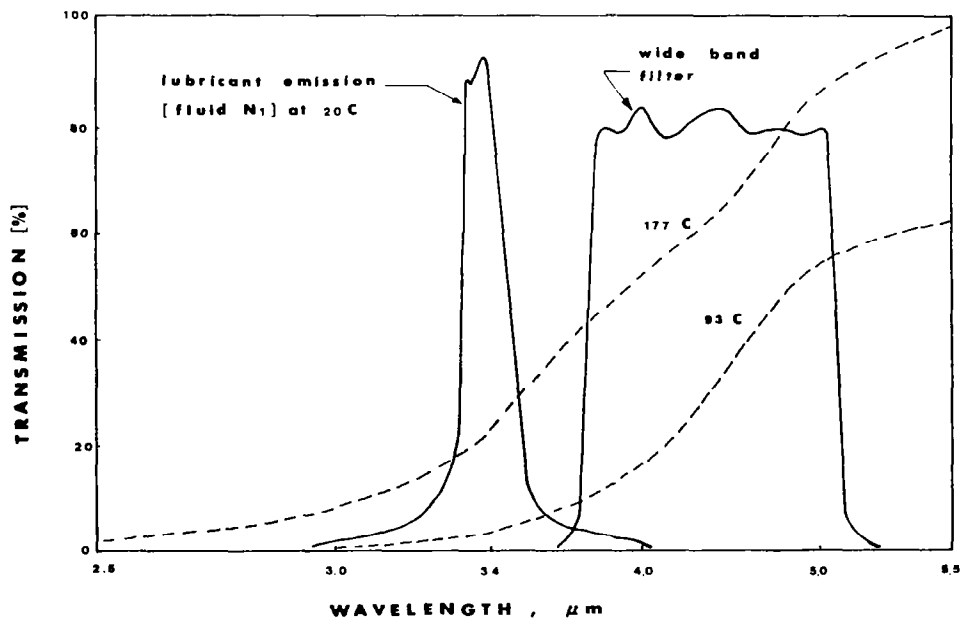
Figure 26. Transmission and emission of fluid and filter

100
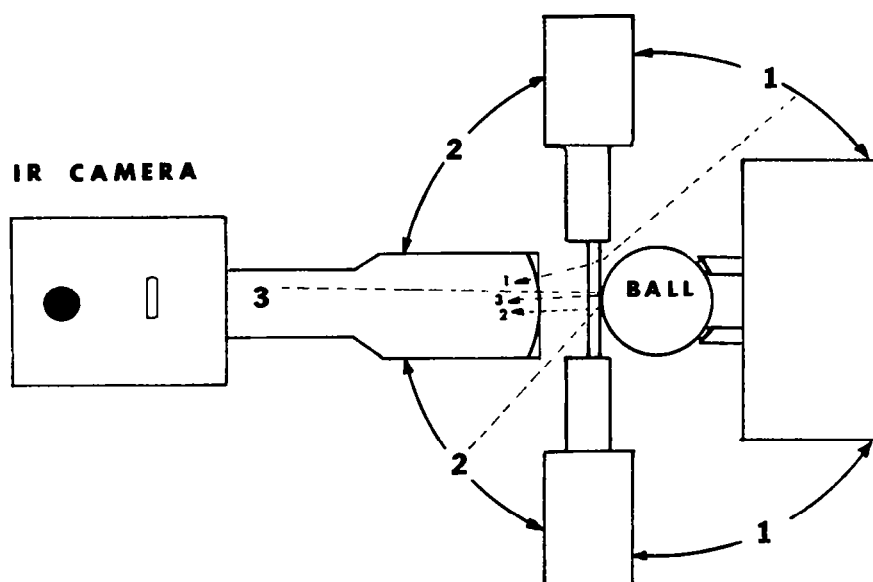
Figure 27. Sources of ambient radiation
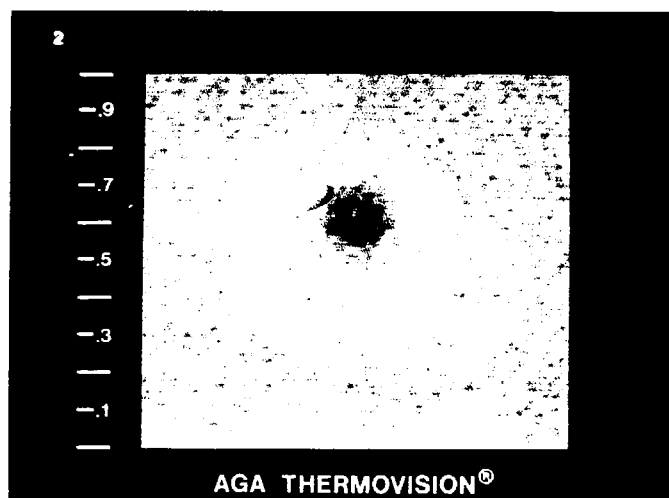
Figure 28. Dark spot reflection of IR lens by ball
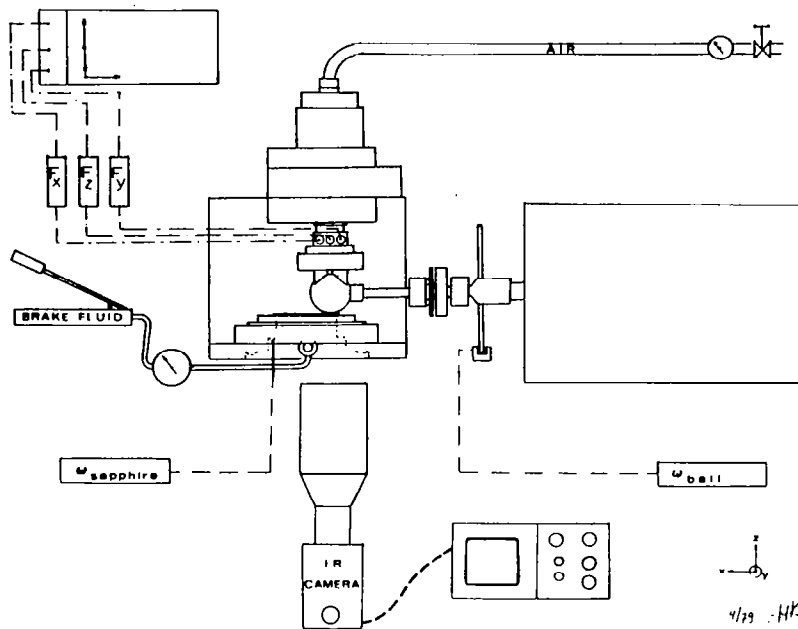
Figure 29. Schematic layout of the EHD simulator
and attached equipment
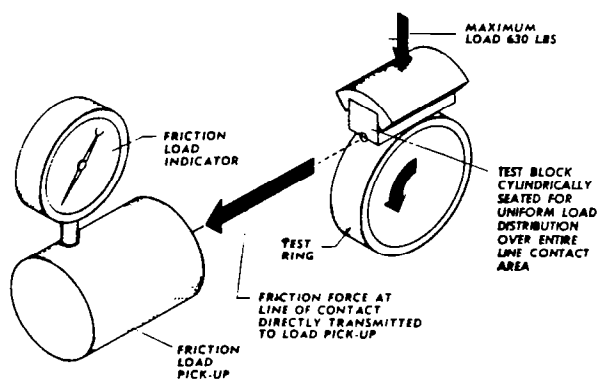
Figure 30. Schematic of LFW-1 test apparatus

RANGE

(a)
Sapphire
Holder
Radiation
Level

(b)
Wake
Radiation
Level

(c)
EHD
Center
Radiation
Level

Direction of Ball Motion
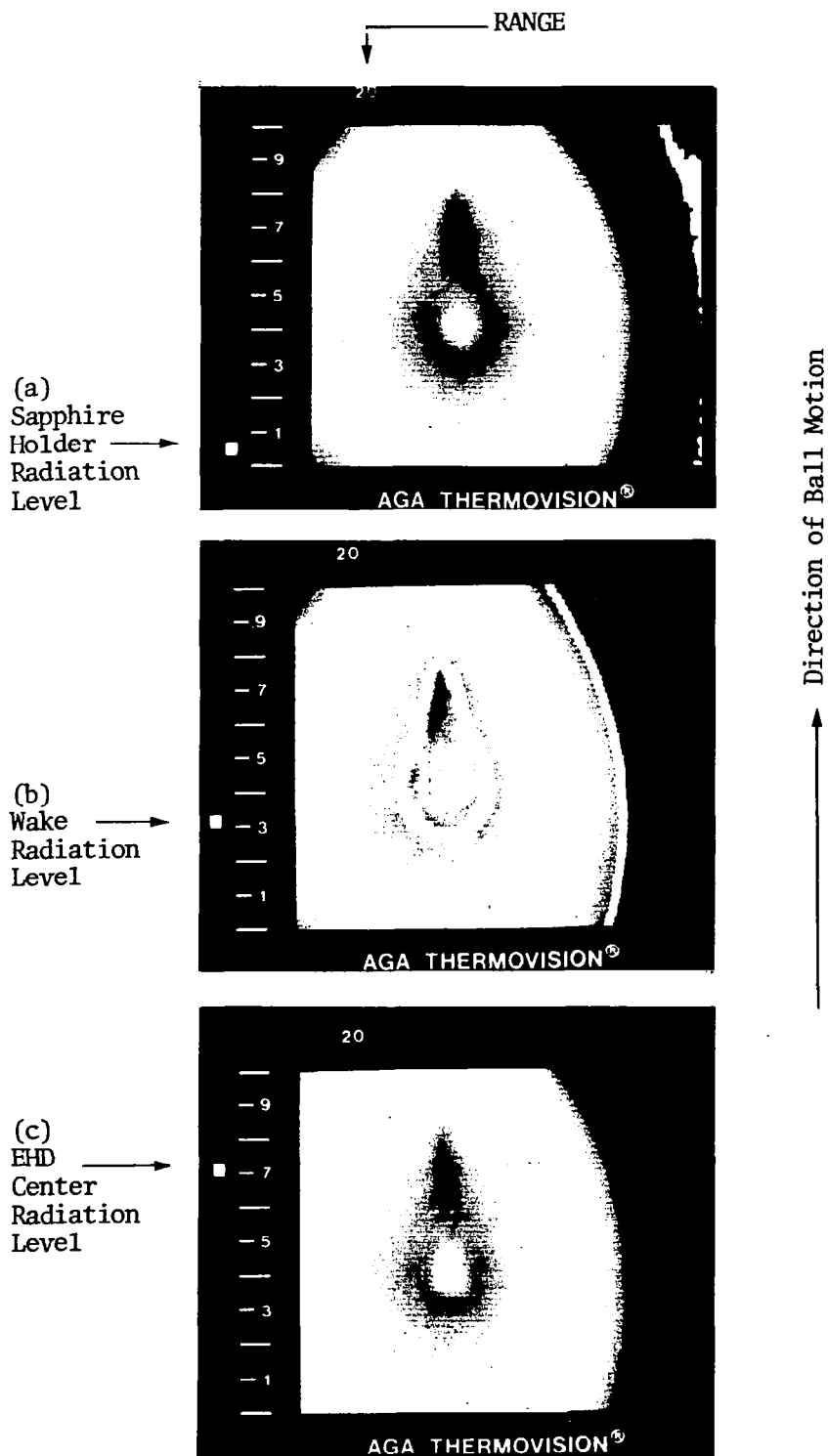
Figure 31.   Radiation levels on ball and sapphire holder in sliding
              conditions.   Iso-radiation levels are white.
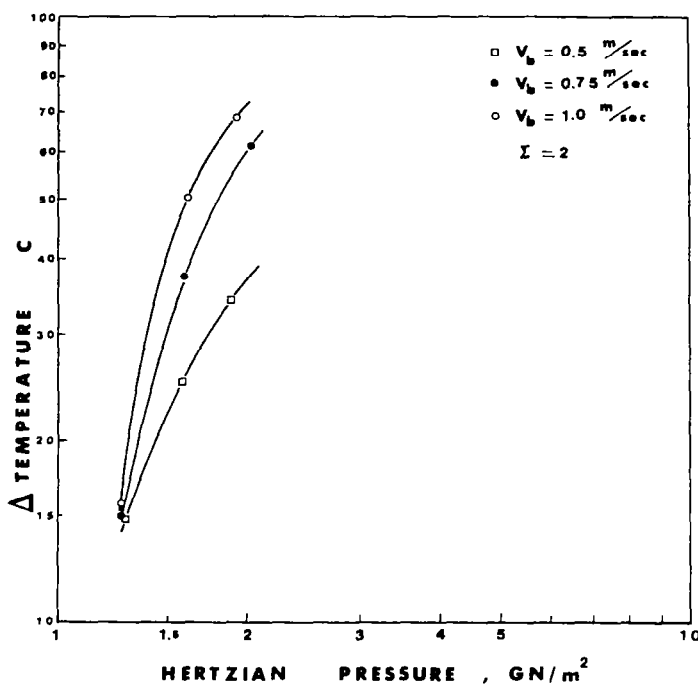
Figure 32. Temperature difference between EHD center and wake, in sliding conditions, for N1
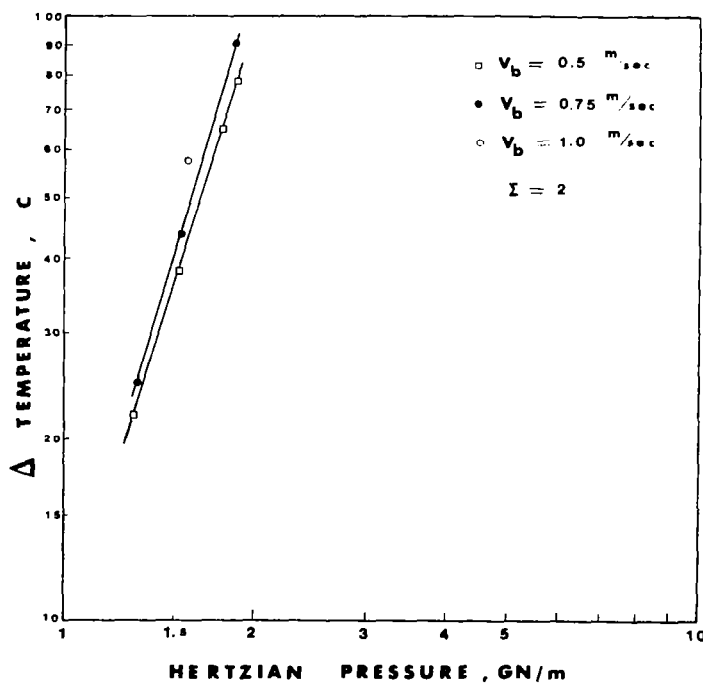
Figure 33. Temperature difference between EHD center and wake, in sliding conditions, for Santotrac 50
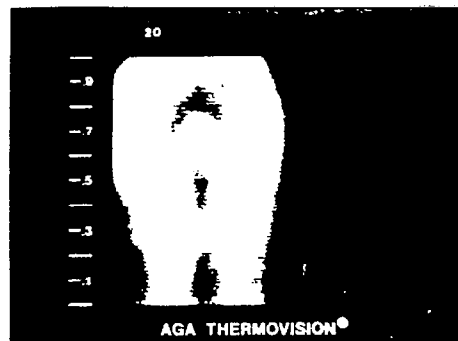
Figure 34. Infrared picture of sliding contact to illustrate the "horseshoe" around the EHD contact.

Operating conditions: V_{ball} = 0.75 m/sec

σ_{Hz} = 1.75 GN/m^2

Fluid: N1
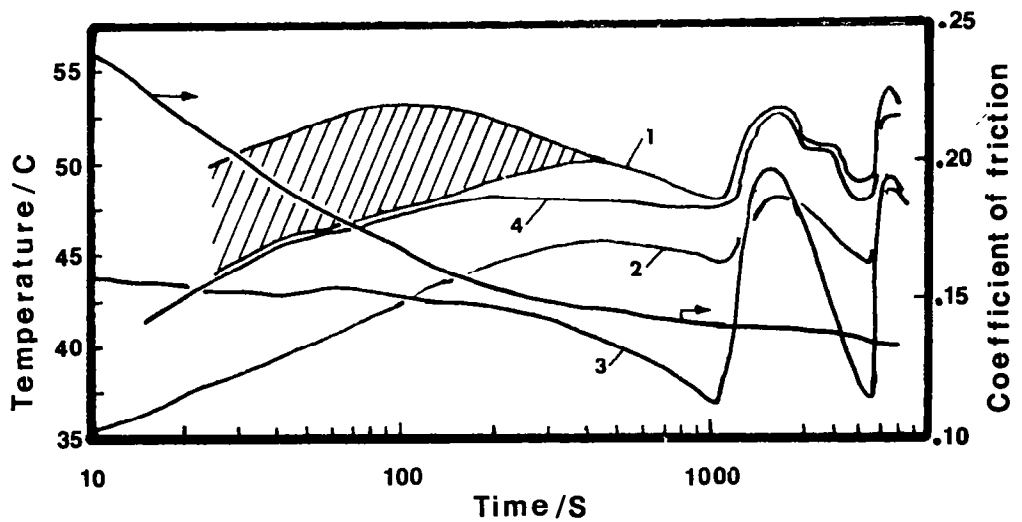
Figure 35. LFW-1 system temperatures and friction: (1) Block-contact (IR), (2) Block center (thermocouple), (3) Oil bath (T/C), (4) Shaft lock nut (IR)
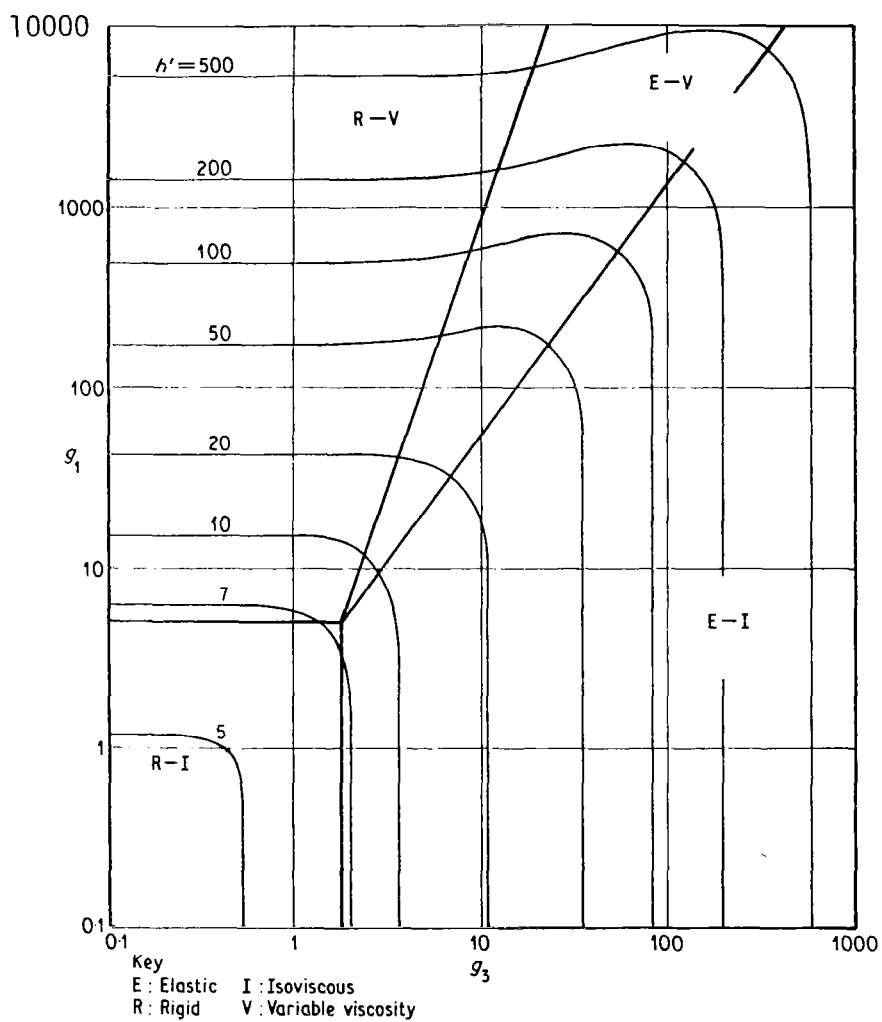
Figure 36. Regime Chart [26]
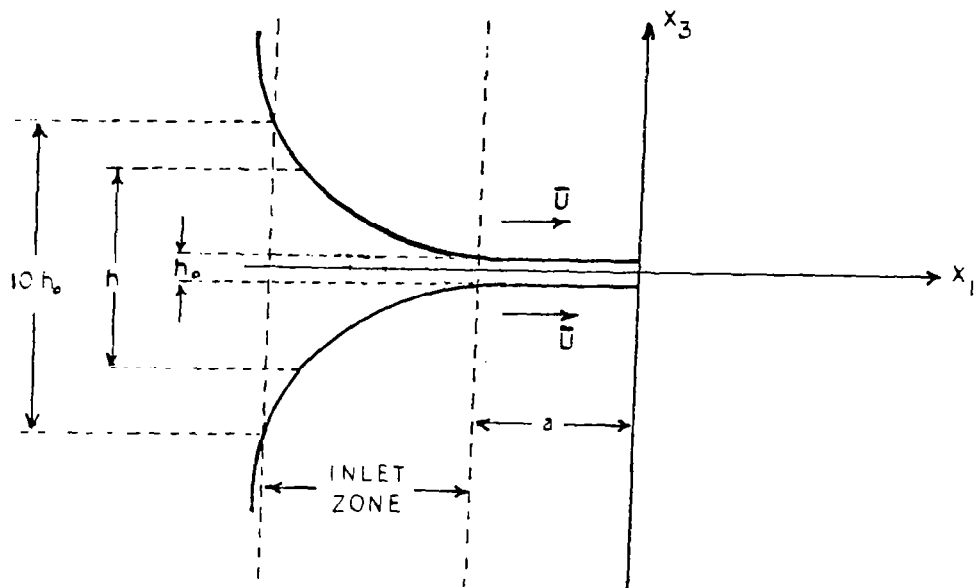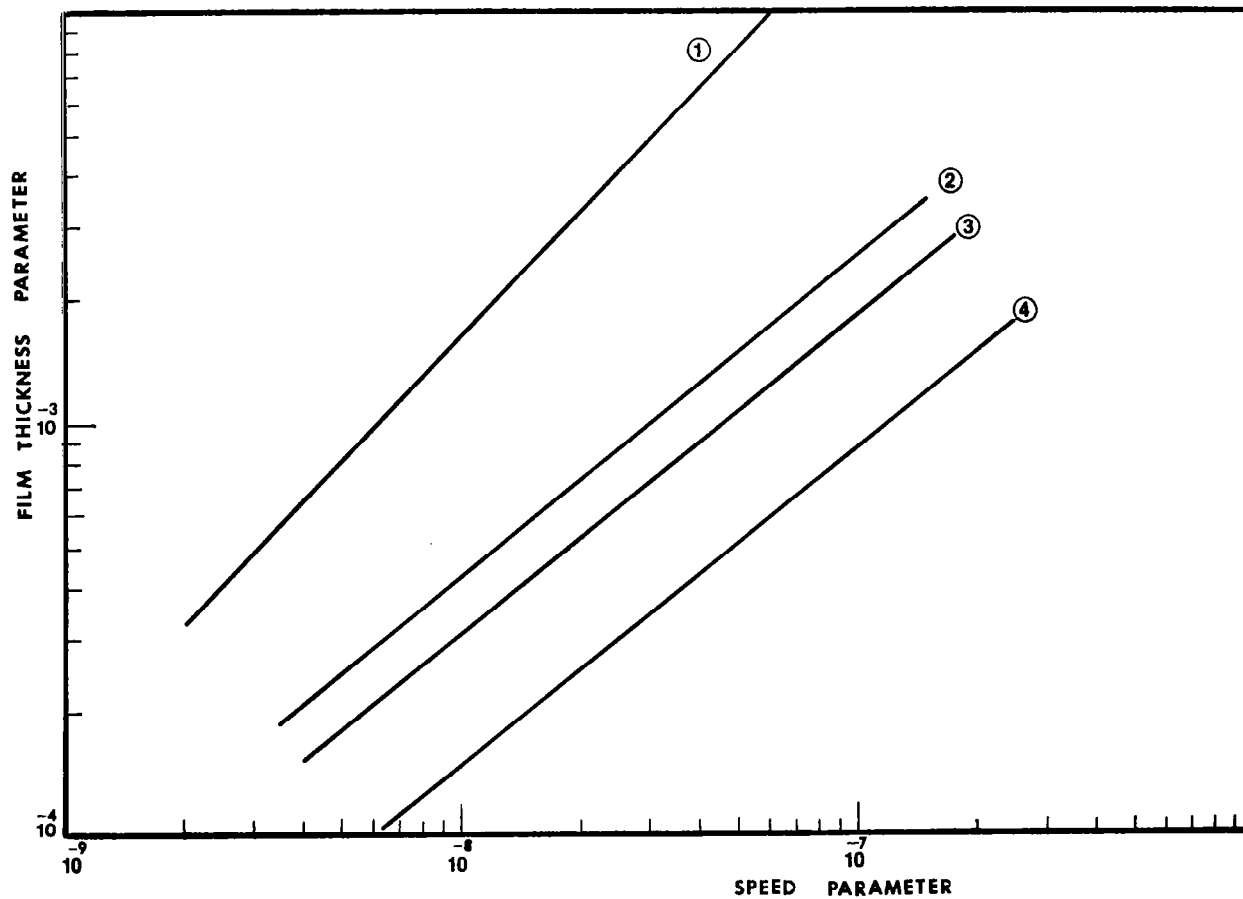
Figure 37. Contact Configuration
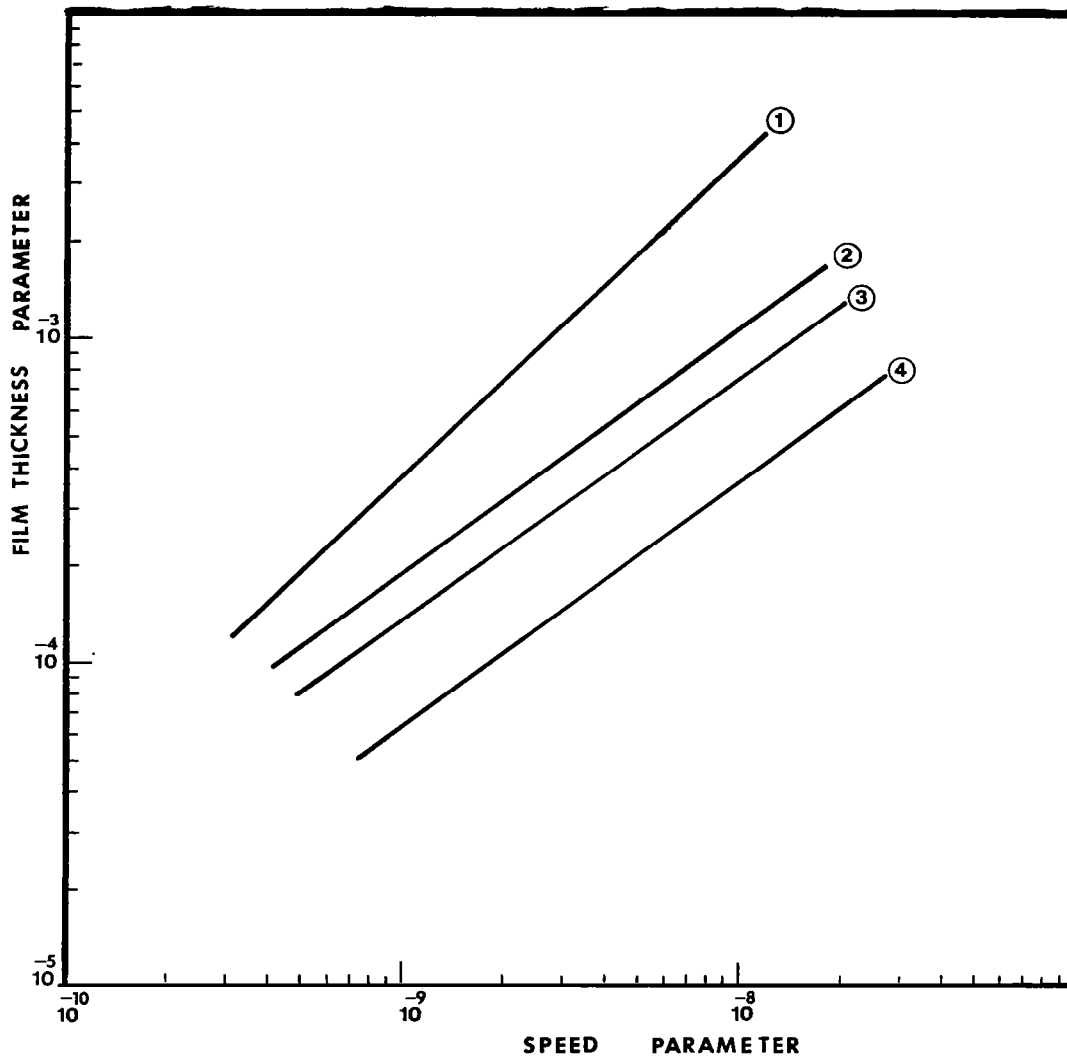
Figure 38. Speed Parameter $\left[U = \dfrac{\mu_o \bar{u}}{E_r \cdot R} \right]$ versus Film Thickness Parameter $\left[H = \dfrac{h_o}{R} \right]$ W/L = 87.6 kN/m μ_o = 0.85 Pas p_H = 5 x 10^8 N/m^2

1. R-V Newtonian
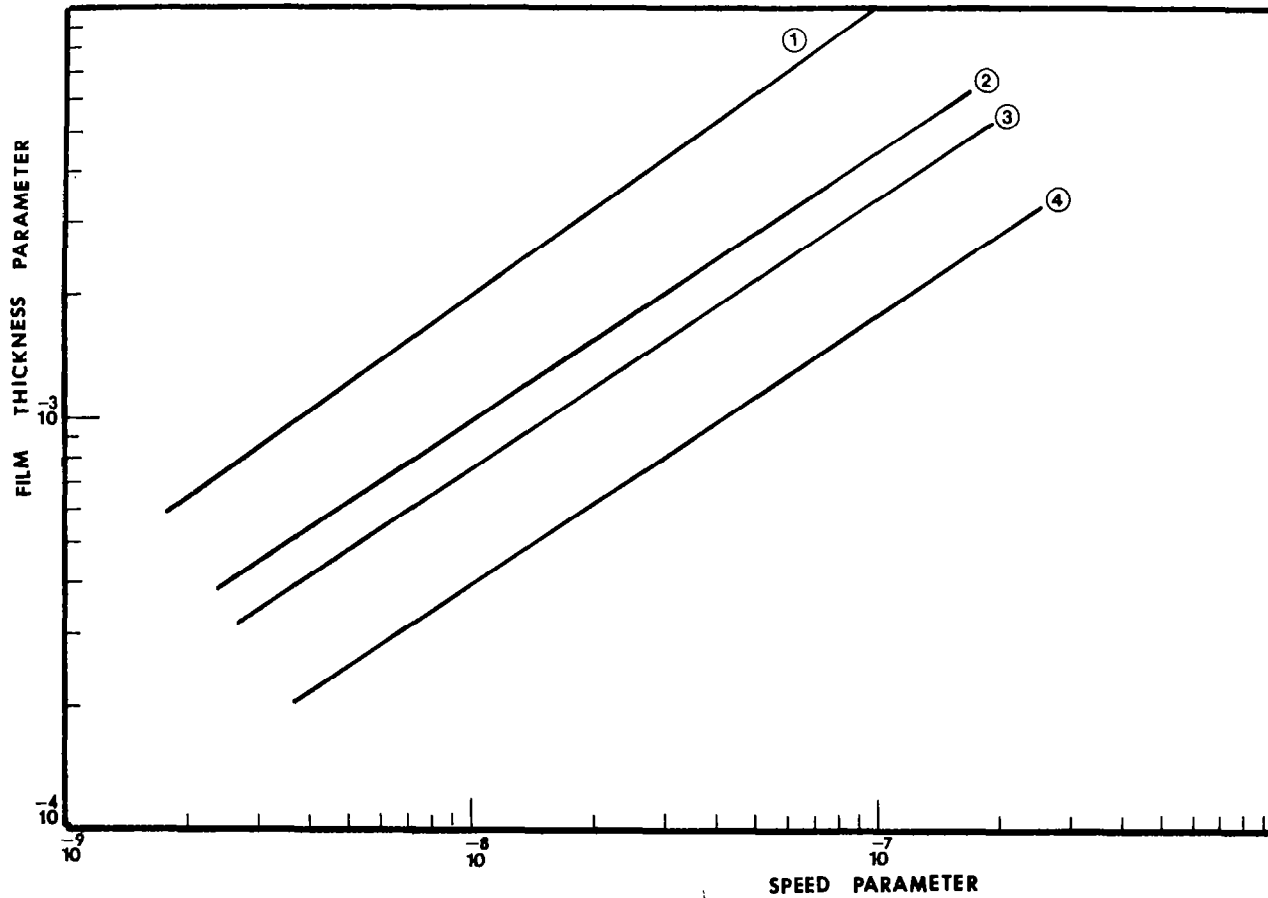2. m = 0.01 ⎫
3. m = 0.005 ⎬ Model R-V
4. m = 0.001 ⎭
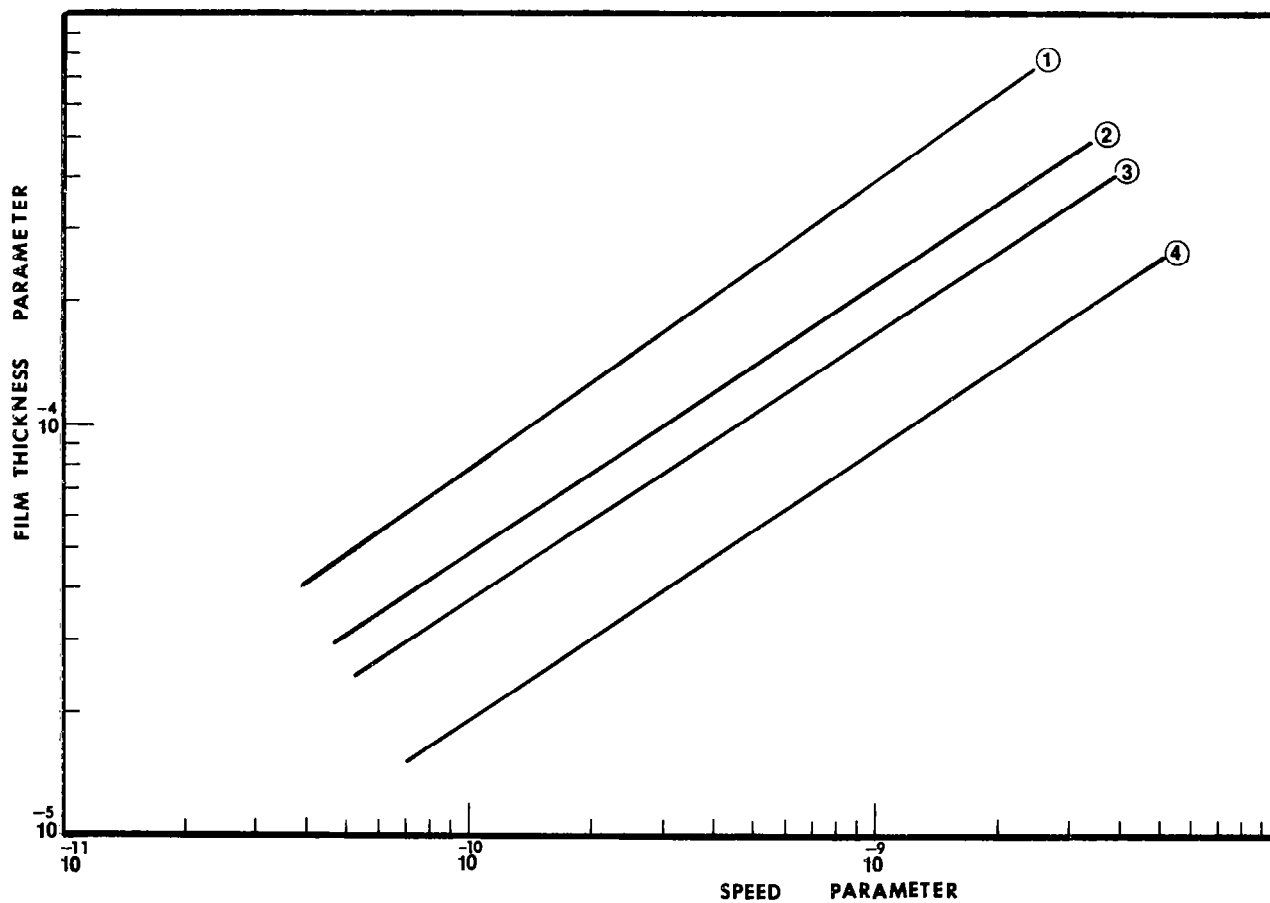
Figure 39. Speed Parameter $\left[U = \dfrac{\mu_o \bar{u}}{E_r \cdot R}\right]$ versus Film Thickness Parameter $\left[H = \dfrac{h_o}{R}\right]$

W/L = 876 kN/m μ_o = 0.85 Pas p_H = 1.6 x 10^9 N/m^2

1. E-V Newtonian (Dowson and Higginson)   3. m = 0.005 Model E-V

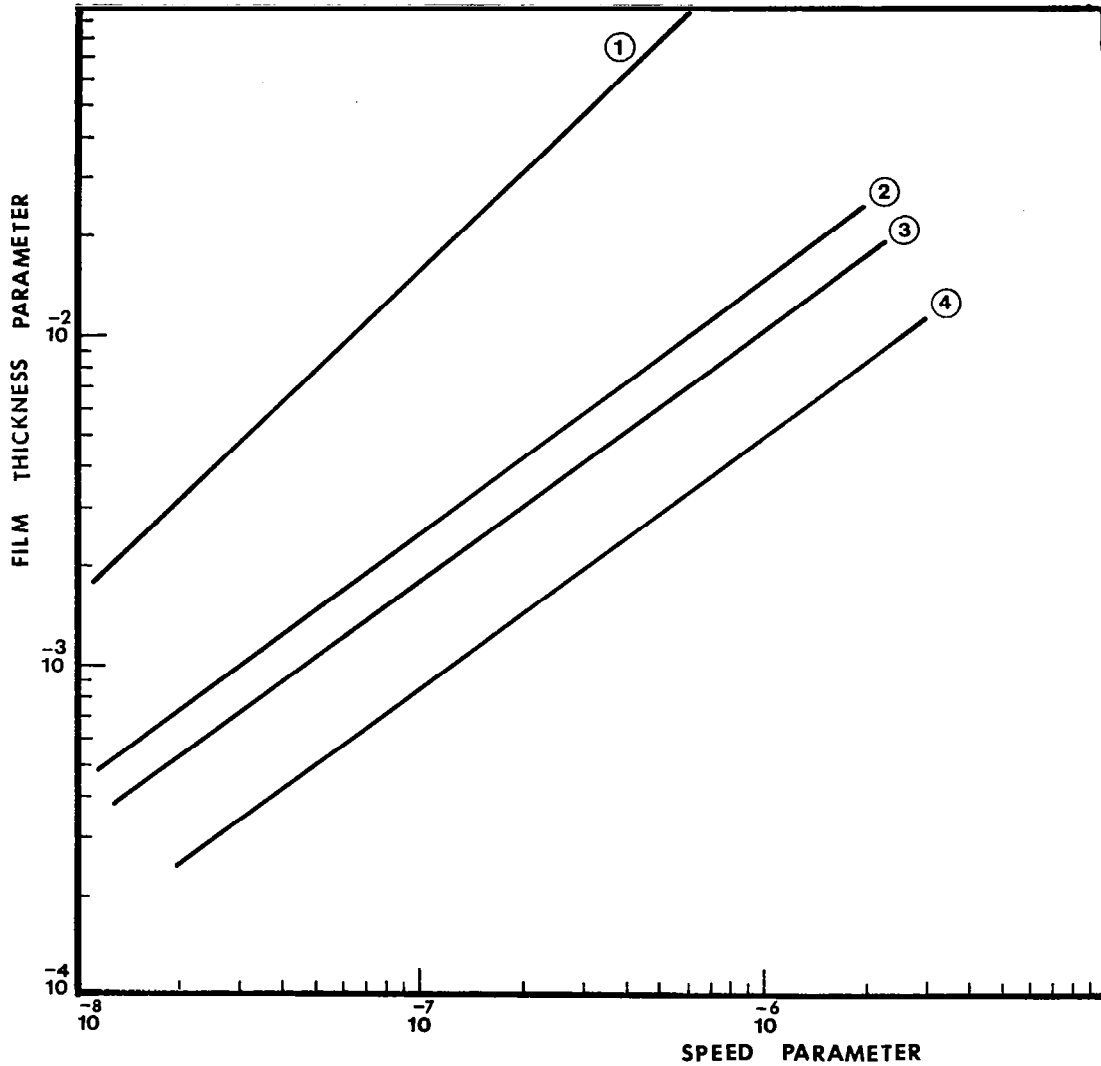2. m = 0.01 Model E-V   4. m = 0.001 Model E-V

Figure 40. Speed Parameter $\left[U = \dfrac{\mu_o \bar{u}}{E_r \cdot R}\right]$ versus Film Thickness Parameter $\left[H = \dfrac{h_o}{R}\right]$

W/L = 87.6 kN/m μ_o = 11.7 Pas p_H = 5 x 10^8 N/m^2

1. R-I Newtonian (Martin's Solution)   3. m = 0.005 Model R-I

2. m = 0.01 Model R-I   4. m = 0.001 Model R-I

Figure 41. Speed Parameter $\left[U = \dfrac{\mu_o \bar{u}}{E_r \cdot R}\right]$ versus Film Thickness Parameter $\left[H = \dfrac{h_o}{R}\right]$

W/L = 876 kN/m μ_o = 11.7 Pas p_H = 1.6 x 10^9 N/m²

1. E-V Newtonian (Dowson and Higginson)   3. m = 0.005 Model E-V

2. m = 0.01 Model E-V   4. m = 0.001 Model E-V

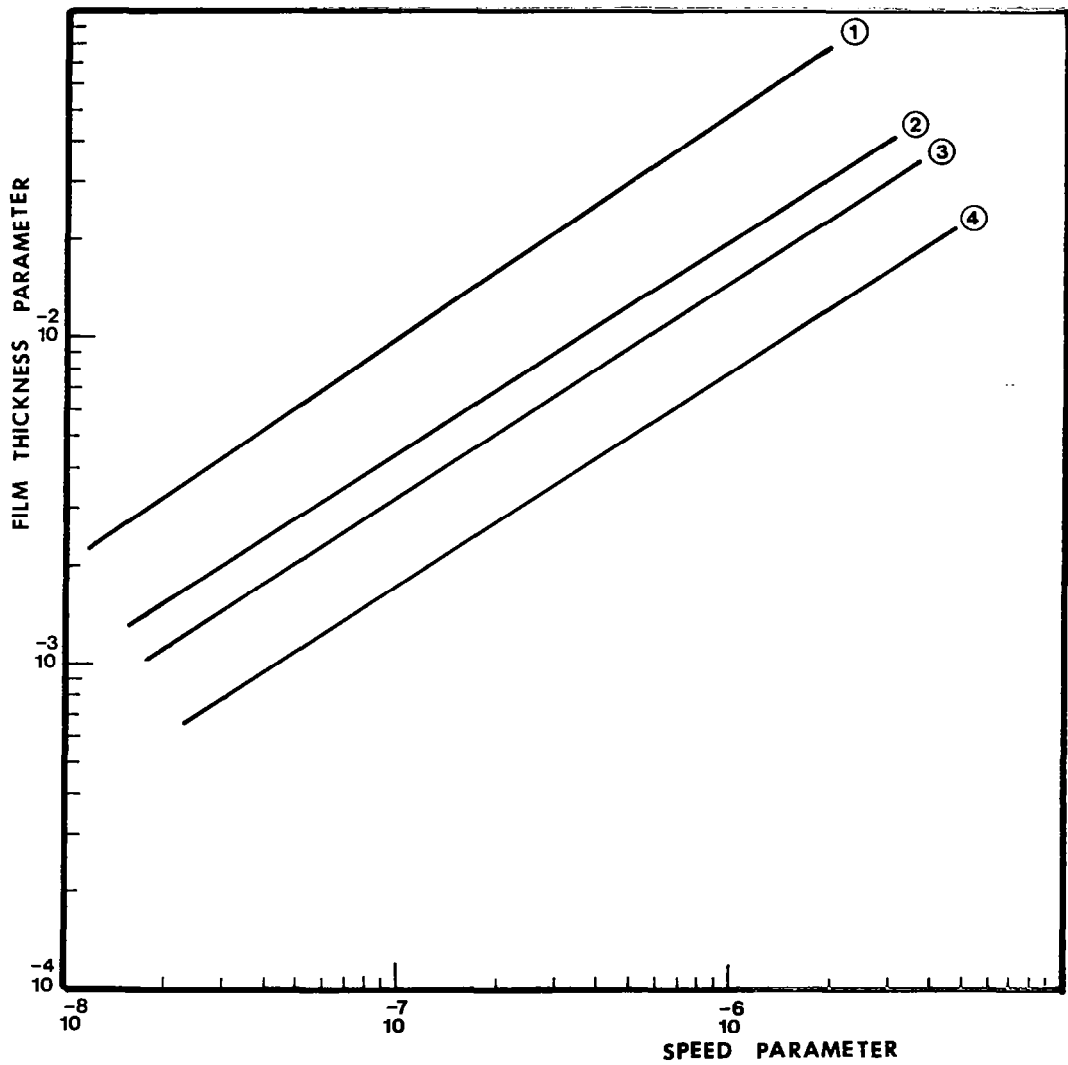Figure 42. Speed Parameter $\left[U = \dfrac{\mu_0 \bar{u}}{E_r \cdot R}\right]$ versus Film Thickness Parameter $\left[H = \dfrac{h_0}{R}\right]$

$W/L = 876$ kN/m $\mu_0 = 91$ Pas $p_H = 5 \times 10^8$ N/m^2

1. R-I Newtonian (Martin's Solution)   3. m = 0.005 Model R-I
2. m = 0.01 Model R-I   4. m = 0.001 Model R-I

112

Figure 43. Speed Parameter $\left[U = \dfrac{\mu_o \bar{u}}{E_r \cdot R}\right]$ versus Film Thickness parameter

$\left[H = \dfrac{h_o}{R}\right]$ W/L = 876 kN/m μ_o = 91. Pas p_H = 1.6 x 10^9 N/m^2

1. E-V Newtonian (Dowson and Higginson)
2. m = 0.01   Model E-V
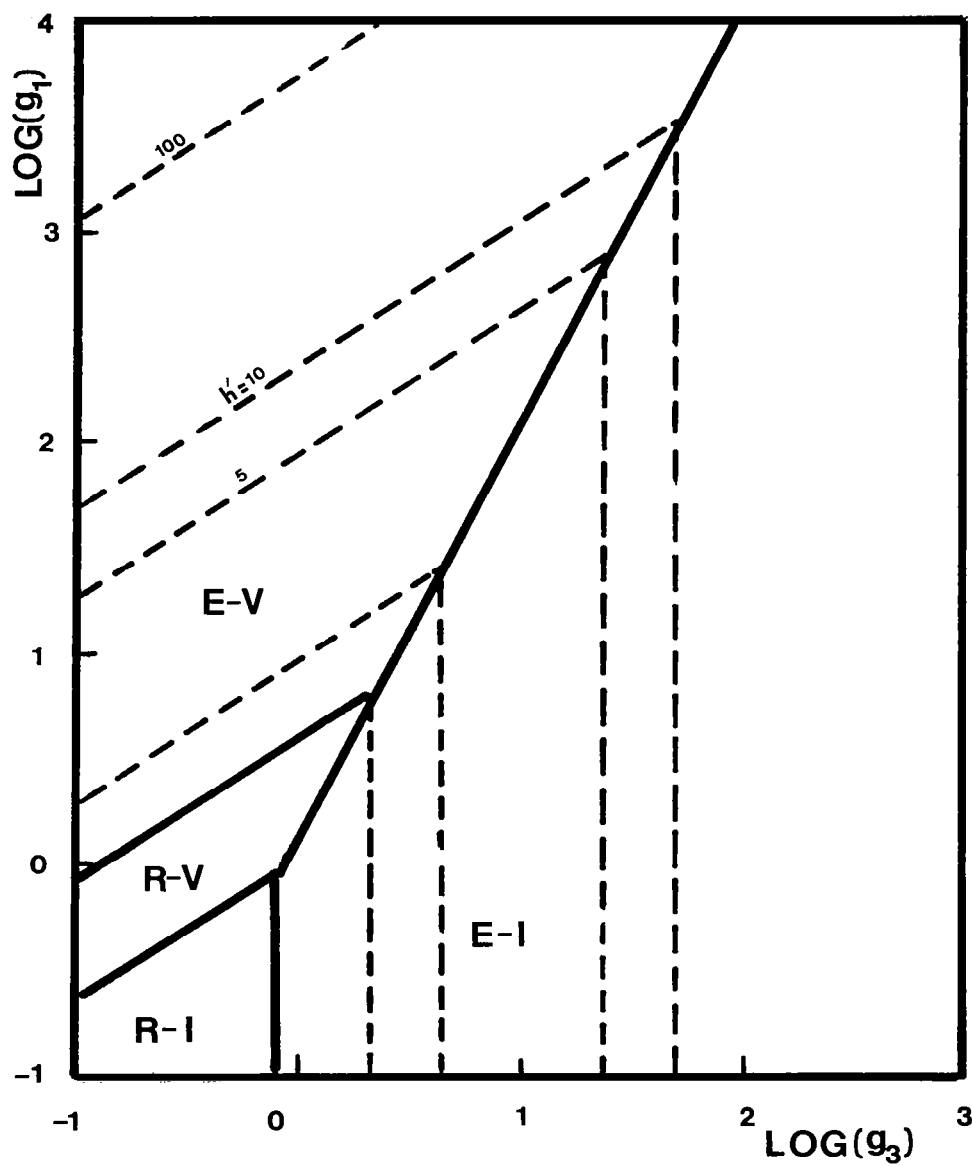3. m = 0.005   Model E-V
4. m = 0.001   Model E-V
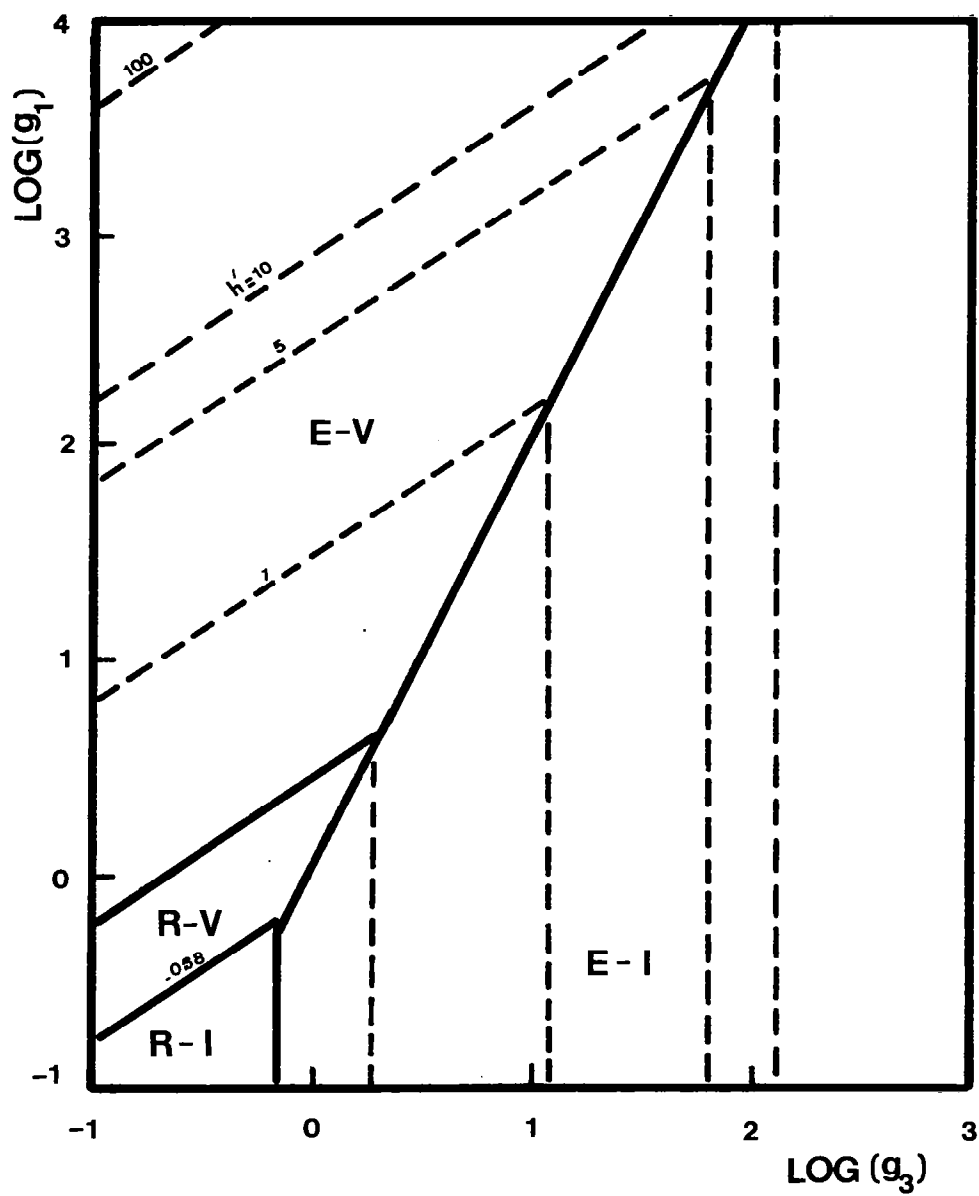
Figure 44. Regime Chart (Non-Newtonian)

m = 0.01

Figure 45. Regime Chart (Non-Newtonian)

m = 0.001

1. Report No. NASA CR-3368	2. Government Accession No.	3. Recipient's Catalog No.
4. Title and Subtitle SURFACE TEMPERATURES AND GLASSY STATE INVESTIGATIONS IN TRIBOLOGY - PART IV		5. Report Date January 1981
		6. Performing Organization Code
7. Author(s) Scott S. Bair and Ward O. Winer		8. Performing Organization Report No.
		10. Work Unit No.
9. Performing Organization Name and Address Georgia Institute of Technology Atlanta, Georgia 30332		11. Contract or Grant No. NSG-3106
		13. Type of Report and Period Covered Contractor Report
12. Sponsoring Agency Name and Address National Aeronautics and Space Administration Washington, D.C. 20546		14. Sponsoring Agency Code

15. Supplementary Notes

Lewis Technical Monitor: William R. Jones, Jr.
Final Report

16. Abstract Measurements were made of the limiting shear stress for two naphthenic oils of differing molecular weight and three blends of the lower molecular weight oil and polyalkylmethacrylate polymers of differing molecular weight. The two base oils reached the same limiting shear stress for the same temperature and pressure. This was also true for all the polymer solutions although the polymer reduced the limiting shear stress by about 15 percent. It seems that limiting stress is more a function of material type than viscosity or molecular weight. A new falling body viscometer was constructed to operate to 230° C and to 0.6 GPa. Another viscometer was constructed to extend the pressure range to 1.1 GPa. A new concentrated contact simulator has been developed which allows recording of the traction force while the slide-roll ratio is continuously varied and the rolling speed is maintained essentially constant by a single drive motor. The configuration is that of a crowned roller against a disk. Measurement of lubricant minimum film thkckness of elliptical EHD contacts of various aspect ratios were made by optical interferometry. The data collected were used to evaluate the Hamrock and Dowson minimum film thickness model over a range of contact ellipticity ratio where the major axis of the contact ellipse was aligned both parallel and perpendicular to the direction of motion. A statistical analysis of the measured film thickness data showed that on the average the experimental data were 30 percent greater than the film thickness predicted by the model. Preliminary development of the application of a scanning infrared radiation system to a tribo-system was completed. A commercial scanning IR detector was employed to measure the radiation from an especially constructed elastohydrodynamic device and from a commercial Timken type tester. The scanning rate was 25 frames per second. An analytical study was undertaken for the film thickness developed in line contacts under pure rolling conditions employing the limiting shear stress rheological model in the various lubrication regimes (rigid surface-isoviscous lubricant, rigid surface-variable viscosity lubricant, elastically deforming surface-isoviscous lubricant, and elastically deforming surface-variable viscosity lubricant). Comparsons were made in all cases with the corresponding Newtonian lubricant cases.

17. Key Words (Suggested by Author(s)) Elastohydrodynamic lubrication Traction Lubricant rheological model Contact temperatures	18. Distribution Statement Unclassified — Unlimited STAR Category 27		
19. Security Classif. (of this report) Unclassified	20. Security Classif. (of this page) Unclassified	21. No. of Pages 118	22. Price* A06